Investigation of Mass Transport Phenomena in Polymer Electrolyte Membrane Water Electrolysers

Jude Olaoluwa Majasan

Submitted in partial fulfilment of the requirements for the degree of Doctor of Philosophy of the University College London

Electrochemical Innovation Lab

Department of Chemical Engineering

University College London,

WC1E 7JE, United Kingdom.

2019

Declaration

I, Jude Olaoluwa Majasan confirm that the work presented in this thesis is my own. Where information has been derived from other sources, I confirm that this has been indicated in the thesis.

…….

Signature

……

Date

Abstract

Polymer Electrolyte Membrane Water Electrolysers (PEMWEs) are considered a promising candidate for large-scale renewable energy storage and green hydrogen production. To improve efficiency and minimize cost for large-scale deployment, operation at high current densities is necessary. However, a consequence of high current density operation is increased mass transport hindrance which degrades performance. Two components are critical to mass transport in PEMWEs, namely the porous transport layer (PTL) and the flow-field plates. Both are expected to transport liquid water, product gases, electrons, and heat with minimal fluidic, thermal and voltage losses. However, the influence of morphology and configuration of both these components and operating conditions on cell performance are not well understood.

This research investigates the mass transport phenomena in the PTL and in the flow-field channels in relation to performance in PEMWEs. The influence of flow-field configuration and two-phase flow characteristics in the flow channels on performance was studied by combined high-speed optical imaging and electrochemical characterization at various operating conditions. Results showed a strong correlation of performance with the flow path length and flow regime. Further, a correlative ex-situ X-ray tomography and in-situ electrochemical characterization approach was used to investigate the influence of PTL microstructural parameters such as mean pore diameter, pore size distribution, porosity, tortuosity, and porosity distribution on performance. Results indicated that minimizing contact resistance is most beneficial for improved performance over the range of current density studied. The influence of flow channel depth on performance was investigated by electrochemical impedance spectroscopy and a design of experiment (DoE) approach was employed to investigate the relative importance and interaction effects of mass transport factors on cell performance. Results showed the water feed rate and two-way interaction between the flow-field and PTL are most significant.

This study provides enhanced understanding of the mass transport characteristics in PEMWEs for optimized design and improved performance.

Impact Statement

The fight against global warming has seen huge growth in the global investment in renewable energy, mainly wind and solar, over the past two decades. Although, as much as 80% of the world's energy still comes from fossil fuels; researchers, policymakers and environmentalist are united over the need to stop global warming. This was evidenced by the recent UN's COP21 Paris climate change conference, an agreement between 196 countries to reduce emission of greenhouse gases, chiefly carbon emissions – a notorious cause of climate change. Thus, the shift to zero-carbon renewable energy is gathering pace. From being on the peripheral of the energy system just over a decade ago, renewable energy is now growing faster than any other energy source and becoming increasingly competitive.

However, renewables are intermittent; therefore, a successful transition to a carbon-free future is dependent on achieving significant progress with energy storage technologies of equivalent storage capacity. This reality has led to increased investments in various energy storage technologies including batteries, fuel cells, electrolysers, etc.

The electrolysis technology is still not widely commercialized due to cost-intensiveness and low efficiency, despite its potential to enhance renewable energy deployment and as a source of green hydrogen production. To achieve increased cost and performance efficiency, operation at high current density is desirable. However, mass transport losses in the electrolyser system hampers efficiency at high current density; and the understanding of the mass transport phenomena is limited. A better understanding of these processes is necessary for design optimization and performance improvement of the PEMWE system, and has prompted a flurry of research in recent years.

This thesis investigates mass transport processes involving electrochemical reactions, multicomponent and multi-phase flow in the PEMWE using a range of advanced diagnostic techniques. The results presented in this thesis show that the PTL and flow-field/bipolar plate are crucial components of PEMWE performance, especially at high current density.

It is shown that various flow-field configurations and operating conditions impact performance. The flow-field design and channel length was found to play a crucial part in determining two-phase flow characteristics in the flow-field plate which influences overall performance. Particularly, the annular flow regime impedes mass transport in the PEMWE at high current density.

The various losses (ohmic, charge transfer, mass transport) related to the porous transport layer (PTL) were investigated, and the results show that smaller pore PTL shows better electrical conductivity but poorer mass transport resistance, and vice versa for larger pore PTLs. The result suggests that maximizing contact points between the PTLs and catalyst layer is the overriding performance-influencing factor for PTL design.

The study of influence of channel depth also revealed an optimum point beyond which the positive influence of depth is compromised. A preliminary design of experiment (DoE) study revealed that the water feed rate and the interaction between the flow field plate and the PTL are key mass transport parameters for optimization of PEMWE performance.

The ultimate aim of this research is to provide increased understanding of the mass transport phenomena in a typical PEMWE system to enable optimized design of components and ultimately improved performance.

Acknowledgements

I am forever grateful to my supervisor, Professor Dan Brett who gave me the opportunity to work at the Electrochemical Innovation Lab and who has been a tremendous mentor for me. Such was his enthusiasm and verve at teaching that just after a couple of classes during my Masters I decided I definitely want to work with him if I register for a PhD at UCL. But even for my prescience, I could not have predicted how excellent a supervisor he is. He gave so generously his time, inputs, advice and funding to make this research a success. Despite my early-stage struggle, his support never wavered, his guidance was excellent and his encouragement was tremendous – right through to the end. I feel immensely privileged to have worked under, perhaps, the best PhD supervisor anyone could wish for.

My deepest appreciation to my co-supervisor, Professor Paul Shearing for his guidance and technical support throughout this programme. To Dr Ishanka Dedigama, thank you for all the time we had together. Your guidance and support in the lab, especially in those early days were hugely helpful. I also appreciate Dr Aubras for the fruitful research collaboration we had. The time we spent together in the lab discussing science, though short, was one of the highlights of my programme.

I gratefully acknowledge the funding received towards this research from the Presidential Scholarship for Innovation and Development and the Petroleum Development Trust Fund, Nigeria.

A massive thank you to every member of the EIL past and present; colleagues, academics and administrators, who assisted in various aspects of this work, particularly Leon, Dami, Xuekun, and Jay. I appreciate the contributions and insightful discussions at various times with Tan, Yunsong, Max, Nive and James. Special thanks to Jason Cho, Francesco Iacoviello, and Toby Neville for the many fruitful discussions and for technical assistance in key parts of this research work. I am really very grateful for your invaluable contributions.

My heartfelt appreciation to my parents: their unrelenting whatever-the-cost determination to ensure I get a good education set in motion the incredible journey that has brought me to this point. I am grateful for their prayers and support that

has kept me going all these years. Thank you to all my wonderful siblings for their love and support. You're all greatly appreciated.

Special thanks to Sis Ruth Ijomah and family for the enormous support on the family front throughout this programme. And to all my friends and brethren (too many to list here) at LCA, I appreciate everyone for their help, prayers and support.

To my beloved wife, Jemimah, thank you so much for your love and support throughout this experience. Your immense patience and encouragement got me through the highs and lows of this programme.

Above all, I owe it all to the Almighty God; my unalloyed thanks and adoration to Him. He is my sustainer, enabler, and strength-giver, and it's His mercies and grace that has brought me thus far. It's a massive understatement, but this wouldn't even be remotely possible without His grace. All the glory goes to Him.

Publications

- **J. O. Majasan**, J. I. S. Cho, I. Dedigama, D. Tsaoulidis, P. Shearing, and D. J. L. Brett, "Two-phase flow behaviour and performance of polymer electrolyte membrane electrolysers: Electrochemical and optical characterisation," *International Journal of Hydrogen Energy*, vol. 43, no. 33, pp. 15659–15672, 2018.
- **J.O Majasan,** J.I.S Cho, M. Maier, I. Dedigama, P. R Shearing and D. J.L Brett. "Effect of Anode Flow Channel Depth on the Performance of Polymer Electrolyte Membrane Water Electrolyser," *ECS Trans.*, vol. 85, no. 13, pp. 1593–1603, 2018.
- **J. O. Majasan**, F. Iacoviello, J.I.S Cho, M. Maier, X. Lu, T.P Neville, I. Dedigama, P. R. Shearing, and D. J. L Brett, "Correlative study of microstructure and performance for porous transport layers in polymer electrolyte membrane water electrolysers by X-ray computed tomography and electrochemical characterization," *Int. J. Hydrogen Energy*, vol. 44, no. 36, pp. 19519–19532, 2019.
- **J. O. Majasan**, F. Iacoviello, P. R. Shearing, and D. J. Brett, "Effect of Microstructure of Porous Transport Layer on Performance in Polymer Electrolyte Membrane Water Electrolyser," *Energy Procedia*, 2018.
- F. Aubras, J. Deseure, J.-J. A. Kadjo, I. Dedigama, **J.O Majasan**, B. Grondin-Perez, J.-P. Chabriat, and D. J. L. Brett, "Two-dimensional model of low-pressure PEM electrolyser: Two-phase flow regime, electrochemical modelling and experimental validation," *Int. J. Hydrogen Energy*, vol. 42, no. 42, pp. 26203–26216, 2017.
- M. Maier, Q. Mayer, **J. O. Majasan**, C. Tan, I. Dedigama, J. Robinson, J. Dodwell, Y. Wu, L. Castanheira, G. Hinds, P. Shearing, and Dan Brett, "Operando Flow Regime Diagnosis using Acoustic Emission in a Polymer Electrolyte Membrane Water Electrolyser," *J. Power Sources,* vol. 424, pp. 138–149, 2019.

Table of Contents

List of Tables

List of Figures

List of Symbols and Abbreviations

Symbol	Definition
E^0	Reversible cell voltage [V]
E_{cell}	Cell Voltage [V]
g	Gravitational acceleration [9.81 m s^{-2}]
F_b	Buoyancy force [N]
R_{cell}	Cell ohmic resistance [Ω]
F_d	Drag force [N]
F_i	Inertia force [N]
P_i	Partial pressure of gas *i* [Pa]
R_b	Radius of bubble [m]
V_b	Volume of bubble [m^3]
a_b	Acceleration of bubble [m s^{-2}]
d_b	Bubble diameter [µm]
d_p	Pore diameter of porous media [µm]
i_0	Exchange current density [A cm^{-2}]
j_G, j_L	Superficial velocities of gas and liquid
l_b	Length of bubble [m]
α_i	Activity of species
T	Temperature, [°C or K]
ΔG	Change in Gibbs free energy [J mol^{-1}]
ΔH	Enthalpy change
ΔS	Entropy change [J K^{-1}]
E	Electrode Potential [V]
C_i	Concentration of specie *i* [mol m^{-3}]
F	Faraday's constant [96,485 C mol^{-1}]
M	Molecular weight [kg mol^{-1}]
d_{chan}	Hydraulic diameter of channel [mm]
G	Mass flow flux in channel, [kg m^{-2} s^{-1}]
R	Ideal gas constant [J $mol^{-1}K^{-1}$]
V	Cell Voltage [V]

$\boldsymbol{a}$	Cross-sectional area of channel [m^2]
$\boldsymbol{i}$	Applied current [A]
$\boldsymbol{j}$	Current density [A cm^{-2}]
$\boldsymbol{n}$	Number of electrons transferred
$\boldsymbol{t}$	Time [s]
$\boldsymbol{x}$	Quality of the two-phase flow
$\boldsymbol{\alpha}$	Charge transfer coefficient
$\boldsymbol{\gamma}$	Surface tension of interface [N m^{-1}]
$\boldsymbol{\zeta}$	Water stoichiometry ratio
$\boldsymbol{\eta}$	Overpotential [V]
$\boldsymbol{\theta}$	Contact angle [°]
$\boldsymbol{\mu}$	Kinematic viscosity of fluid [Pa s]
$\boldsymbol{\rho}$	Density [kg m^{-3}]
$\boldsymbol{\phi}$	Fibre diameter [µm]
$\boldsymbol{\omega}$	Radial frequency [rad s^{-1}]
$\boldsymbol{Z}$	Impedance [Ω]
$\dot{\boldsymbol{N}}_{\boldsymbol{H_2O}}$	Molar rate of water consumption
$\boldsymbol{J}$	Diffusion flux [mol $m^{-2}s^{-1}$]
$\boldsymbol{D}$	Diffusivity [m^2 s^{-1}]

List of Symbols and Abbreviations

Abbreviation	Definition
AC	Alternating Current
AEL	Alkaline Electrolyser
ANOVA	Analysis of Variance
CPE	Constant Phase Element
CT	Computed Tomography
DC	Direct Current
DI	Deionized Water
DMFC	Direct Methanol Fuel Cell
DoE	Design of Experiment
EC	Equivalent Circuit
EIS	Electrochemical Impedance Spectroscopy
GW	Gigawatts
HER	Hydrogen Evolution Reaction
Hz	Hertz
LP-PTL	Large Pore Porous Transport Layer
MEA	Membrane Electrode Assembly
MPD	Mean Pore Diameter
MW	Megawatts
OCV	Open Circuit Voltage
OER	Oxygen Evolution Reaction
OFAT	One Factor At A Time
PD	Pore Diameter
PEMWE	Polymer Electrolyte Membrane Water Electrolyser
PFF	Parallel Flow-field
PMMA	Polymethyl Methacrylate
PSD	Pore Size Distribution
PTL	Porous Transport Layer
RHE	Reversible Hydrogen Electrode
SEM	Scanning Electron Microscopy

SOEC	Solid Oxide Electrolyser
SP-PTL	Small Pore Porous Transport Layer
SSFF	Single serpentine Flow-field
TEM	Transmission Electron Microscopy
TW	Terawatts
YSZ	Yttria-stabilized Zirconia
CNC	Computerized Numerically Controlled
PEM	Polymer Electrolyte Membrane
PVC	Polyvinyl Chloride

Chapter 1

Introduction

1.1 Background and Motivation

Renewable energy sources such as solar, wind, and hydrothermal are becoming increasingly attractive and gaining widespread use in response to the growing global concern over energy sufficiency, ecological sustainability and environmental problems such as air pollution, greenhouse gas emissions, and natural resource depletion [1]–[4]. At least 13 countries – including Uruguay, Nicaragua, Costa Rica and several European countries – have met 10% or more of their electricity consumption with wind power since 2017 [5]. Global solar adoption surged by nearly a third to 402 GW in 2017, with at least 29 countries having installed 1 GW or more [5]. Also, in 2017, for the eighth consecutive year, global investment in renewable energy exceeded $240 billion, bringing cumulative investment since 2004 to $2.9 trillion [6]. In total, a record 150 GW of renewable power was installed globally in 2017, more than a threefold increase within four years; and by 2018, a landmark figure of 1 TW of wind and solar power has been installed globally [7].

Even so, fluctuations and intermittency of these renewable energy sources remain a huge challenge. Renewable energy load-profiles typically consist of periods of peak supply interleaved with long periods of shutdown. Thus, the increased integration of renewable energy into the energy supply grids has brought the intermittency challenges to the fore even as energy demands outpace supply and global energy

demand is predicted to grow by about 40% in the next 20 years [4][8]. Presently, conventional power plants are used to compensate for the demand-supply gap. However, these power plants depend largely on fossil fuel, and therefore fail to provide a solution to the sustainability problem. As the capacity of renewable energy sources continues to grow, into the terawatt range, energy storage systems of equivalent capacity are required. Consequently, it is becoming ever more urgent to develop efficient energy storage technologies that would boost renewable energy deployment and enhance grid stabilization [9].

The Power-to-Gas technology has a huge potential to tackle this issue. Thus, hydrogen has been identified as a clean and flexible energy carrier and a far more attractive option for energy storage from renewable and intermittent power sources. Furthermore, hydrogen can be used in fuel cells to generate electricity with high efficiency for mobile and automotive applications, thereby replacing fossil fuel for pollution-free mobile and transport applications [10], [11]. In addition, compressed hydrogen has a higher specific energy (energy per unit mass) than gasoline, a huge advantage in automotive applications [12], [13]. Also, hydrogen can be converted to synthetic methane for energy production due to the easy-to-handle nature of methane [14].

At present, roughly 90% of global hydrogen production is through reforming of natural gas, gasification of coal, and gasification and reforming of heavy oil [15]. These production routes rely heavily on the use of non-renewable hydrocarbon feedstock, which compromises the low-carbon credibility of the hydrogen produced and, ultimately, does not contribute to the realisation of a "carbon-balanced" energy matrix. Consequently, there is a growing interest in the search for effective alternatives to produce hydrogen in a clean, safe and sustainable manner. To this end, electrochemical conversion of water to hydrogen and oxygen through *water electrolysis* described in Eq. 1.1, first discovered by Troostwijk and Diemann in 1789 [16], has been identified as an ideal route for high-quality hydrogen production.

$$H_2O_{(l)} + electricity \rightarrow H_2 + \frac{1}{2}O_2 \qquad (1.1)$$

Water electrolysis technology has been known for over two centuries, but, at present, accounts for only ~5% of the world hydrogen production, largely due to

prohibitive cost. However, this outlook is changing with the global surge in renewable energy use and the increasing devotion to energy sustainability. Coupling renewable energy infrastructure to electrolysis technology allows for safe, sustainable and pollution-free hydrogen production while simultaneously providing a solution to the intermittency of renewable energy. A schematic of the ideal 'energy cycle' where water electrolysis plays a key role in hydrogen production from renewable energy for various applications is illustrated in Figure 1.1.

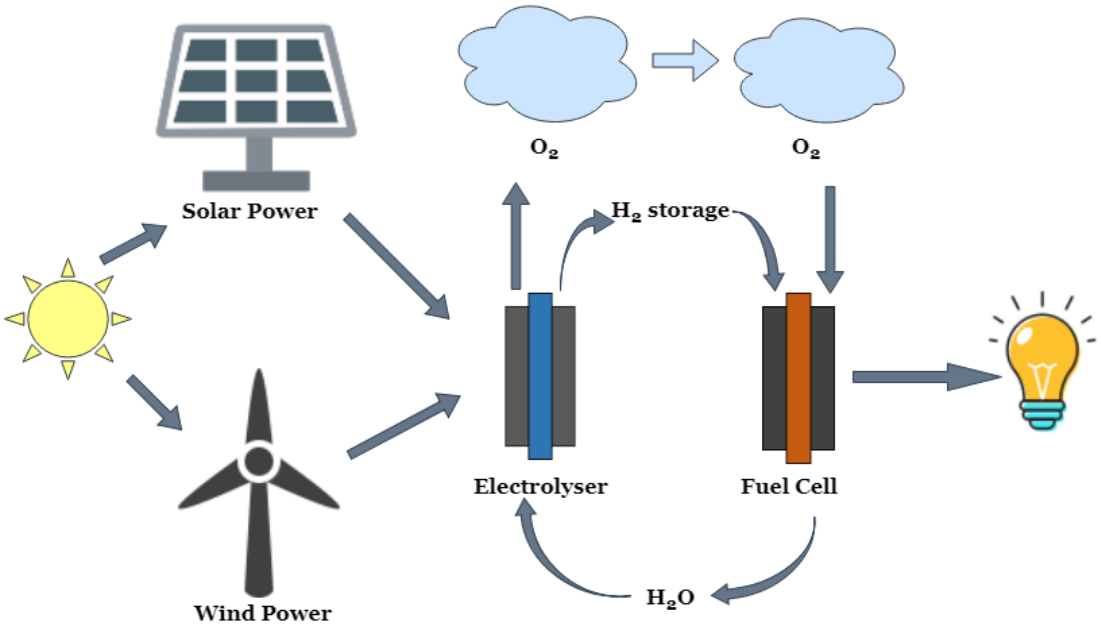

Figure 1.1. Schematic illustration of the ideal energy cycle with water electrolysis playing a key role in hydrogen production from renewable energy.

Since the first discovery of electrolysis, three main electrolyser types have been developed, differentiated principally by their electrolyte type. They are alkaline electrolyser (AEL), polymer electrolyte membrane water electrolyser (PEMWE), and solid oxide electrolyser (SOEC). Figure 1.2 presents a summary of the operating principles of the various electrolyser technologies.

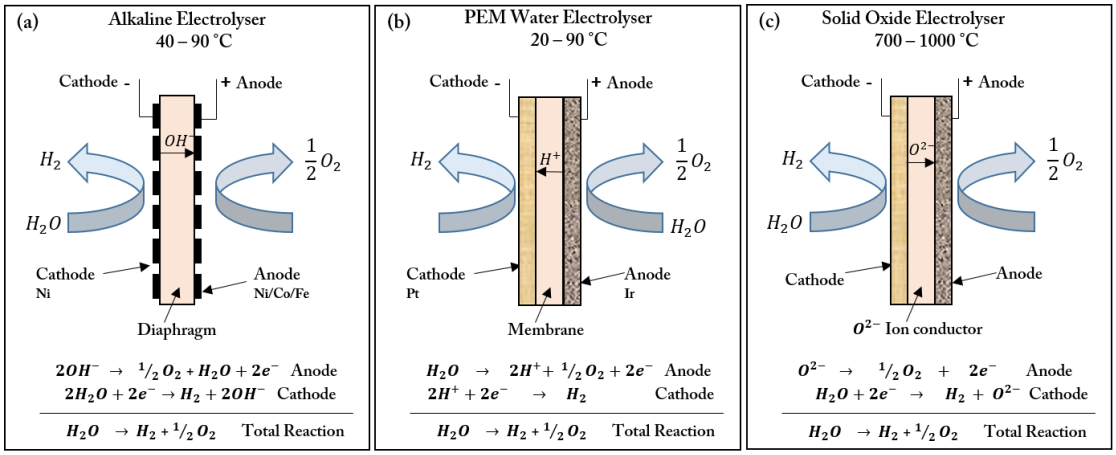

Figure 1.2. Specifications and operating principles of the electrolyser types.

1.2 Alkaline electrolyser

The alkaline electrolyser is the most mature electrolyser technology for hydrogen production up to the megawatt range, and the most commercially implemented worldwide [17]. It consists of two electrodes immersed in aqueous alkaline solution (KOH or NaOH) and separated by a diaphragm to avoid recombination of the product gases and enable good efficiency and safety. The diaphragm is required to possess good ionic conductivity and high chemical and physical stability. The basic operation of the alkaline electrolyser is shown in Figure 1.2(a) and a summary of the key operational parameters are presented in Table 1.1.

There are three major drawbacks associated with the alkaline electrolyser [18]. First, is the inability to operate at high pressure (the typical operational pressure is 25-30 bar), which makes for a bulky stack design. Second, is the low maximum achievable current density (~0.4 A cm^{-2}), due to high ohmic losses across the liquid electrolyte and diaphragm. The gas bubbles produced at the electrodes reduces the contact between the electrodes and electrolyte, thus increasing the cell resistance and efficiency suffers as a result. Third, is the low partial load range, that is, limited production rate (in the range of 25-100% of the nominal power) due to diffusion of gases through the diaphragm at partial load. This lower partial load range does not seem to be beneficial, in particular, for the flexible use of alkaline water electrolysis on the basis of renewable resources since a non-negligible fraction of the capacity for electrolysis cannot be used for hydrogen production[19].

Table 1.1. Summary of the key operational parameters of electrolyser types [20].

	Alkaline Electrolyser	**PEM Water Electrolyser**	**Solid Oxide electrolyser**
State of development	Commercial	Commercial	Laboratory
H_2 production in m^3/s (STP, per system)	<0.211 ≈2.7 MW	Up to ~0.125 ≈1.6 MW	-
Electrolyte	Alkaline solution	Solid polymer membrane (Nafion)	ZrO_2 ceramic doped with Y_2O_3
Charge carrier	OH^-	H_3O^+/H^+	O^{2-}
Cell temperature (ºC)	40-90	20-90	700-1000
Cell Voltage (V)	1.8 – 2.4	1.8 – 2.2	0.91 – 1.3
Current density (A cm^{-2})	0.2 – 0.4	0.6 – 3.0	-
Specific energy consumption: Stack (kW h Nm^{-3})	4.2 – 5.9	4.2 – 5.6	-
Cold start time	Minutes to hours	Seconds to minutes	-
Advantages	Well established technology, long-term stability, non-noble catalyst, relatively low cost, stacks in MW range.	Compact system design, high gas purity, high current densities, high voltage efficiency, rapid-response system, good partial load range, and dynamic operation.	Non-noble metal catalysts, high pressure operation, high electrical efficiency, integration of waste heat possible.
Disadvantages	Corrosive liquid electrolyte, Gas crossover (degree of purity), low partial load range, low dynamics, low current densities, and low operational pressure.	Corrosive acidic environment, high cost of component material, and commercialization.	Bulky system design, limited long term stability of the cells, expensive, not suited to fluctuating systems.
Transient operation	Possible but leads to problems, reduction up to 20% load possible, overload operation possible.	Better than the alkaline counterpart, dynamic adjustment possible, partial (down to 5%) and overload operation possible.	Not well suited

1.3 Solid Oxide Electrolyser

The Solid Oxide Electrolyser (SOE, also known as high temperature electrolyser) is the least developed of the electrolysis technologies and still in the laboratory stage; although research has grown in the last decade with increasing interest from companies, research centres and universities [21]. In the Solid oxide electrolyser, zirconia (ZrO_2) doped with yttrium (III) oxide (Y_2O_3) is the commonly used electrolyte, due to its high oxygen ion conductivity, as well as having good chemical and thermal stability at the required temperatures (750-1000°C) [22]. Other electrolyte materials that have been considered include Scandia stabilized zirconia (ScSZ) [23] and lanthanum gallate (or lanthanum strontium gallium magnesium oxide, LSGM) materials [24]. For the cathode, porous cermet composed of yttria-stabilized zirconia (YSZ) and metallic nickel is most commonly used, whereas lanthanum strontium manganite (LSM)/YSZ composite is most commonly used as the anode material.

The main advantage of the SOE is the reduced electricity demand for the electrolysis process at higher temperatures because the Joule heat produced within the cell, when electrical current is passed, is put to use. Also, electrode overpotentials, responsible for power losses in the electrolyser cell, are reduced. Although the heat demand for the electrolysis process increases with increasing temperature, the elevated temperature condition reduces the equilibrium cell voltage and therefore the electricity demands. Since roughly two-thirds of the cost of electrolytic hydrogen arises from the use of electricity, the cost of the hydrogen produced can be decreased, especially if the increase in heat energy demand is fulfilled by an external heat source, such as renewable energy, nuclear power, or waste heat from high-temperature industrial processes [21].

The main drawbacks of the solid oxide electrolyser are the fast material degradation and the limited long term stability, both of which are consequences of the high temperature operation [25]. Also, huge capital cost is incurred for additional processing of the mixture of hydrogen and steam in the product stream. Besides, severe stability issues have been reported in coupling the technology with fluctuating and intermittent power sources [20], [26].

1.4 Polymer Electrolyte Membrane Water Electrolyser (PEMWE)

The first solid polymer electrolyte electrolyser was developed by General Electric in the 1960s mainly to overcome the shortcomings of the alkaline electrolyser [18]. In the PEMWE, a thin solid proton-conducting membrane is used as the electrolyte instead of the caustic solution used in alkaline electrolysers. The membrane is responsible for the high protonic conductivity, low gas crossover, compact system design and high pressure operation of the PEMWE. The most commonly used membrane material is Nafion® from DuPont.

Compared to the alkaline electrolyser, the PEMWE possesses a number of key advantages largely due to the thin proton-conducting membrane. The thinness of the membrane enables lower ohmic losses; and since the maximum achievable current density in the electrolyser cell is dependent to a large extent on ohmic losses, higher current densities can be achieved. PEMWEs are thus operated at higher current densities (>2 $A\,cm^{-2}$), potentially reducing the operational and overall electrolysis cost [27]. Also, high purity hydrogen is obtained due to the low gas crossover property of the membrane. Furthermore, a wider range of power input is achieved in the PEMWE due to the faster rate of proton transport across the thin membrane compared to the sluggish transport in the alkaline electrolyser caused by the liquid electrolyte and its associated inertia. This aspect is particularly important when the electrolyser operates under the fluctuating conditions typical of renewable energy sources [18].

Other advantages of the PEMWE over its alkaline counterpart, include ability to cover the full range (10–100%) of nominal power density due to the low permeability of hydrogen through Nafion® (<$1.25 \times 10^{-4}\ cm^3 s^{-1} cm^{-2}$ for Nafion® 117, standard pressure, 80 °C, 2 $mA\,cm^{-2}$) [4]. Additionally, the solid electrolyte allows for a compact system design with durable structural properties, in which high operational pressures (equal or differential across the electrolyte) are achievable [28]. For instance, pressures up to 350 bars have been reported in some commercial systems [29]. The high pressure operation allows delivery of hydrogen at a high pressure for the end user, thus providing energy savings on downstream compression and storage. High pressure operation also reduces the volume of the gaseous phase at the electrodes, significantly improving product gas removal [30].

Due to the highlighted advantages, the PEMWE technology is, on balance, preferred over other electrolyser technologies and has, therefore, attracted a great deal of research in recent years [31], [32]. Public funding agencies and private companies (such as Proton Onsite, Hydrogenics, Giner, Siemens and ITM Power) have increased R&D investments to develop durable electrolysis units with high Nm^3 H_2/hour delivery range that would improve technology competitiveness. However, the key drawback of the PEMWE is the corrosive environment created by the PEM and the high overvoltage at the anode which necessitates the use of special materials for its construction. These materials must not only resist the harsh corrosive low pH condition (pH <2), but also sustain the high applied overvoltage (~2 V), especially at high current densities. This precondition renders a lot of common, inexpensive materials unsuitable, thus, typical materials for PEMWE construction are scarce and expensive. Therefore, to achieve large-scale commercialization, the material and cost aspect must be addressed.

1.4.1 Overview of PEM Water Electrolyser components

The main components of a PEMWE are the solid polymer electrolyte membrane (PEM), electrocatalyst layers, porous transport layers (PTLs)/current distributors and flow-field/bipolar plates. The basic design of the PEMWE is shown in Figure 1.3. The PEM is at the centre of the cell, on either side of which are attached porous electrodes/electrocatalyst layers (one at the anode for the oxygen evolution reaction, OER; and the other at the cathode for the hydrogen evolution reaction, HER). The collection of the PEM and the electrocatalyst layers is collectively called the membrane electrode assembly (MEA). The MEA is clamped between two porous transport layers (PTLs)/current distributors, and two flow-field plates having flow channels machined in them for water and gas transport. Mechanically soft peripheral gaskets are often used to seal the cell. Individual PEMWE cells are put together in series (stack) to increase gas production. Stacks consisting of 50-60 cells are common in industrial systems [33].

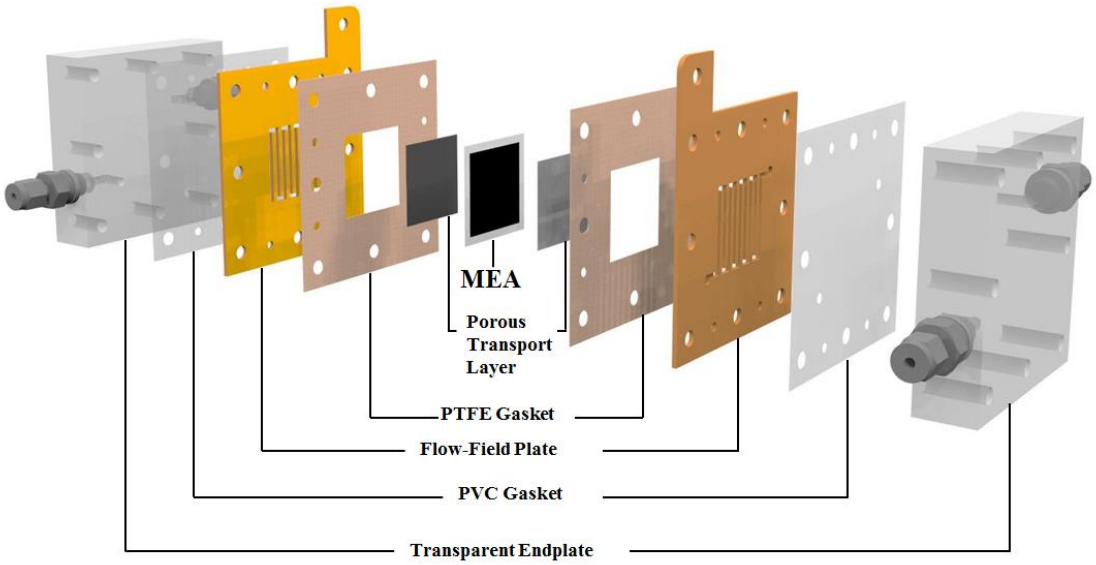

Figure 1.3. Schematic of a PEM Water Electrolyser

1.5 Problem Statement

To realize the widespread commercialization and achieve good competitiveness of the PEMWE for large-scale hydrogen production and renewable energy storage, further research to combat current technical issues is crucial. This includes finding solutions for efficiency, durability, and high investment costs. Currently, the total investment costs of a PEM electrolyser system are two times bigger than that of its alkaline counterpart, due largely to the distinctive materials imposed by the corrosive low pH conditions of the PEM [20], [34]. Consequently, one current goal is to reduce investment cost from the present 1000–2000 €/kW to 300–600 €/kW in 2030 [34]. Accordingly, an approach that has been considered for cost efficiency is high current density operation. This would enable increased hydrogen output at a similar investment cost. For instance, doubling operational current density from 2 A cm^{-2} to 4 A cm^{-2} would double hydrogen output (assuming 100% Faradaic efficiency) with negligible effect on stack cost. Thus, there is a significant incentive for high current density operation. However, a consequence of high current density operation is increased mass transport hindrance due to the need to deliver water to the electrodes and removal of product gases. It is therefore important to understand the mass transport phenomena in the PEMWE, and achieve optimized design of cell components associated with water, gas and electron transport to minimize transport losses and achieve overall improved performance.

1.6 Objective of Thesis

There is limited understanding of mass transport phenomena in the PEM water electrolyser, especially at high current densities, which is the impetus for the research described in this thesis. At elevated current densities, the volume of gases produced (oxygen at the anode, and hydrogen at the cathode) becomes rather large and could lead to significant gas accumulation in and around the electrocatalyst layer and a reduction in the active area available for the electrolysis reaction causing mass transport limitation and performance degradation. To avoid severe mass transport losses, a better understanding of the mass transport of reactant liquid water and product gases across the PTL and flow-field channels is essential. It is important to understand the two-phase flow behaviour and the influence of various two-phase flow regimes on performance at high current densities as well as optimal design and microstructure of components that maximizes mass transport and performance.

The aim of this thesis is to enhance understanding of mass transport in the PTL and the flow-field channels of the PEMWE especially at high current densities where mass transport is the limiting factor. Previous studies have shown that the cathodic contribution to performance losses is less critical, as most of the voltage losses are related to the electrochemical processes at the anode [35]. Therefore, this research focuses on the diagnostic of mass transport characteristics at the anode side of the PEM electrolyser which includes examination of two-phase counter-current liquid/gas flow in the anode side PTL and flow-field plates.

The specific research objectives are:

- To build optically transparent PEMWE cells for direct visualization and understanding of two-phase liquid/gas flow behaviour in different flow-field channel configurations.
- To investigate how various operating parameters such as flow circulation, water feed rate, and operating temperature impact the two-phase flow behaviour and overall cell performance.

- To provide understanding of how various two-phase flow regimes (bubbly, slug, annular) influence the cell electrochemical performance by simultaneous high-speed imaging and electrochemical measurements.
- To investigate the influence of flow channel parameters, specifically channel depth, on two-phase flow and regimes in the flow channel and hence, electrochemical performance.
- To relate the microstructural characteristics of the porous transport layer (PTL) to their electrochemical performance by simultaneous X-ray tomography and electrochemical measurements.
- To investigate the individual and interaction effects of mass transport parameters on PEMWE performance by application of statistical design of experiment (DoE) technique.

Through these objectives, this study offers insights into the mass transport processes in the PEM electrolyser thus potentially enabling better design of mass transport components and enhanced performance. This would contribute towards achieving the goal of large-scale commercialization of the PEMWE technology for hydrogen production and renewable energy storage.

1.7 Thesis Overview

This thesis begins with an introduction to the global energy/climate challenge, the increasing deployment of renewable energy and the growing opportunity to harness electrolysis technology for green hydrogen production and solving the intermittency problem of renewable energy. The three main types of electrolyser technologies were highlighted, with their advantages and drawbacks. The PEMWE technology is then singled out with a discussion of its positive and negative aspects and the current technical challenges leading to the motivation and objective of the work described in this thesis.

Chapter 2 presents the theoretical framework, principles and techniques which underpin this study. The PEM electrolyser technology is introduced more comprehensively including a more detailed examination of the working principle and cell components. An analysis of cell thermodynamics and efficiency metrics is presented as well as a discussion of the operating conditions critical to PEMWE

performance. This is followed by description of the mass transport phenomena at the PEMWE anode including the physics of bubble evolution and two-phase flow in channels. This chapter closes with a review of relevant literature on PEMWE flow field configurations, PTL types and PTL microstructural properties that are shown to influence PEMWE performance.

Chapter 3 details the experimental procedures and techniques used in this thesis. It discusses the development (design and fabrication) of the two different PEMWE cells used in this study, as well as the discussion of various *operando* and *ex-situ* techniques and electrochemical methods employed.

Chapter 4 is the first of the results chapters and presents the investigation of gas-bubble dynamics and two-phase flow behaviour in the anode flow-field of a working PEMWE in relation to cell performance; including the effect of flow configuration and various operational parameters. The influence of water circulation, water feed rate and temperature on bubble evolution and performance is presented.

Chapter 5 examines the influence of anode channel depth on the PEMWE performance at various channel depths and current densities using electrochemical impedance spectroscopy. In this study, a single-channel cell was designed and fabricated and the influence of depth on two-phase flow at current densities up to 2 A cm^{-2} is presented.

Chapter 6 examines the relationship between the microstructure and corresponding electrochemical performance of some commonly used titanium sinter PTLs with mean pore diameter ranging from 16 μm to 90 μm. These microstructure-performance relationships are studied *ex-situ* using scanning electron microscopy and X-ray computed micro-tomography to determine key structural properties and the electrochemical performance was studied *operando* using polarization curve and electrochemical impedance spectroscopy.

Chapter 7 is the final results chapter and presents the investigation of the effect and interactions of anode mass transport parameters on performance of a PEMWE using a 2^3 full factorial Design of Experiments (DoE) approach with replication.

The effects of anode flow-field design, anode porous transport layer and water feed rate on the cell performance as well as their interactions were studied.

Chapter 8 presents a summary of the work presented in this thesis. This chapter closes with a discussion of opportunities for future work.

Chapter 2

Literature Review: PEM Water Electrolyser Technology

The first PEMWE was developed by General Electric Co. in the 1960s for space applications and first commercialized in 1978. The technology is currently available at small and medium-scale commercial applications and is becoming increasingly attractive for energy storage applications due to the increased investment in renewable energy and the increasing devotion to energy sustainability. Recent research efforts are focused on improving PEMWE performance and finding new suitable and cheaper materials to increase cost-competitiveness and ultimately large-scale commercialization.

In this chapter, the fundamental operating principles and the main components of the PEMWE are presented, followed by a review of the key operating conditions and a description of the mass transport phenomena in the PEMWE including the physics of bubble evolution and two-phase flow in channels. Thereafter, a review of relevant literature on flow-field design, PTL types and microstructural properties is presented.

2.1 Working Principle of the PEM Water Electrolyser

The PEM Water electrolyser is similar to a PEM fuel cell in both construction and operation, with the difference being that the half reactions take place at opposite electrodes and water and gases flow in opposite direction to those in a fuel cell [36],

[37]. The overall PEMWE cell operation consists of two half-cell reactions: the hydrogen evolution reaction (HER) at the cathode and the oxygen evolution reaction (OER) at the anode. Water is fed to the anode where it is dissociated into electrons, protons and oxygen in the form of gas bubbles (Eq. 2.1). Oxygen is expelled from the cell through the anode-side porous transport layer (PTL) and flow-field channels to the cell outlet. The protons travel across the proton-conducting membrane to the cathode. The electrons exit the cell via the external direct current power source, which supplies the driving force (i.e. cell potential) for the reaction. At the cathode, the electrons recombine with the protons to produce hydrogen gas (Eq. 2.2). The hydrogen gas is then transported through the cathode-side PTL and flow-field channels toward the cell outlet. Due to the limited self-ionization of pure water, an acid is used as the electrolyte and electrocatalysts are applied to lower the activation energy of the process. The overall reaction is presented in Eq. (2.3).

Anode reaction: $$2H_2O \rightarrow 4H^+ + O_2 + 4e^- \quad (2.1)$$

Cathode reaction: $$4H^+ + 4e^- \rightarrow 2H_2 \quad (2.2)$$

Overall reaction: $$2H_2O \rightarrow 2H_2 + O_2 \quad (2.3)$$

2.2 PEMWE components

The PEM electrolyser consists of a membrane electrode assembly (MEA), which is a collection of the anode, cathode and the solid electrolyte; porous transport layers/current distributors, flow-field plates with channels and end plates (not shown in diagram) that hold the cell together, as illustrated in Figure 2.1.

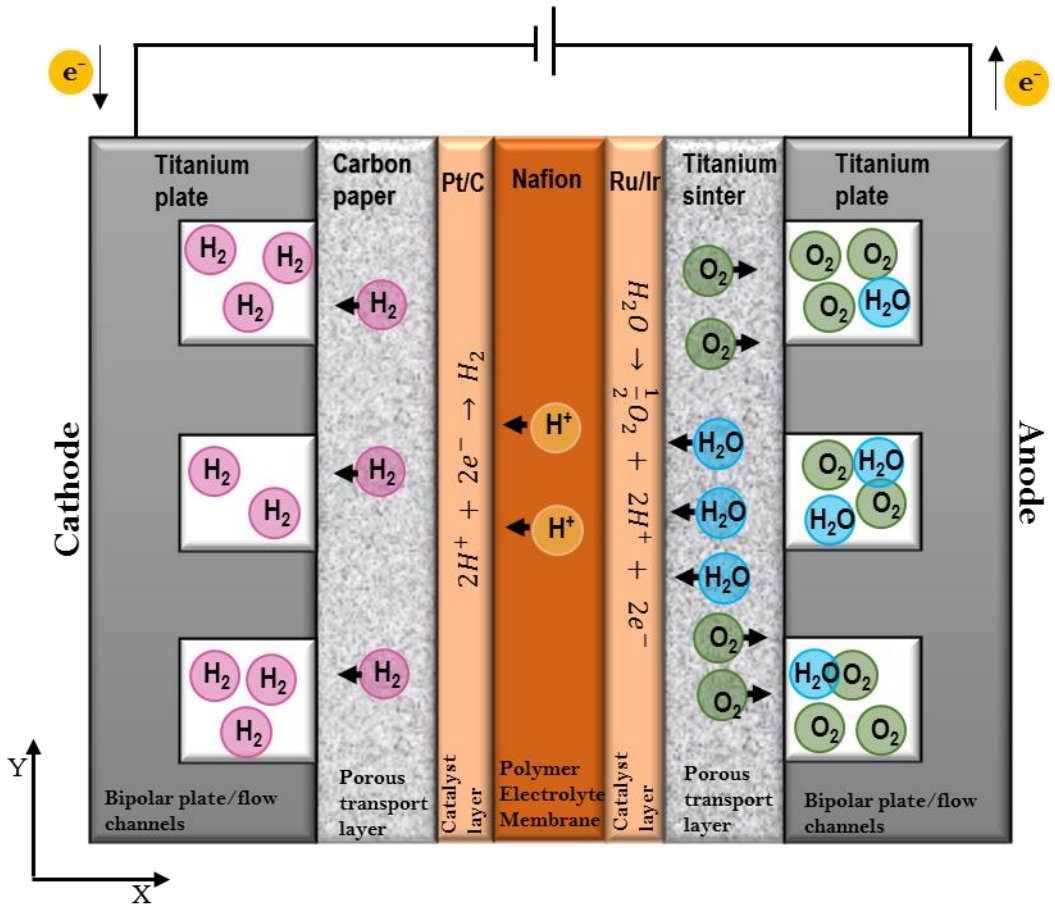

Figure 2.1. Schematic of a PEM Water Electrolyser showing the components and water-gas two-phase flow through the PTL and flow channels.

2.2.1 Membrane Electrode Assembly (MEA)

In the PEMWE cell, the two half-cells are separated by a solid acidic membrane called polymer electrolyte membrane or proton exchange membrane. In most cell designs, the electrodes are deposited directly on to the membrane, creating the key component of the PEM electrolyser cell: the membrane electrode assembly (MEA). The MEA ensures selective conduction of protons and separation of product gases while providing insulation and gas separation between the electrodes. The industry standard membrane in the PEMWE is Nafion®, a perfluorosulfonated ion-exchange ionomer characterised by low area specific resistance (0.15 Ω cm^2 for Nafion 117), high proton conductivity (0.15 S cm^{-1} at 80°C), good mechanical properties and excellent electrochemical stability [38]. A drawback of the Nafion membrane is that the conductivity decreases at temperatures above 100°C due to membrane dehydration. Alternative membrane materials that might be suitable for

higher temperature applications have been investigated, mostly sulfonated hydrocarbon membranes such as poly(ether ether ketone) (PEEK), poly (ether sulfone) PES and their blends [39]–[41].

Due to the high acidity of the perfluorinated membrane used in state-of-the-art PEMWE cells, expensive noble metals or their oxides are used as electrocatalysts. At the cathode, platinum black or carbon-supported platinum-based catalysts used in PEM fuel cell cathodes are also used in PEM water electrolysers, shown in Figure 2.3. Significant progress has led to reduction of platinum loading from ~4 mg cm^{-2} to ~0.3 mg cm^{-2}, achieved by using high surface area carbonaceous catalyst supports such as carbon powders [42], carbon nanofibers [43] and carbon nanotubes [44]. At the anode, the OER takes place at a much higher potential (~1.5 – 1.8 V vs. RHE), thus catalysts with good activity and stability are necessary. The most active and stable catalysts for the OER in PEMWEs are based on noble metal oxides [45]–[47].

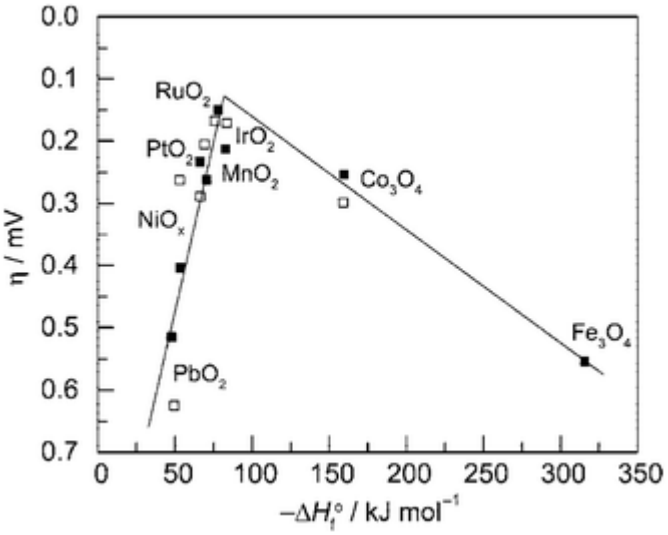

Figure 2.2. "Volcano plot" showing activity for O_2 evolution on metal oxide electrodes *versus* the enthalpy of transition of the oxide in acidic (■) and basic (□) solutions. Overpotential measured relative to 0.1 mA cm^{-2} current density. Adapted from [48].

Trasatti [48] investigated a number of electrocatalysts, and as shown in Figure 2.2, noble metal oxides RuO_2 and IrO_2 are located at the top of the plot because of their low redox potential and good electrical conductivity. RuO_2 has the highest activity

towards oxygen evolution as it has the lowest overpotential as a function of the transition enthalpy of going from the lower to the higher oxidation number. However, it is prone to instability in the oxygen evolution reaction [49], as it is further oxidised to its highest oxidation number, RuO_4 which is liquid at room temperature. RuO_4 have a melting point and boiling point of 25°C and 130°C respectively [50], thus RuO_2 is corroded under typical electrolyser operating temperatures[31]. IrO_2 on the other hand is less active towards the OER but far more stable and has been used mostly on its own[39], [51], to stabilize RuO_2 [49] or as mixed oxide in the form of $Ir_xRu_{1-x}O_2$ [52], [53].

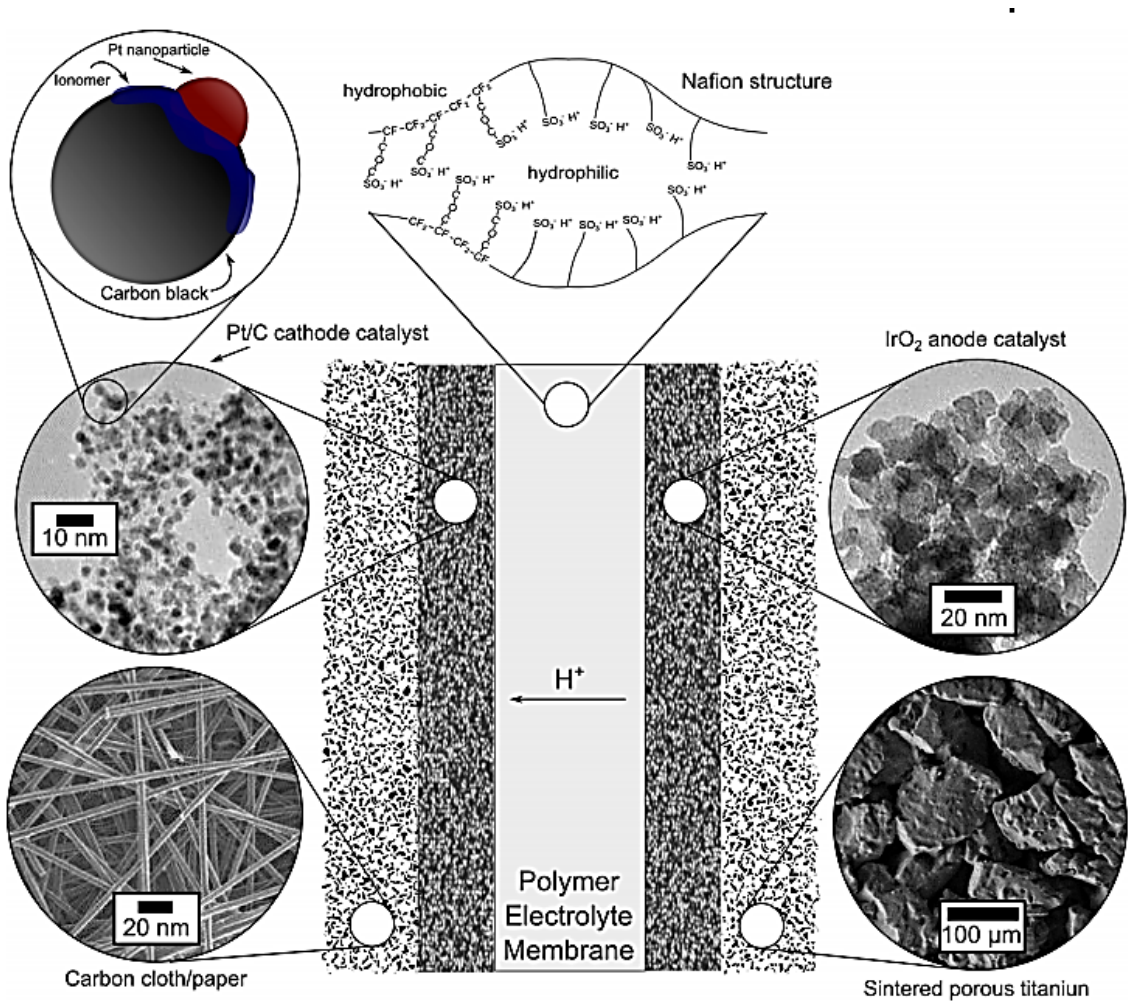

Figure 2.3. Cross-section schematic of a catalyst-coated membrane (MEA) of a PEM Water electrolyser. Insets: micro/nano structure for each component obtained either by scanning electron microscopy (SEM) or by transmission electron microscopy (TEM). Reproduced from [54].

2.2.2 Porous Transport Layer (PTL)

The porous transport layer/current distributor is placed between the MEA and bipolar/flow-field plate in the PEMWE, and is responsible for mass transport of liquid water and gas between the electrodes and the flow channels of the flow-field plate, as well as electrical and heat conduction. Through its pore phase, the reactant water is supplied to the electrode and the product gas in form of bubbles is removed from the electrode. Through its solid phase, electrons and heat are transported between the electrode and the flow-field plate. In cases where differential pressure is applied, the PTL also provide mechanical support to the membrane. These functions of the PTL requires that they possess certain characteristics [55]:

(i) Optimized pore structure for good water permeability and gas diffusivity to enable effective and efficient delivery of water to the electrocatalyst and transport produced gas in the opposite direction.
(ii) High electrical and thermal conductivity and resistance to passivation over time.
(iii) Good corrosion resistance to withstand the high overpotential, acidic and oxygenated environment at the anode.
(iv) High mechanical strength especially under operational differential pressure.

At the PEMWE cathode, carbon fibre-based materials, similar to those used in PEM fuel cells are typically used as PTLs. However, at the anode, due to the high electrochemical potential and low pH, the choice of materials is usually limited to titanium-based porous materials, in the form of sintered powders, fibres, foam or meshes [56]–[60].

2.2.3 Bipolar/Flow-field Plates

The bipolar/flow-field plates encase the two half-cells and provide the electrical contact to the external power supply. Usually, the flow channels are machined in them for transport of liquid water to the electrodes and produced gases out of the cell. Frames with sealing elements or gaskets tighten the half-cell to prevent gas and water leakage from the inside to the environment. The bipolar/flow-field plates act as:

(i) Conductor, transferring electrons from the anode of one cell to the cathode of the adjacent cell.
(ii) Distributor of reactant water to the electrode and to remove product gases.
(iii) Separator of evolved gases at the electrodes.
(iv) Mechanical support to the membrane and electrodes.

These functions require the materials of the flow-field plate to possess specific properties such as corrosion resistance, high electrical and thermal conductivity and high mechanical strength. The bipolar plate is an expensive component which accounts for ~48% of the total cost of the PEMWE stack [61]. Materials such as stainless steel, titanium and coated- stainless steel and copper plate have been used for its construction [62]–[64]. Titanium has excellent electrical conductivity, corrosion resistance and mechanical strength but it is expensive and difficult to machine and forms a passivation layer after extended use that impairs its electrical and thermal conductivity [65]. Thus, they are often gold-coated to ensure durability albeit at an increased cost [66]. Gold-coated stainless steel/copper is a less expensive alternative to titanium, but imperfections in the coating or prolonged use exposes the metal to corrosion. Corrosion of base metal causes the destruction of the coating increasing the ohmic resistance [27], [62], [64]. Also, the coating or exposed metal ion dissolves over time and diffuses into the PEM membrane and decrease ionic conductivity, leading to increased membrane degradation[64]. Due to the various cost and durability trade-offs, both material and cost optimization of bipolar plate has received increased attention in recent years [61], [67].

2.3 Thermodynamics of Water Electrolysis

In a thermodynamic sense, the water molecule is highly stable. Thus, the electrolysis of water is an uphill process that is thermodynamically unfavourable at room temperature and only occurs when sufficient electrical energy is supplied. To achieve electrolysis, a minimum *equilibrium (or reversible) cell voltage*, E^0 must be overcome. This equilibrium cell voltage E^0 (at standard temperature and pressure) is the difference between the equilibrium potential at the electrodes, described by Eq. 2.4 as [54]:

$$E^0 = E^0_{anode} - E^0_{cathode} \tag{2.4}$$

The maximum energy obtainable as work from a chemical reaction is determined by the Gibbs free energy change (ΔG) of the reaction given by Eq. (2.5) as:

$$\Delta G = \Delta H - T\Delta S \tag{2.5}$$

where ΔH is the enthalpy change, T the temperature, ΔS the entropy change, and $T\Delta S$ represents the thermal energy demand for the reaction. The Gibbs free energy sets the magnitude of the reversible voltage for an electrochemical reaction [68]. Therefore, the minimum electrical voltage required for the electrolysis process is equal to the change in the Gibbs free energy ΔG given by Eqs (2.6) and (2.7), where n is the amount of charges (electrons) transferred during the reaction and F is the Faraday constant.

$$-\Delta G = nFE^0 \tag{2.6}$$

$$E^0 = \frac{-\Delta G}{nF} \tag{2.7}$$

The equilibrium cell voltage of the electrolysis cell is therefore the theoretical minimum voltage required to provide the electrical input for the water electrolysis reaction which is equal to 1.23 V under standard state conditions (ΔG = 237.14 kJ mol^{-1}). However, this is only possible if the thermal part of the energy ($T\Delta S$ in Eq. 2.5) is supplied by an external heat source [18]. Without an external heat source, the thermal part of the energy for the reaction must be delivered by electrical energy, and hence a higher cell voltage than the equilibrium value is required. This cell voltage is called *thermoneutral voltage* and is determined from the enthalpy change ΔH of the electrolysis reaction which is 1.48 V under standard-state conditions (ΔH = +285.83 kJ mol^{-1}). Electrolysis is endothermic below the thermoneutral voltage, and exothermic above it, with the production of waste heat.

2.3.1 Open circuit voltage

The open circuit voltage (OCV) is the cell potential when no current is passed through the cell. Under standard conditions, it is equal to the equilibrium voltage computed from the Gibb's free energy. However, the Gibb's free energy changes with temperature, pressure and concentration and therefore, the Nernst equation is

used to compute the OCV under such non-standard conditions [69]. The Nernst equation is expressed in Eq. (2.8) as:

$$E_{cell} = E^{\circ} + \frac{RT_{cell}}{2F} \ln \frac{P_{H_2} P_{O_2}^{1/2}}{a_{H_2O}} \quad (2.8)$$

Where R is the universal gas constant (8.314 J $mol^{-1}K^{-1}$), T_{cell} is the cell temperature, P_{H_2} and P_{O_2} are the partial pressures of hydrogen and oxygen gases and a_{H_2O} is the activity of water usually considered to be unity.

2.4 Overpotentials

Cell operation conditions inevitably cause the cell system to deviate from the equilibrium state and the actual cell potential, E_{cell}, is increased from its equilibrium value, E^0 because of irreversible losses. This phenomenon is often called polarization, overpotential or overvoltage, and is expressed in Eq. (2.9) as:

$$\eta = E_{cell} - E^0 \quad (2.9)$$

The overpotentials cause the cell potential to be higher than the ideal potential and originate primarily from three sources: (i) Activation or charge transfer overpotential, (ii) Ohmic or electron transfer overpotential, and (iii) Concentration or mass transport overpotential.

The potential of a PEMWE cell therefore consists of the open circuit voltage, activation overpotential, ohmic overpotential and the concentration/mass transport overpotential. The relationship can be expressed by Eq (2.10):

$$E_{cell} = E_{ocv} + \eta_{act} + \eta_{ohm} + \eta_{conc} \quad (2.10)$$

Where E_{ocv} is the open circuit voltage, η_{act} is the overpotential due to charge transfer processes in the electrochemical reactions, η_{ohm} is the ohmic overpotential caused by the electrolyser cell resistances., and η_{conc} is the diffusion overpotential caused by the mass transport processes in the cell.

2.4.1 Activation overpotential

The initiation of an electrochemical reaction on the electrode surface requires overcoming of an energy barrier known as activation energy. The energy loss associated with overcoming this energy barrier is termed activation overpotential. It is influenced by physical and chemical parameters such as catalyst property, catalyst utilization/distribution, electrode morphology, operating temperature, and active reaction site [70]. Assuming only charge transfer limitations (which is a reasonable approximation at low current densities), the activation overpotential is typically described by the Butler-Volmer equation (Eq. 2.11). This equation relates the current to the activation overpotential at each electrode and is given as:

$$i = i_0 \left[exp\left(-\frac{\alpha n F \eta_{act}}{RT}\right) - \exp(-\frac{(1-\alpha) n F \eta_{act}}{RT}) \right] \tag{2.11}$$

Where i_0 is the exchange current density which is the cell anodic or cathodic current under equilibrium conditions, α is the charge transfer coefficient and n is the number of electrons transferred in the elementary charge transfer step. The first exponential term in Eq. (2.11) is the rate of the anodic direction while the second exponential term is the rate of the cathodic direction. The exchange current reflects the intrinsic rates of electron transfer of an electrode reaction; the higher the exchange current, the faster the electrode reaction. The charge transfer coefficient determines the geometry of the energy barrier and indicates whether the electrode reaction favours the anodic or the cathodic direction at an applied potential [71].

At sufficiently small activation overpotentials, according to the Taylor series expansion of the exponential function, Eq (2.11) can be approximated as:

$$i = \frac{i_0 n F \eta_{act}}{RT} \tag{2.12}$$

Eq. (2.12) shows that the current has a linear relationship to the activation overpotential in a narrow potential range near the equilibrium potential. The slope of the linear plot is also called the charge transfer resistance, R_{ct}.

$$R_{ct} = \frac{RT}{nF i_0} \tag{2.13}$$

R_{ct} is a measure of the kinetic capability of the cell reaction and can be measured directly by some electrochemical analysis methods, such as electrochemical impedance spectroscopy.

At high activation overpotential, one of the two terms in Eq. (2.11) is negligible and Butler-Volmer equation takes the form described in Eq. (2.14):

$$i = i_0 e^{-\frac{\alpha n F \eta_{act}}{RT}} \tag{2.14}$$

Or in another form,

$$\eta_{act} = \frac{RT}{\alpha n F} \ln i_0 - \frac{RT}{\alpha n F} ln\, i = a + b \ln i \tag{2.15}$$

This exponential relationship between the current and activation overpotential is called the Tafel equation and was established experimentally by Swiss chemist Julius Tafel in 1905. In the Tafel equation, $\frac{RT}{\alpha n F} \ln i_0$ is the overpotential at the unit current density, and $b = -\frac{RT}{\alpha n F}$ is the Tafel slope reflecting the rate of change of the overpotential as a function of the logarithm of the current density. A typical Tafel plot is shown in Figure 2.4.

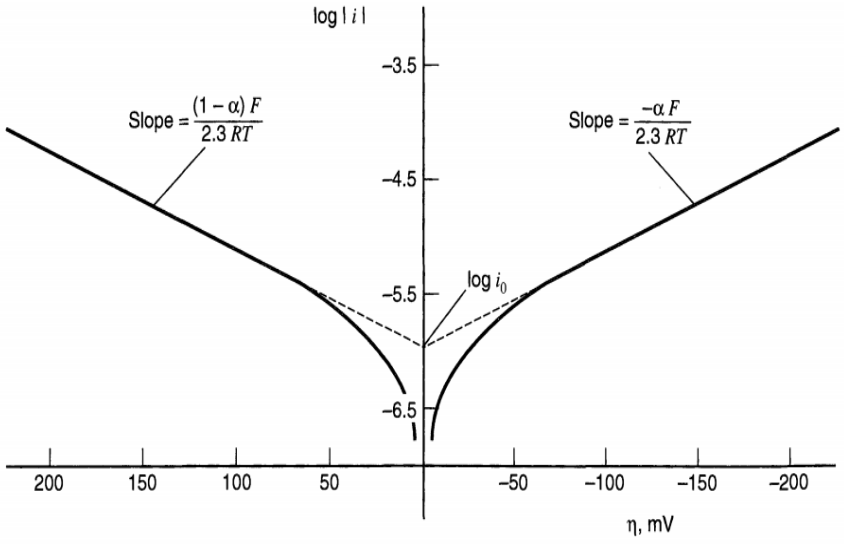

Figure 2.4. Tafel plots for anodic and cathodic branches of the current-overpotential curve for O + e ⇆ R with α = 0.5, T = 298 K, and $i_o = 10^{-6}$ A cm^{-2}. Reproduced from Ref [72].

The activation overpotential can be calculated individually for the anode, η_a, and cathode, η_c and are presented in Eq. (2.16) and (2.17):

$$\eta_a = \frac{RT}{\alpha_a nF} \ln\left(\frac{i}{i_{a,0}}\right) \tag{2.18}$$

$$\eta_c = \frac{RT}{\alpha_c nF} \ln\left(\frac{i}{i_{c,0}}\right) \tag{2.19}$$

where α_a and α_c, are the charge transfer coefficients of the anode and cathode respectively. Many reactions tend towards symmetry, so with no information available both charge transfer coefficients is usually approximated as 0.5. In water electrolysis, $n = 2$. $i_{a,0}$ and $i_{c,0}$ are the exchange current densities (A cm^{-2}) for the anode and cathode respectively, and i is the current density of the electrolysis cell.

During the global reaction, each electrode makes a non-symmetric contribution to the overall activation overpotential. The value of the exchange current density at the anode electrode is typically much lower than the cathode (e.g. 10^{-7} A cm^{-2} in Pt-Ir anode, and 10^{-3} A cm^{-2} in Pt cathode at 80 ºC) [73]. Thus the cathode contribution is usually assumed to be negligible. The exchange current densities of the anode and the cathode are a function of the cell material, electrocatalyst used, morphology, and temperature.

2.4.2 Ohmic overpotential

The ohmic overpotential is due to ohmic losses within the cell. This includes the electronic losses due to the resistance of the flow-field plates, electrodes, PTL etc. The dominant ohmic losses are the ionic losses caused by the resistance to the proton transport through the PEM [70]. Ohmic overpotential follows Ohm's Law. The ohmic overpotential is linearly proportional to the applied current i and can be expressed as Eq. (2.18) [74]:

$$\eta_{ohm} = R_{cell} i \tag{2.18}$$

Where R_{cell} is the ohmic resistance of the cell. The magnitude of the ohmic resistance is a combination of the resistances of the electrodes, PTL and flow-field plates.

2.4.3 Mass transport overpotential

The mass transport overpotential (or concentration overpotential) takes into account the mass transport limitations that occur at high current densities inside the porous structures (electrodes, PTLs and flow-field channels) of the PEMWE [27]. Since the electrolysis reaction takes place at the membrane–electrode interface, all the mass flows must be transported through the porous electrode: water from the flow channels through the PTLs to the catalyst layer, and the produced hydrogen and oxygen gas from the reaction sites through the PTL and flow channels to the exit. The liquid water encounters resistance (which increases with flow as it flows through the electrode); energy is lost in the process giving rise to a diffusion overvoltage. The evolution of the mass transport losses takes two major forms: diffusion, η_{diff} and bubble η_{bub} overpotentials.

Diffusion dominates mass transport losses only at low current densities, however PEMWE are increasingly operated at high current densities, sometimes above 3 A cm^{-2}. At such high current densities, the production of the gas phase in the form of bubbles shields the active area, distorts the contact between the electrode and electrolyte, and reduces the catalyst utilization. This results in an increase in the local current density and the so-called bubble overpotential, which increases exponentially with increasing current densities [75] and is shown in Figure 2.5.

Thus, concentration overpotential becomes increasingly important at high current densities where the water demand and gas production becomes large. The mass flow of the water/gas mixture through the porous electrodes and the PTLs is mainly a diffusion phenomenon and is described by Fick's law [27]. Fick's law relates the diffusive flux to the concentration under the assumption of a steady state. It postulates that the flux goes from regions of high concentration to regions of low concentration, with a magnitude that is proportional to the concentration gradient, or in simplistic terms, the concept that a solute will move from a region of high concentration to a region of low concentration across a concentration gradient, the porous electrode in this case[76]. For a one-dimensional case, Fick's law is presented in Eq. 2.19 as:

$$J = -D\frac{\partial \phi}{\partial x} \tag{2.19}$$

where J is the "diffusion flux", J measures the amount of substance that will flow through a small area during a small time interval, D is the diffusion coefficient or diffusivity in dimensions, ϕ is the concentration, and x is the position. The negative sign indicates that J moves in the opposite direction with the gradient.

In the PEMWE, the greatest concentration overpotential influence is attributed to the products transport limitations, where the inability to remove the product gases as quickly as they are produced leads to increase in their concentration at the reaction sites and hence a slowing of the reaction kinetics.

The concentration overpotential at the anode and cathode can be calculated using the Nernst equation and is given by Eq. (2.20) [77]:

$$\eta_{conc} = E_{conc,a} + E_{conc,c} = \frac{RT_a}{4F} ln\left(\frac{C_{O_{2,m}}}{C_{O_{2,m}0}}\right) + \frac{RT_c}{2F} ln\left(\frac{C_{H_{2,m}}}{C_{H_{2,m}0}}\right) \quad (2.20)$$

where $C_{O_{2,m}0}$ and $C_{H_{2,m}0}$ indicate the oxygen and hydrogen concentrations respectively at the membrane-electrode interface under a given operating condition.

2.4.4 Polarization Curves

Figure 2.5 depicts a theoretical voltage-current density curve (polarization curve) of a PEM water electrolyser, showing the contributions of the three loss mechanisms: the activation, ohmic and mass transport losses to the overall cell polarization.

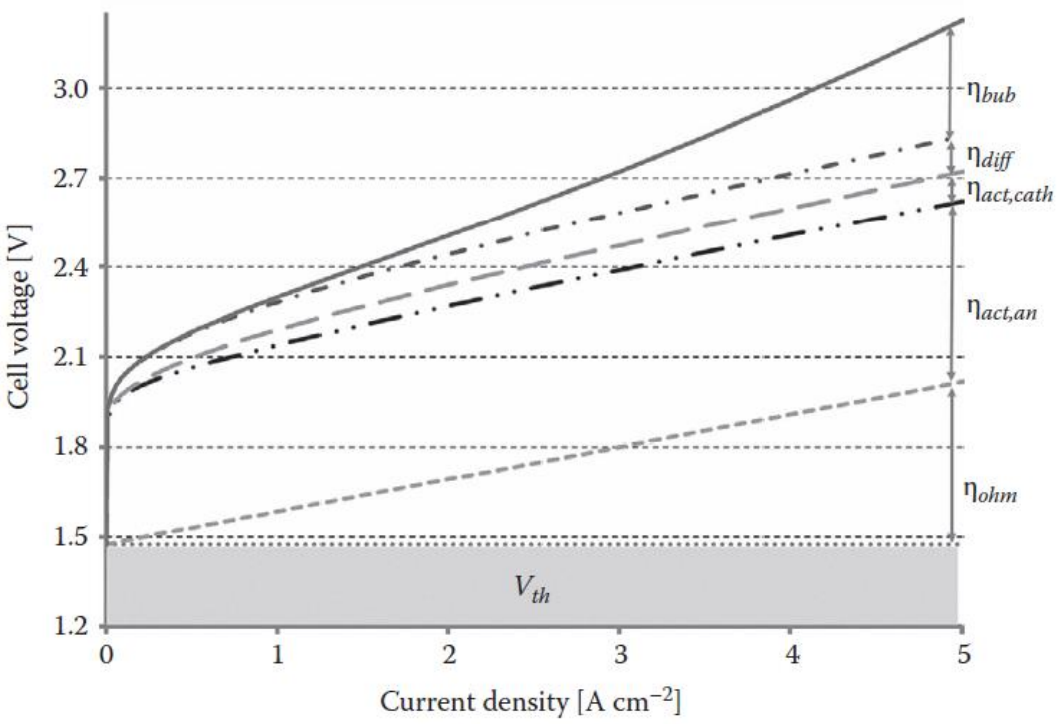

Figure 2.5. Simulated overpotentials in a conventional PEM Water Electrolyser cell. Adapted from [18].

Since the PEMWE components are electrically arranged in a series connection, all the voltage losses from the anode and cathode sides can be summed up to give the total cell polarization. The cell voltage, E_{cell} which is a measure of the total amount of electrical energy demand for water-splitting, then results from the sum of the reversible cell voltage, and all irreversible losses within the cell.

$$E_{cell} = E^0 + \eta_{act,an} + \eta_{act,cat} + \eta_{ohm} + \eta_{diff} + \eta_{bub} \qquad (2.21)$$

Figure 2.5 illustrates the cell contribution of the anode and cathode activation overpotentials, the reversible cell voltage, E^0, and the ohmic overpotential to the total electrical energy demand for water splitting by the PEMWE. It is based on an electrochemical model with data input on real cell operation.

2.5 Electrolysis Efficiency

Energy efficiency is defined as the energy output that can be produced with a given input of energy. The efficiency of the electrolysis cell can be expressed in a

number of ways, depending on how the electrolysis system is assessed and compared [13].

The efficiency of an electrolysis cell at a given current density is inversely proportional to the cell voltage. A higher voltage results in more hydrogen production but at a lower efficiency. Cell voltage of about 2 V is typically selected if operational efficiency is desired over the size and capital cost of the electrolyser [4].

The efficiency of a PEMWE cell is an important parameter to assess the energy cost of the process.

2.5.1 Electrical Efficiency

The electrical efficiency η_{el} is expressed as the proportion of chemical energy generated W_{H_2} compared to the electrical energy W_{el} required and is represented in Eq. (2.22) as:

$$\eta_{el} = \frac{W_{H_2}}{W_{el}} = \frac{\dot{N}_{H_2} H_V}{E_{cell} i t} \tag{2.22}$$

Where $\dot{N}_{H_2}$ is the molar rate of hydrogen produced, H_V is the heating value of hydrogen, E_{cell} is the cell voltage, i is the current and t is the time.

2.5.2 Voltage Efficiency

The voltage efficiency V_{eff} relates the theoretically required amount of energy for the reaction, i.e., the reaction enthalpy ΔH_R^0 to the actual electrical energy input into the cell expressed in Eq. (2.23) as:

$$\eta_{Voltage} = \frac{\Delta H_R^0}{2F E_{cell}} \tag{2.23}$$

2.5.3 Faradaic Efficiency

The faradaic efficiency is a measure of the number of electrons that are transported in the external circuit to the surface of electrode for conducting the electrochemical reaction either oxygen evolution reaction (OER) or hydrogen evolution reaction (HER) and other electrochemical reactions in the electrolytes. It is defined as the

ratio between experimentally evolved volume of gas (hydrogen or oxygen) and theoretically calculated volume of gas, as shown in Eq. (2.24):

$$\eta_{Faraday} = \frac{V_{H_2}(Produced)}{V_{H_2}(Calculated)} \tag{2.24}$$

The theoretical volume of gas can be calculated by the Faraday's second law, based on the current density, electrolysis time and electrode area by assuming a 100% Faradaic efficiency, whereas the practical amount produced in the experiment can be measured by water-gas displacement method or gas chromatography analysis [78].

2.5.4 Thermal Efficiency

The thermal efficiency defines the additional cell potential required above the open-circuit voltage to maintain the thermal balance throughout the cell. Theoretically, thermal efficiency greater than 100% is possible if the reaction is endothermic [45]. The enthalpy change of the water-splitting reaction is employed as the energy input for determination of thermal efficiency. Thus, if the electrolyser operates below the thermoneutral voltage, the thermal efficiency can be higher than 100%. It is expressed in Eq. 2.25 as:

$$\eta_{Thermal} = \frac{\Delta H}{\Delta G + losses} = \frac{E_{\Delta H}}{E_{cell}} \tag{2.25}$$

Where $E_{\Delta H}$ is the equilibrium cell voltage equal to 1.48 V at 25°C. The electrolysis cell is exothermic at cell potential above 1.48 V, and endothermic at cell potential below this value [13].

Based on the energy efficiency assessment, energy efficiency of the electrolysis cell can be improved in two broad ways: (1) thermodynamically reducing the energy needed for the water-splitting reaction such as by increasing the operating temperature or pressure; (2) reducing the energy losses in the cell, which can be realized by minimizing the dominant overpotentials at various current densities [13].

2.6 PEMWE Operating Conditions

PEMWE operation is highly influenced by various thermodynamic and electrochemical operating conditions such as temperature, water feed rate, pressure, current density etc.[32]. These operating conditions directly influence cell potential and performance losses in the cell and their alteration can be either beneficial or detrimental in terms of performance, efficiency, cost, etc.

2.6.1 Temperature

The temperature within the PEM water electrolyser has a significant impact on the performance. The operating temperature range in the PEMWE cell is 20–90 ºC with the upper bound set largely due to MEA stability issues at higher temperatures [31], [32], [79]. Generally, an increase in operating temperature leads to reduction of activation/kinetic and ohmic losses in the PEMWE cell, due to faster reaction kinetics and higher ionic conductivity of the membrane at high temperatures [56]. Figure 2.6 illustrates the typical effect of temperature on the ohmic resistance and overall electrolyser performance. At higher temperature, a lower applied voltage is required to reach the same levels of current density (better performance). Optimal temperature is suggested to be between 70 and 90 ºC as a trade-off between improved performance and material stability issues at high temperature. However, slightly lower temperatures (60–70ºC) are used in commercial systems, due to stability issues with ion-exchange resins used to maintain purity of the process water [32].

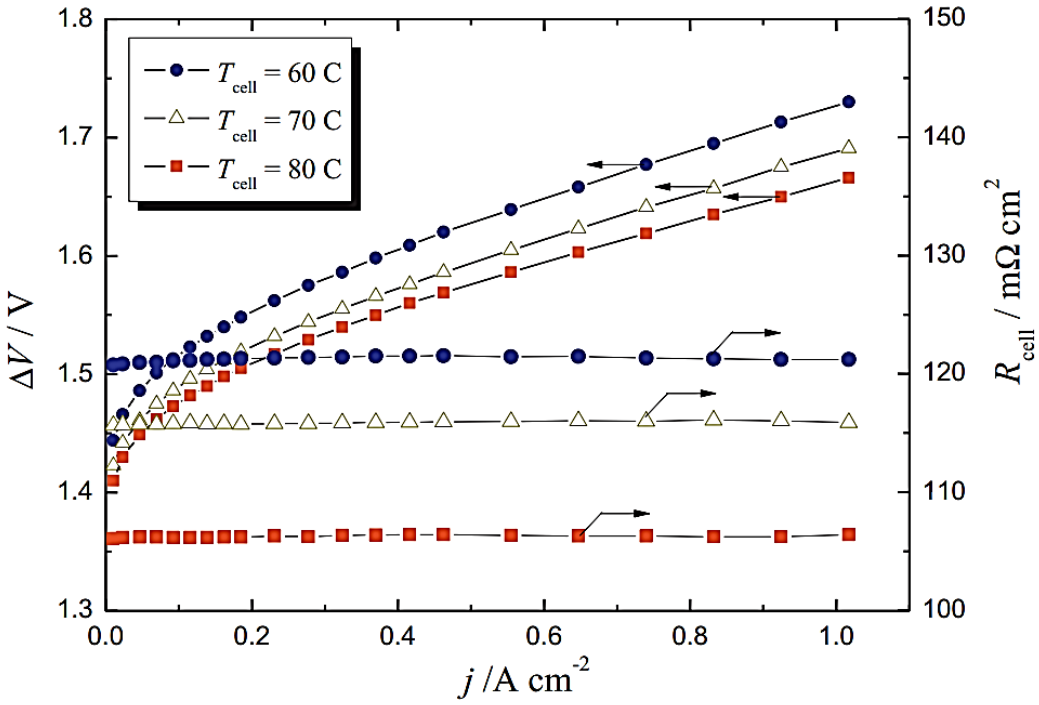

Figure 2.6. Cell potential (ΔV) and cell resistance (R_{cell}) versus current density (j) up to 1.0 A cm^{-2} during electrolysis at different temperatures. Reproduced from Ref [56].

2.6.2 Pressure

The PEMWE system can be operated at pressures significantly higher than ambient pressure, depending on the end use [13]. Two modes of pressurized operation are generally employed: balanced (similar pressure on hydrogen and oxygen sides) and differential (significantly higher pressure at the cathode). Commercial PEMWEs typically operate at pressures in the range 30–50 bars [27]. However, on the prototype level, direct electrochemical compression in PEMWEs up to 700 bar (differential) pressure has been demonstrated [28], [68]. Increased pressure operation offers specific benefits compared to atmospheric operation: more efficient transport of biphasic (liquid–gas) mixture across the PTL due to decrease in volume of gas phase (bubbles) with increasing pressure and savings on compression costs and allows direct hydrogen gas storage.

The main shortcoming of high pressure operation is the gas cross-permeation through the PEM which increases when the operating pressure is raised. Hydrogen diffuses into oxygen due to the higher diffusivity of hydrogen in the PEM; oxygen

also diffuses into hydrogen but to a lesser extent. This cross-diffusion leads to lower purity gas production and poses significant safety risk (the lower limit of explosivity of H_2 in O_2 is 4 vol%) [81]. Also, cross-diffusion generates parasitic current akin to an internal cell short-circuit, leading to lower current efficiencies, and increased ohmic and kinetic overpotential. Therefore, for most practical applications an upper limit of 130 bars (2,000 psi) is recommended [82].

Theoretically, the compression loss in a PEM electrolyser can be predicted by the Nernst equation (see Eq 2.10), where assumptions for the activity of gases and water are needed to calculate the equilibrium potential. An assumption of ideal gas behaviour for both H_2 and O_2 can be made for the solubility of hydrogen and oxygen in water up to 100 bars, because at thermodynamic equilibrium conditions only the dissolved gas in the water is in contact with the electrodes. Consequently, the activities can be expressed by the partial pressures. The activity of water is assumed to be unity.

According to the Nernst equation, the thermodynamic cell voltage at 60°C increases by 33 mV per decade of pressure for differential pressure operation (O_2 at atmospheric pressure) and by 50 mV per decade for balanced pressure operation (both gases at higher pressure) [32]. Figure 2.7 illustrate the influence of increased operating pressure on the performance of an operational PEMWE cell.

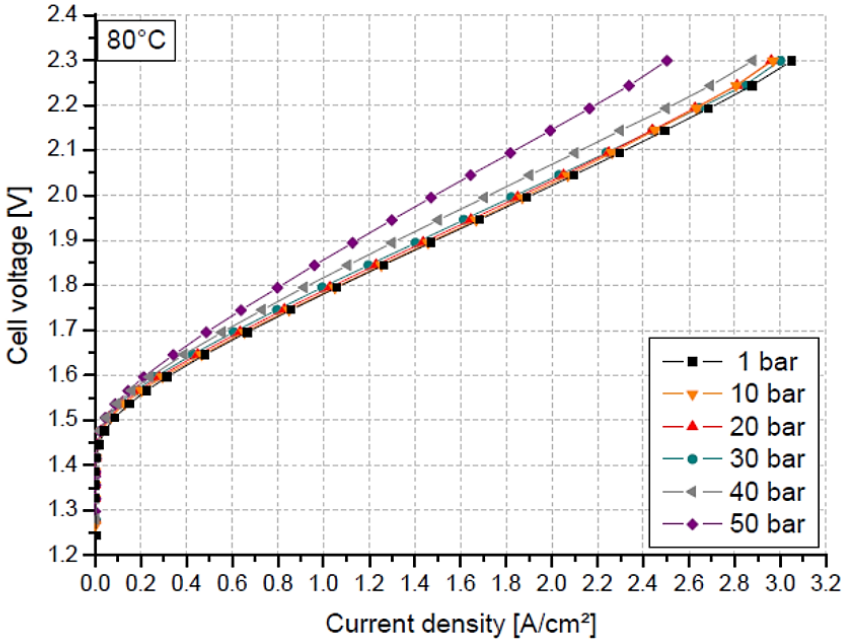

Figure 2.7. Electrolyser operation at constant temperature of 80°C and various operational pressures. Adapted from Ref [83].

2.6.3 Current density

The amount of gases produced in the PEM electrolyser cell is directly proportional to the current density applied. As a result, high current density operation is advocated for increased H_2 production per unit cell area to lower the capital expenses of the PEMWE system. Recent research efforts have focused on widening the range of operational current densities from 2.0 A cm^{-2} in existing commercial electrolysers, to as much as 20 A cm^{-2} [84].

Operation at elevated current densities provides an opportunity for controlling the effect of gas crossover. Cross-diffusion of hydrogen and oxygen at high differential pressure poses significant safety risk as discussed in the previous section. At high current densities, the hydrogen in oxygen gas will be diluted by the increased oxygen production rate, thus reducing the safety risk of elevated pressure operation [32]. Although, the hydrogen permeation rate as function of current density is not yet fully understood and might be influenced by the electro-osmotic drag of water and catalyst layer heterogeneities [85].

The negative aspect of elevated current density is the dominance of irreversible losses, for example, Joule heating, at high current density, which makes a cooling

system necessary to alleviate degradation. Furthermore, concerns regarding homogeneity of current distribution in the electrolyser system are intensified at high current density, as inhomogeneous current distribution can result in faster local ageing and accelerated degradation [86]. More importantly, mass transport losses are elevated at high current density due to accumulation of produced gases at the electrode leading to surface coverage of the electrocatalyst layer; thus, effective transport of liquid water to the electrode and removal of product gases becomes a critical issue at high current density[87]–[89].

2.6.4 Water circulation and feed rate

The supply of water to the electrode is an important operating parameter of the PEMWE operation [18], [90]. Water distribution plays a key part in sustaining the reaction, in heat distribution/removal, and the transport of produced gas out of the cell [91]. Purity of the water is also vital for efficient operation as impurities could deposit on the electrode surface impeding the ion transfer and electrochemical reactions. Water supply to the PEMWE cell can be realized as anode feed, cathode feed or as both anode and cathode feed [18]. In most cases, the cell is fed at the anode because the water is consumed at this side. In this case, water is transported to the cathode by electro-osmotic drag. Cathode feed is used in some specialized applications, for instance, in manned aerospace application [92] and medical isotope production [93]. In this case, water migrates through the membrane to be consumed at the anode. Thus, water diffusion becomes the rate-determining step and prevents operation at high current densities and as a result larger cell areas are required for equivalent hydrogen production.

Studies have shown that water feed rate through the PEMWE cell impacts cell performance [91], [94]. Figure 2.8 illustrates a PEM electrolyser operating with varying water feed rates where performance was seen to deteriorate with increasing water feed rate when operating at room temperature and atmospheric pressure.

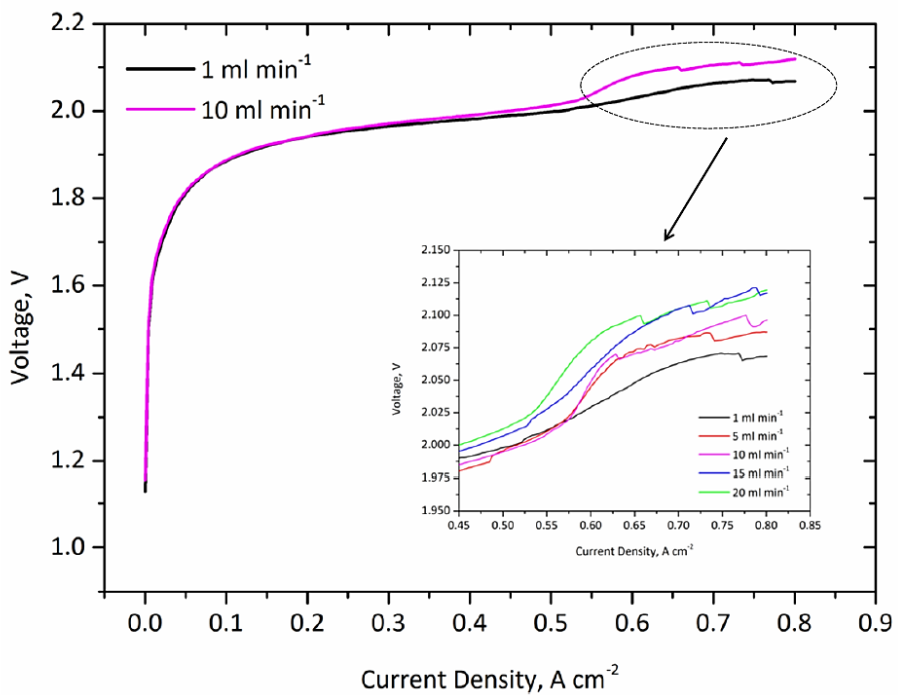

Figure 2.8. Performance of PEMWE cell at varying water feed rates. Inset shows the variation of performance with feed rates ranging from 1 ml min^{-1} to 20 ml min^{-1} at room temperature and ambient pressure. Reproduced from Ref [95].

The molar rate at which water is reacted in the PEM electrolyser is given by Faraday's law (Eq. 2.26):

$$\dot{N}_{H_2O} = \frac{i}{2F} \tag{2.26}$$

where $\dot{N}_{H_2O}$ is the rate of water consumption (molar basis), i is the applied current, and F is the Faraday constant (96485.3 C mol^{-1}). This water consumption rate gives the amount of water consumed at a given current. The water stoichiometry ratio, ζ is the ratio of water feed rate to the amount of water consumed by the reaction in a single cell at a given current density, and is an important index of PEMWE operation defined as [91]:

$$\zeta = \frac{G_{circ}}{G_{cons} + G_{drag}} \tag{2.27}$$

Where G_{circ} is the mass flux of circulated water, G_{cons} is the mass flux of water consumed , G_{drag} is the mass flux of water transported from the anode to the cathode by electro-osmotic drag.

The relation between this ratio and the current density can be calculated independent of the type of flow-field configuration. Theoretically, a value of ζ=1 is sufficient for the electrolysis reaction. However, during cell operation, ζ is often set to much higher value to avoid membrane drying out and ensure cell safety. For instance, water feed rate of 30 ml min^{-1} at current density of 3 A cm^{-2} corresponds to a ζ of ~18. Typical industrial systems supply around 50-300 times the water required at high current densities to ensure that enough water reaches the catalyst and for temperature control [54].

2.7 Mass Transport Phenomena in the PEMWE

As discussed in Chapter 1, the PEMWE must be continually supplied with water and electricity to sustain the electrolysis process. Simultaneously, the hydrogen and oxygen gases produced must be continuously removed to avoid screening of the reaction surface. This concurrent process of reactant supply and product removal is known as *"mass transport"* [96]. And as will be explained in this section, this seemingly simple task can turn out to be quite complicated with flow channel design, porous transport layer microstructure, gas-bubble dynamics and two-phase flow regimes all playing a part [18].

The mass transport is important because ineffective or inefficient mass transport lead to poor electrolyser performance especially at high current densities since performance is dictated by the reactant and product concentrations at the electrocatalyst layer rather than at the cell inlet [27], [97]. Thus, either of water starvation or product gas accumulation at the electrocatalyst layer will impede performance. This loss of performance is called *concentration loss or mass transport loss*; and can be minimized by improved understanding and careful optimization of mass transport processes: gas-bubble dynamics, two-phase flow regimes and the design of flow structures of the PEMWE cell [91], [97], [98].

The porous transport layer and the flow-field/bipolar plate are the two main components that directly influence mass transport losses in the PEMWE, and are thus the focus of this research. They both mediate the flow of water and gas between the reaction active sites and the cell inlet/outlet [59], [91]. The key difference between mass transports in the two components is that of structure and

length scale; hence, leading to different mass transport mechanisms and approaches to their characterization. The dimensions of flow channels in the flow-field plate are usually on the millimetre or centimetre scale and the flow patterns typically consist of geometrically precise channel arrays that are amenable to the laws of fluid mechanics. In contrast, the PTL exhibit structure consisting of pores rather than channels with pore dimension on a micrometre length scale. The circuitous, sheltering geometry of these PTLs insulates gas molecules from the convective forces present in the flow channel. Sheltered from convective flow, gas transport through the PTL is dominated by diffusion [96].

2.7.1 Mass Transport in the PEMWE Flow-field

The key function of the PEMWE flow-field is to supply water through the PTL to the electrocatalyst layer and remove produced gas from the cell. Hence, the flow is a gas-liquid two-phase flow controlled by the physics of bubble evolution and two-phase flow in (micro)-channels, and by dictating the water availability at the electrocatalyst layer and the residence time/bubble size of the product gas, the flow field design is linked to the cell performance.

2.7.1.1 Electrolytic Gas-bubble Evolution

Gas evolution in the electrolysis cell proceeds in three stages: nucleation, growth and detachment [99]. Bubbles nucleate at the PTL/flow-field interface when the dissolved gas concentration reaches a critical value. The bubbles grow by coalescence with other bubbles and finally detach once the forces pulling them away (buoyancy and inertia forces) overcome the surface adhesive force (surface tension and hydrodynamic drag forces) [100]. Several operational parameters such as water feed rate, cell orientation and current density can influence the bubble formation, detachment, shape and size [91]. Thus, the influence of these operating parameters on the gas-bubble evolution in the PEMWE system, as well as the factors which govern the rate of gas bubble evolution, must be well understood.

The bubbles formed and attached at the PTL/flow-field interface get detached only after they reach a critical diameter, determined by a balance of forces that either favours or opposes bubble detachment [101], [102]. They are:

1. *Buoyancy force* F_b : the force that results from pressure exerted on the vapour bubble by the surrounding liquid. The buoyancy force acts on the bubble surface in contact with liquid and wall. The bubble's upward motion is driven by its buoyancy i.e. the weight of liquid displaced. The buoyancy force F_b is given by Eqs. (2.28) and (2.29):

$$F_b = \rho_l V_b g \tag{2.28}$$

$$V_b = \frac{4}{3}\pi r_b^3 \tag{2.29}$$

Where ρ_l is the liquid density, V_b is the volume of bubble and r_b is the radius of the bubble.

2. *Surface tension force:* the attractive force that holds the bubble to the solid surface, given by:

$$F_\gamma = \pi D_b \gamma sin^2(\theta) \tag{2.30}$$

Where D_b is the bubble diameter, γ is the liquid surface tension and θ is the contact angle.

3. *Inertia force:* The vapour bubble gains an initial acceleration from the unbalanced net force in the upward direction as it departs the surface. The bubble attains a certain momentum as a result of this acceleration which causes the liquid field to impart inertia. Due to this inertia, the bubble acceleration decreases, making the velocity component reach its asymptotic value known as terminal velocity. The inertia force is thus dependent on the mass of surrounding liquid displaced by the bubble during its motion. As it moves, the bubble effectively entrains an added mass of fluid equal to half of the displaced fluid mass [103]. This entrained mass is also referred to as the *added mass* of bubble. The bubble motion is resisted by this added mass imposing an inertia force F_i which is calculated as:

$$F_i = Ma_b \tag{2.31}$$

Where a_b is the initial acceleration of the bubble and M is the mass of the bubble which is equal to the entrained mass of bubble M_e. Hence the inertia force is given as:

$$F_i = \rho_l \left(\frac{2}{3}\pi r^3\right) a \tag{2.32}$$

4. *Drag force:* force exerted on the bubble during motion due to the viscosity of water. The direction of drag force is always opposite to the flow direction.

The bubble gains an initial velocity on departure from the surface which imparts motion to the bubble, and eventually gives rise to the drag force. The drag force is approximated by Stokes' equation given by Eq. (2.33):

$$F_d = 6\pi\rho_l\mu r v \tag{2.33}$$

Where μ is the kinematic viscosity of the fluid and v is the bubble velocity within the fluid.

For micro-channels, such as the ones encountered in PEMWEs, bubble detachment is strongly influenced by the PTL/flow-field interface, the channel geometry and the interaction of the various forces [102]. For instance, Zhuang *et al.* [102] examined the characteristics of formation, growth and detachment of microbubbles on various surfaces such as Pt on carbon cloth, planar Pt surface, carbon paper etc. in a micro-direct methanol fuel cell study. The result revealed significant variations in the size uniformity and diameter of the bubbles detached from the surface. Different inclination angles also showed various ease of bubble detachment.

For a bubble growing and detaching from a single pore of known diameter, d_p, and the surface contact angle of θ. Under the assumption that the bubble detachment process is dominated by buoyancy and surface tension effects, the force balance predicts that the diameter of the bubble at detachment, or bubble detachment diameter, d_b is given by Eq. (2.34) [104]:

$$d_b = \left(\frac{4d_p\sigma\sin\theta}{g(\rho_l - \rho_g)}\right)^{\frac{1}{3}} \tag{2.34}$$

2.7.1.2 Two-Phase flow in Channels

Liquid water and product gases distribute themselves in different flow regimes in vertical flow channels depending on geometry and operating conditions. The typical flow regimes are dispersed bubbly flow, slug flow, churn flow and annular flow [59]. These flow regimes in vertical upward flow in channels are illustrated schematically in Figure 2.9 which also includes plug flow as a transitional flow between bubbly and slug [59].

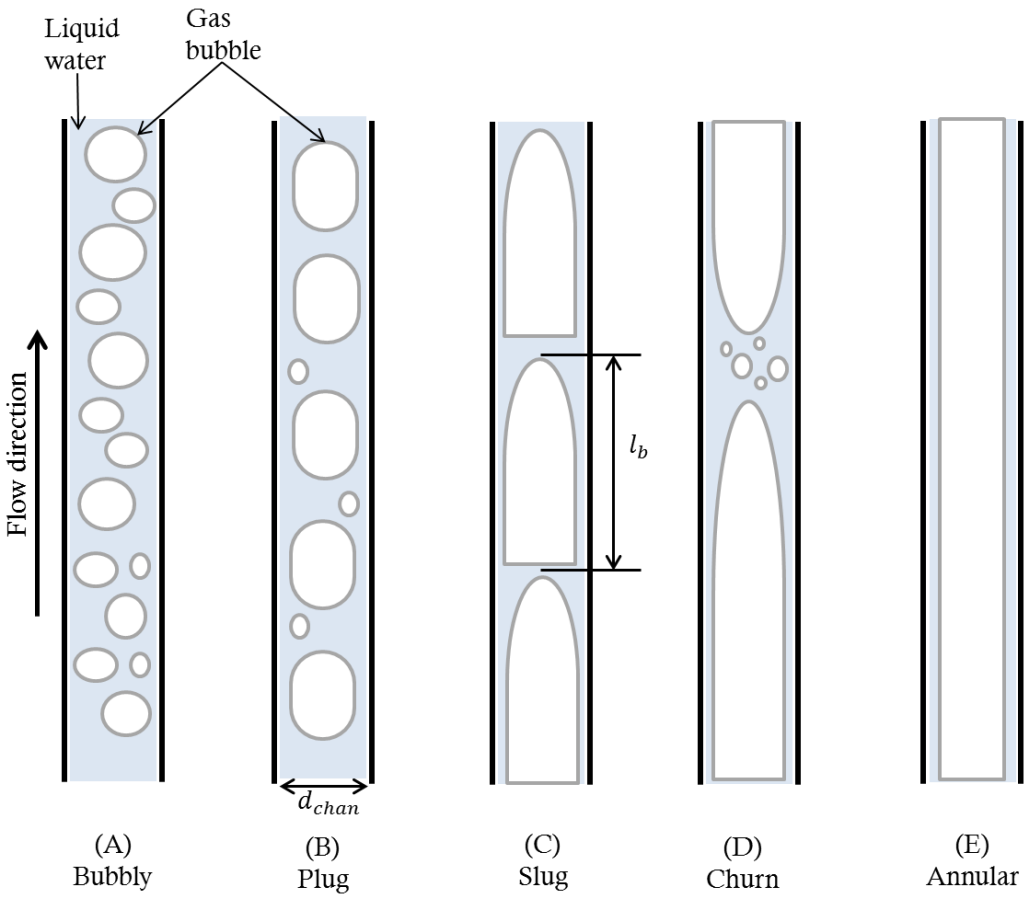

Figure 2.9. Schematic flow patterns of gas-liquid two-phase flow in channels. Adapted from Ref [59].

1. *Bubbly flow:* Here, the gas is distributed as discrete small bubbles in the continuous liquid phase. This regime is characterized by spherically-shaped bubbles with length l_b considerably smaller than the channel diameter, d_{chan}. As the gas fraction increases, a transitional regime called elongated bubble flow or *plug flow* is developed, characterized by elongated bubbles with length l_b slightly greater than channel diameter, d_{chan}.
2. *Slug flow:* With further increase in gas fraction, bubble coalescence increases as the mean size of the bubbles increases until bullet-shaped bubbles called *slugs* form. These slugs are periodic, and may exist with discrete bubbles still present in the interim. This flow regime is characterized by bullet-shaped bubbles also known as Taylor bubbles, where $l_b \gg d_{chan}$.
3. *Churn flow:* Further increase in gas velocity leads to a breakdown of large bubbles in the slug regime and flow becomes highly chaotic and foamy. This

chaotic condition occurs when the downward-acting gravitational force and upward-acting shear forces balance out. This flow pattern is an intermediate regime between slug and annular flow regimes.

4. *Annular flow:* This is a steady flow regime characterised by continuity of the gas phase along the channel core. This regime ensues when the shear force of the high velocity gas on the liquid film exceed the gravitational force. The gas flows as a continuous phase up the centre of the channel and the liquid phase flows only along the walls of the channel as a film [59].

A number of studies have shown that the two-phase flow pattern in the channels of the PEMWE can be characterized by the superficial velocities of the gas and liquid (j_G and j_L, respectively), the flow quality, and the mass flux [59], [91], [94]. The superficial velocity is given in Eq. (2.35) and (2.36) as follows:

$$j_G = \frac{(G_G + G_L)x}{\rho_G} \tag{2.35}$$

$$j_L = \frac{(G_G + G_L)(1 - x)}{\rho_l} \tag{2.36}$$

Where G_G and G_L are the mas fluxes of the gas and liquid, ρ_G and ρ_l are the densities of gas and liquid, respectively, and x is the quality of the two-phase flow at an arbitrary location along the channel, and is defined in Eq. (2.37) as follows [59]:

$$x = \frac{G_G}{G_L + G_G} \tag{2.37}$$

Where G_l and G_g are the mass flux of the liquid and gas respectively.

The mass flux of oxygen gas at the exit of the anode channel is calculated according to Faraday's law, assuming 100% Faradaic efficiency and complete entrainment of all the oxygen gas generated at the anode. Thus, mass flux of oxygen gas at the exit is given as:

$$G_{O_2} = \frac{iAM_{O_2}}{4Fn_{ch}a} \tag{2.38}$$

Where i is the current density, A is the total area of the electrode, M_{O_2} is the molar weight of oxygen, F is the Faraday constant, n_{ch} is the number of channels and a is the cross-sectional area of the channel.

However, not all the water supplied is present for gas entrainment in the channel since water is consumed by the reaction. Hence, the total mass flux of water consumed per channel (also follows Faraday's law) is given as:

$$G_{cons} = \frac{iAM_{H_2O}}{2Fn_{ch}a} \tag{2.39}$$

Where M_{H_2O} is the molar weight of water. In reality, some of the water supplied is moved along with protons through the PEM to the anode compartment by *electro-osmosis* [105]. This mass flux of water dragged by electro-osmosis G_{drag} is estimated to be ~10 times that of G_{cons}. Therefore, the x_{exit} of the two-phase flow in the channels can be estimated by substituting the various mass fluxes into Eq. (2.36), to give Eq. (2.40):

$$x_{exit} = \frac{G_{O_2}}{G_{circ} - G_{cons} - G_{drag} + G_{O_2}} \tag{2.40}$$

This model has been used to develop flow regime maps that predicts the various flow regimes as a function of operational current density, water feed rates and flow channel configurations [59], [91], [94]. Figure 2.10 shows a typical flow regime map for the PEMWE anode channel for various flow-fields. However, the key limitation of this model, and hence the corresponding accuracy of the flow regime maps are the assumptions that G_{circ} is constant even when oxygen gas is entrained and that the flow quality changes linearly along the flow channel from zero to x_{exit}.

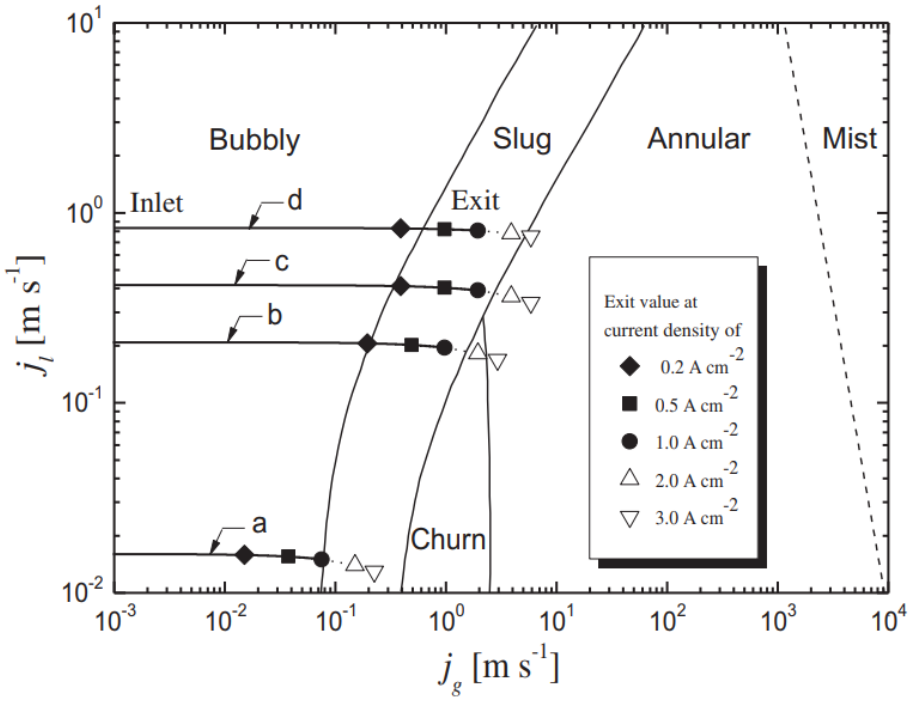

Figure 2.10. Flow regime map expressed by superficial velocity of gas and liquid showing flow characteristics for various flow-field configurations (a) parallel (b) serpentine-dual (c) serpentine-single at water feed rate of 25 ml min^{-1} and (d) serpentine-single at 50 ml min^{-1}. Adapted from Ref [91]

2.7.1.3 Flow-field Configurations and Influence on PEMWE performance

In the PEMWE, once the liquid water enters the cell, it must be distributed over the entire reaction surface area. This is typically accomplished through a flow-field, which usually has channels covering the entire area in some pattern or porous structure. Since the two-phase flow behaviour in the flow-field affects the mass transport of water to the catalyst layer and the bubbles removal, it has a direct impact on cell performance.

The most common types of flow designs that have been presented in the literature include parallel, serpentine, spot (grid) and interdigitated and are shown in Figure 2.11.

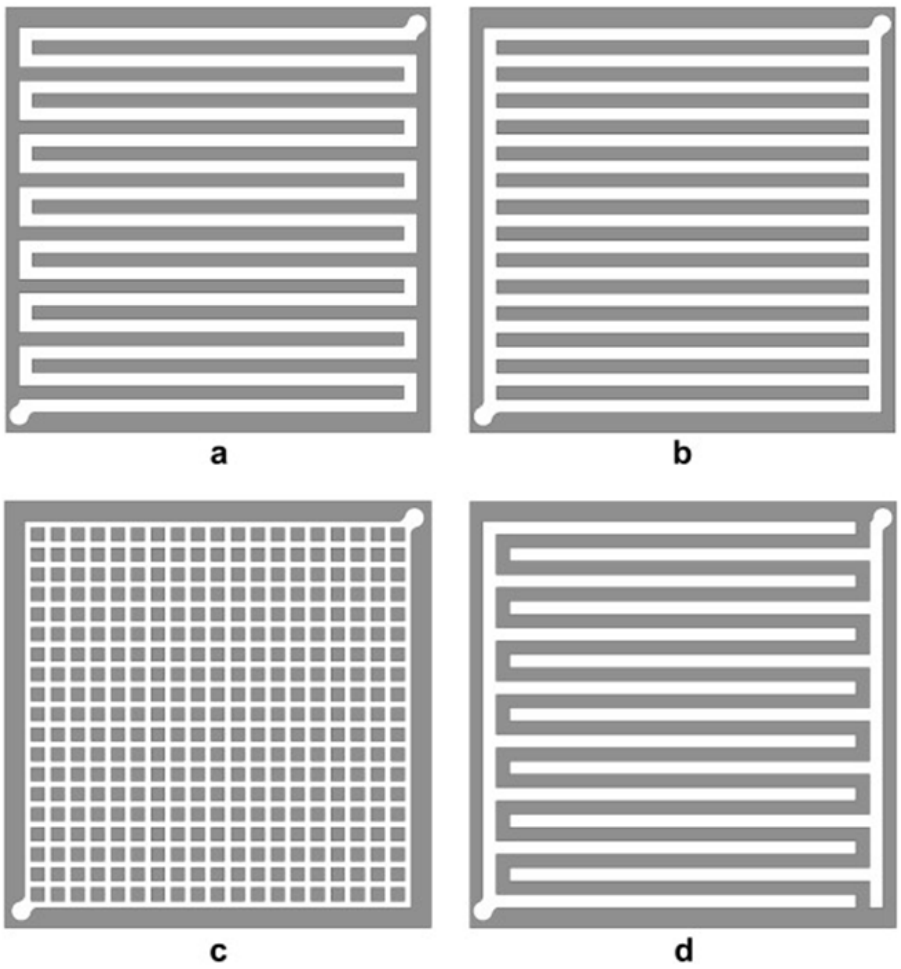

Figure 2.11. Various flow-field designs in PEMWE development (a) serpentine (b) parallel (c) spot/grid (d) interdigitated.

Ito *et al.* [91] investigated different flow-field designs and examined the effects of current density, water feed rate and cell temperature and found that mass transport limitations are more pronounced in the slug or annular regime than in the bubbly regime and that there is a strong relationship between the two-phase flow regime and performance. Dedigama *et al.* [94], [97] studied the two-phase flow characteristics as a function of current density and water feed rates using high-speed imaging in the anode flow-field of a transparent PEMWE equipped with a parallel flow-field. They also investigated the heat distribution and current density distribution across the active area of the cell. Results showed how the flow regime evolves along a channel from bubbly to slug/annular and that this is associated with an increase in local current density towards the end of a channel. Lafmejani *et*

al. [106] examined the pattern of vertical upward gas-liquid flow in a single straight channel by optical visualization in an ex-situ setup. They analysed two-phase flow phenomena in PEMWE by gas injection through a permeable wall made of titanium felt into a transparent channel of flowing water. Their results indicated that bubble coalescence occurred along the channel length and bubbly-flow, Taylor flow and annular flow regimes were observed.

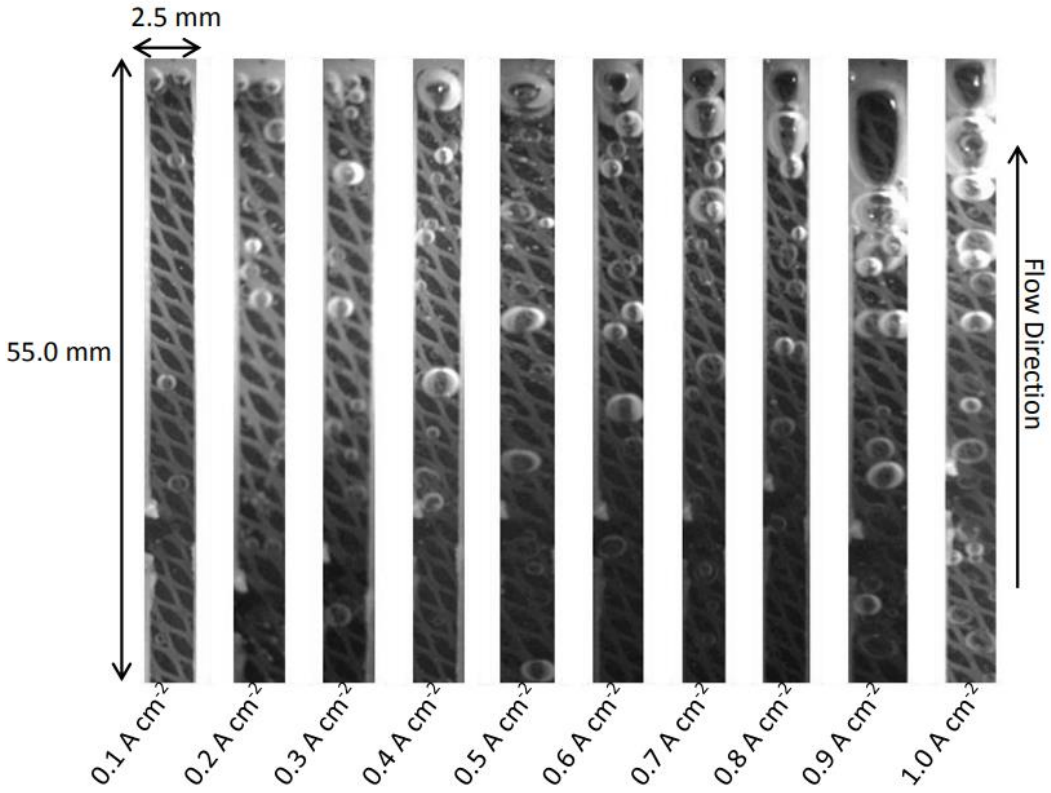

Figure 2.12. Flow regimes visible in the middle anode channel of a PEM water electrolyser operating at room temperature (20°C), atmospheric pressure (1 atm) and water feed rate of 1 ml min^{-1}. Adapted from Ref [94]

Selamet *et al.* [107] combined neutron radiography with optical imaging to examine gas evolution at the anode and cathode sides of an operational PEMWE. Using the evolution of water thickness with time, they found that gas-bubble evolution and detachment follows a cycle of periodic growth and removal of small bubbles followed by prolonged blockage by large stagnant bubbles. They also investigated the effect of operating parameters and found that water feed rate, current density and operating temperatures have a significant influence on two-phase flow phenomena in PEMWE. Hoeh *et al.* [108] used neutron imaging to quantify gas

evolution in the anode channel at various current densities and water feed rates. They found that gas void fraction in the channel decreases with increasing water feed rate and increases with increasing current density. To analyse gas evolution into the channels, Hoeh *et al.* [109] also investigated gas discharge into the anode flow channels using synchrotron X-ray radiography. Their results showed that there exist selective pathways for gas evolution from the porous transport layer and the number of such pathways increases with increase in current density.

Also, several studies have employed modelling and numerical techniques to improve understanding of two-phase flow and flow-field design in the PEM electrolyser. Nie *et al.* [55] performed three-dimensional numerical simulations and experimental measurements of fluid flow in a simplified bipolar plate of a PEM electrolysis cell. Their investigations in the bipolar plate with parallel flow channels showed that the pressure decreases from inlet to outlet in the diagonal direction. They also reported non-uniform distribution of velocity and temperature over the flow field. Tijani *et al.* [110] investigated several flow plate designs using numerical simulation to evaluate hydrodynamic properties, velocity fields and pressure gradients in different designs. Aubras *et al.* [111] developed a two-dimensional model for evaluation of heat and mass transfer at the PEM electrolyser electrodes taking into account two bubbly flow regimes. They suggested that the bubble coalescence phenomenon is associated with improved mass transfer and reduced ohmic resistance in the PEM electrolyser. Ruiz *et al.* [112] developed a mathematical and numerical framework for the investigation of the effect of flow channel configurations in a high temperature PEM electrolyser. They investigated the parallel, serpentine and multiple-serpentine flow channel configurations and suggested that the multiple-serpentine design performs better in terms of hydrogen production, temperature uniformity and pressure drop. More recently, Toghyani *et al.* [32] developed a three-dimensional numerical analysis for performance comparison of five flow field patterns evaluating performance based on molar fraction of produced hydrogen, current density, and temperature and their result revealed better distribution of temperature and current density in the serpentine flow field configuration.

Similar to the two-phase flow phenomena at the anode of a PEM electrolyser, the anode of a direct methanol fuel cell (DMFC) has simultaneous transport of liquid methanol reactant and evolution of CO_2 gas produced at the electrocatalyst surface. Thus, the produced CO_2 gas becomes entrained in the liquid methanol reactant, and a two-phase flow arises in the flow-field channels at the DMFC anode. Several studies have investigated the gas evolution and two-phase flow phenomena in DMFCs in relation to cell performance. Various flow-field designs have been explored including parallel, serpentine, interdigitated, grid, spiral and fractal flow-fields [33], [34], [35], [36], [37], [38]. These studies have reported that the serpentine flow pattern provides the best performance due to the higher velocity, which contributes to increased convective flux and leads to better mass transport at high current densities. A few studies have investigated the effect of geometric parameters such as channel width, rib width and channel dimension ratios, among others [39], [40], [41]. Several studies have also probed bubble evolution and two-phase phenomena in DMFCs, specifically using visualization techniques [38], [40], [42], [43], [44]. These studies highlight that cell performance is affected by several factors including flow-field design, channel geometry and operating parameters.

2.7.2 Porous Transport Layers in PEMWE

The porous transport layers (PTLs) in PEMWEs are permeable, electrically conductive media sandwiched between the MEA and flow-field/bipolar plate at both electrode sides to facilitate the transport of liquid and gas between the electrodes and flow channels, as well as electrical and heat conduction within the cell [88], [113]. These functions of the PTL require high liquid permeability and gas diffusivity of the pore phase, and high electrical and thermal conductivity of the solid phase.

Ideally, the PTL contributes minimally to overpotential losses in the PEMWE, such that the liquid water is fed to the electrode and the product gas is expelled from the catalytic layer through the PTL unhindered. However, the build-up of oxygen gas in the form of bubbles (gas voids) in the vicinity of the anode can reduce the available active area for reaction, and gas bubbles trapped in the pores of the PTL could hinder mass transport of liquid water to the electrode [114]. Since, the PTL plays such a key role in determining the overall performance of PEMWEs, it is

necessary to understand how its structural properties such as pore size distribution, thickness, porosity, tortuosity, gas/water permeability, and electrical conductivity influences performance.

2.7.2.1 PTL Materials and Types

Titanium is the commonly used PTL material in PEMWEs as opposed to carbon fibre-based materials (carbon paper and cloth) typically used in PEM fuel cells [115]. Carbon materials are unsuitable in PEMWE anodes due to the high anodic potential which corrodes carbon materials whereas titanium exhibits high corrosion resistance under high anodic potential and acidic conditions. Furthermore, titanium provides good thermal/electrical conductivities and excellent mechanical properties [18].

However, the surface of the titanium is oxidized to the highly-electrically resistive TiO_2 leading to increased interfacial contact resistance which adversely affects performance [116]. Therefore, Ti PTLs are often coated with precious metals to resist surface oxidation and achieve satisfactory conductance [57]. The commonly used PTLs at the anode of PEMWEs are titanium (Ti)-based materials such as sintered titanium powders, expanded sheets, felt type titanium fibre and titanium foam [56]–[60], [117].

1. **Ti felt PTL**

The Ti felt PTL has a similar structure to carbon paper commonly used in PEM fuel cells consisting of unwoven fabric made of shaved fibres of Ti metal interweaved to form a non-ordered porous material and shown in Figure 2.13(b) and (d). The Ti felt is prepared by thermal sintering of evenly distributed fine Ti fibres, and subsequent roll-pressing achieves smoothness and controls thickness. The fibre diameter is often selected to minimize surface roughness and its damaging effect on the adjacent MEA, and is normally varied between 20-100 μm [118]. Key properties of the PTL such as porosity, and pore diameter are usually controlled during fabrication by adjusting the fibre diameter and the fibre loading range (usually about 0.5–0.8). For practical purpose, the pore size is often varied between 20 and 200 μm [58]. The key advantage of the Ti felt as PTL is its ability to support mass transport in both the in-plane and through-plane directions, enabled by its

fibre orientation. Thus, various researchers have investigated the optimization of its structure in relation to performance in the PEMWE, including effect of porosity, pore diameter, thickness, and two-phase flow regime [56], [58], [59], [113].

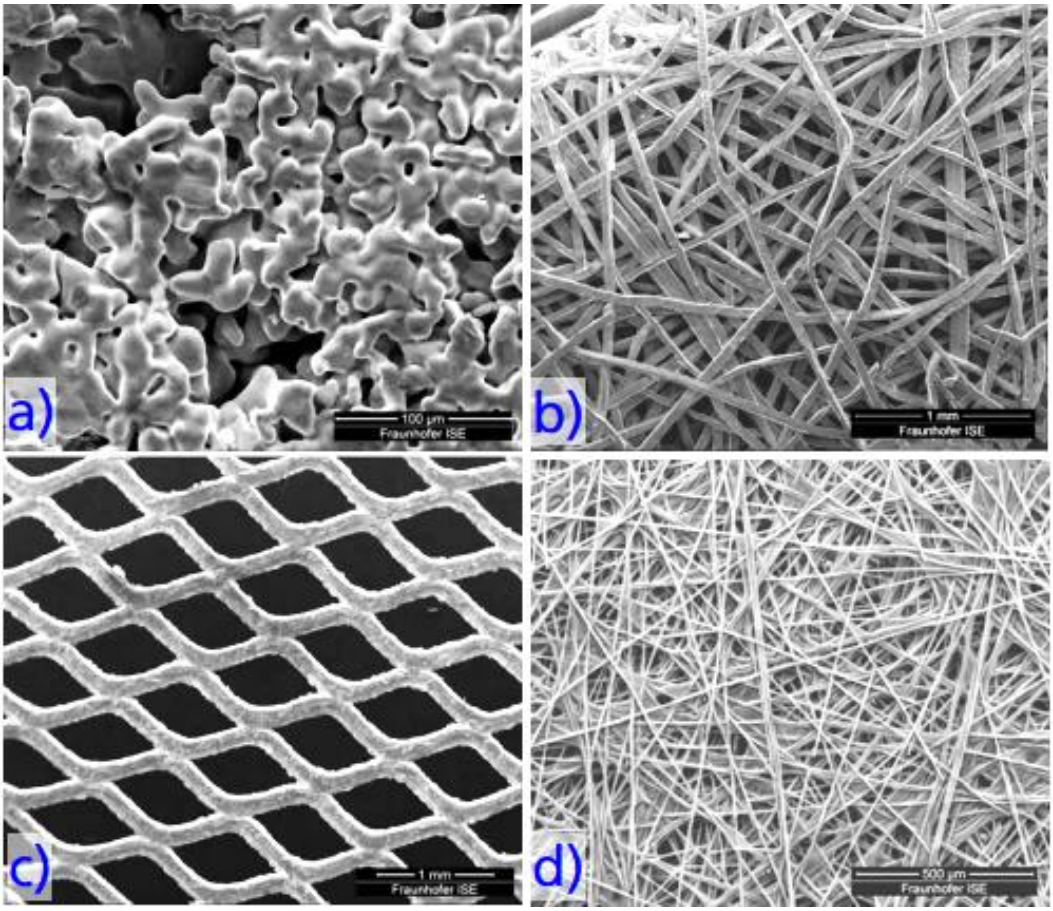

Figure 2.13. Micrographs of various PTL types (a) sintered Ti powder, (b) Ti felt, (c) expanded Ti mesh, (d) carbon fibre paper. Reproduced from Ref [119].

2. Screen Mesh PTL

The screen mesh is a fine screen Ti PTL used in a number of lab-scale electrolyser studies [113], [120] and is shown in Figure 2.13(c). The screen mesh PTL are the cheapest PTL type; however, its main limitation is the reduced electrolysis performance compared with the sintered structures or felts [121]. Also, the screen mesh generally has a large fibre diameter typically larger than 100 µm and a large pore diameter typically larger than 150 µm which makes for a large uneven surface, which predisposes the PTL to "sinking" into the MEA during assembling compression and thus damages the catalyst layer [18].

3. Sintered Powder PTL

This PTL type is the most commonly used and is fabricated by thermal sintering of spherical-shaped Ti powder. Figure 2.13(a) shows micrographs of a typical sintered Ti powder PTL. The structural properties of the solid sinter such as porosity, rigidity, pore size, etc. can be arbitrarily adjusted by controlling the sintering conditions such as temperature, pressure and powder size [122], [123]. Under controlled sintering conditions, the porosity can be set at a range usually between 30-50% and the pore size within the range of 10 – 60 μm [18]. The PTL thickness is usually in the range 1.0-1.5 mm and the surface can be smoothened by polishing. The high rigidity of the sintered Ti powder PTL is a key advantage as it provides excellent structural support to the MEA at pressures surpassing 100 bars. This PTL type is most common and has been used extensively industrially and in lab-scale applications [28], [57], [124].

2.7.2.2 PTL Microstructural Properties

Various microstructural properties of the PTL affect the PEMWE performance including particle size and porosity, pore size distribution, tortuosity, and water/gas permeability etc. This section sheds light on the structural investigation of the PTL, attempted to date, to improve the performance of the PEMWE.

1. Particle size and Porosity

Several studies have investigated the effect of porosity and particle/fibre size for both felt and sintered powder PTLs. Hwang *et al.* [58] employed titanium felt PTL to examine the effect of PTL porosity and fibre size on the performance of a unitized reversible fuel cell (a device which combines the functionality of fuel cell and electrolyser in a single device) under electrolysis mode. They demonstrated that cell performance was degraded at high current density when fibre size increased from 20 to 80 μm, attributed to generation of larger bubbles in the larger pore samples, which impact flow regimes in the flow-field channels and consequently hinder water supply to the electrode surface. Also, they found that for the fibre diameter of 20 μm, the cell performance was not noticeably affected by an increase in porosity from 50 to 75%. Similar studies by Ito *et al.* [56], [59] investigated porosity and fibre diameter of felt type PTLs and reported that contact resistance

increased as the fibre diameter increased due to increased surface roughness. They pointed out that for porosity greater than 50%, further increase in porosity had no significant effect on performance. For sintered powder PTLs, Grigoriev *et al.* [57] investigated the effect of powder size and porosity on the mass transport and ohmic losses and demonstrated that a powder diameter of 50 to 75 μm with a porosity range of 30 to 50% yielded optimal performance. Contrary to the findings by Grigoriev *et al.* [57] and Ito *et al.* [56], [59], Han *et al.* [125] reported that higher porosities can be beneficial for liquid-water saturation along the PTL thickness and therefore lead to improved performance. The liquid-water saturation was examined using two-phase transport model, however their model fail to account for the effect of porosity on electrical conductivity.

2. Mean Pore Diameter (MPD)

The mean pore diameter of the PTL is a key microstructural characteristic that has been demonstrated to influence PTL performance. Grigoriev *et al.* [57] experimentally investigated the effect of pore diameter in sintered powder PTLs and suggested that an MPD of 12-13 μm is optimal for sintered powder PTLs, proposed as a compromise between capillary effects, which manifest at pore sizes below 10 μm, and parasitic ohmic losses associated with large pore sizes. Similar results for felt-type PTLs were reported by Ito *et al.* [59] as they also observed that the electrolyser performance deteriorated with increasing MPD when the MPD was larger than 10 μm. In another study, Ito *et al.* [56], suggested that the oxygen bubbles produced at the anode may block the PTL when the MPD is less than 50 μm. Taken together, these studies suggest that there is an optimal range of PTL pore diameter to minimize mass transport losses; small enough to prevent large gas slugs in the PTL and large enough to minimize capillary effects. Also, that electrolysis performance under atmospheric pressure improves with decreasing pore diameter, regardless of the PTL type. However, contrary to the results by Grigoriev *et al.* [57] and Ito *et al.* [56], [59], Han *et al.* [125] studied the effect of PTL pore sizes between 35 μm and 95 μm in and reported that, the liquid saturation in the PTL increases with increase in pore size and concluded that larger pores might enhance the PEMWE performance.

3. Permeability

Water and gas permeability characteristics of the PTL have an important influence on mass transport and overall performance in the PEMWE. Zielke *et al.* [126] examined the PTL transport properties such as permeability, thermal conductivity, electrical conductivity using micro-computed tomography and a commercial software package, *GeoDict*. They reported an inverse relationship between the PTL porosity and thermal conductivity and also between the in-plane electrical conductivity and water permeability. This means that high porosity or high permeability leads to enhanced water delivery to the electrocatalyst layer, but at the cost of increased electrical resistance, and these relationships were found to be consistent for the various types of PTLs.

2.7.2.3 Visualization Studies of Transport Behaviour in the PTL

A few attempts have focused on understanding the liquid and gas transport behaviours in PEMWE PTLs. Hoeh *et al.* [109] employed *in-situ* synchrotron X-ray radiography to visualize hydrogen bubble growth behaviour at the flow channel/PTL interface in PEMWEs. They found that the gas transport in the PTL occurs through selective pathways and the number of gas bubble discharge sites in the PTL increased as the current density increased. They showed that bubbles are swept away by the flowing water after reaching a critical size. After bubble departure, a new bubble nucleates and grows from the same position (and gas pathway). Arbabi *et al.* [127] performed an *ex-situ* visualization study using a microfluidic lab-on-chip with a 2D pore network to capture structural information of three PTLs; namely, felt, sintered powder, and foam. A representative 2D pore network was created for each material, and the bubble behaviours inside the three materials were compared. They showed that the oxygen gas flow regime in the PTL is likely to be capillary-dominated and that this tool can be used to compare the impact of geometrical properties on the oxygen flow behaviour in the PTL. These studies have shown important gas bubble behaviour, however, there is yet tremendous opportunity to gain deeper understanding of gas evolution in the PTL using various visualization approaches.

2.8 Conclusion

Various aspects of PEMWE development have attracted increased interest, due to its potential for hydrogen production and energy storage. The literature review presented in this chapter has shown that operation at high current density is desired, and in this respect, understanding gas-bubble evolution and two-phase flow in the PTL and flow field channels is crucial to improved performance. This review has also presented the existing understanding of the mass transport phenomena and the influence of microstructural and design characteristics of the PTL and flow-field on performance. Current understanding is very limited and it is therefore important to gain more comprehensive understanding of the mass transport phenomena in the PEMWE especially at elevated current density.

In this research, simultaneous optical visualization and electrochemical measurement is performed to provide crucial insight into bubble evolution and the influence of flow regime on performance. Furthermore, the influence of microstructural properties of the PTL was investigated by combining electrochemical impedance spectroscopy and X-ray tomographic technique to understand structure-performance relationships of the PEM electrolyser PTLs.

The next chapter presents the experimental procedures and techniques used in this research. The development (design and fabrication) of the two different PEMWE cells used in this study, as well as the various *operando* and *ex-situ* techniques and electrochemical methods employed is extensively discussed.

Chapter 3

Experimental Methods and Electrolyser Cell Development

As discussed in Chapter 2, understanding the influence of the PTL microstructural properties and flow-field designs on mass transport and, ultimately, performance is important for PEMWE development. This chapter presents the experimental methods and techniques used for cell fabrication and characterization in this research. The theory behind operando and *ex-situ* techniques used to interrogate mass transport behaviour in the flow-field and PTLs are introduced and finally, the implementation procedures of the various techniques are presented.

3.1 Diagnostic Techniques: Theory and Applications

Various diagnostics tools are used to understand the behaviour of processes and quantification of various losses in electrochemical systems. To date, a wide range of experimental diagnostics has been developed to obtain fundamental understanding of the various dynamics in electrochemical systems [128]. This section focuses on the diagnostic techniques used in this research; outlining the principle of operation, experimental implementation, and data processing.

The diagnostic techniques includes (i) electrochemical techniques such as polarisation curve, galvanostatic measurements and electrochemical impedance spectroscopy (EIS) (ii) Physical techniques which include visualization techniques

such as high-speed optical imaging and X-ray micro-computed tomography. These tools help to optimize cell design and overall performance.

3.1.1 Polarization Curve

Polarization means that the potential of the electrode surface shifts away from its equilibrium value, leading to an electrochemical reaction. Therefore, the polarization curve records the change in cell potential with current density under a set of constant operating conditions [129]. It yields information on the various performance losses in the cell under the prevailing operating conditions and has been used extensively in PEMWE research [33], [57], [58], [130], [131]. Polarization curve measurements allow parameters such as the effects of the water feed rate, water circulation, temperature and pressure to be characterized and compared.

The ideal polarization curve has three distinct regions, and a typical PEMWE polarization curve is shown in Figure 3.1. The first region is observed at low current density and is called region of *activation polarization*. It is characterized by a sharp increase in cell potential due to the charge transfer resistances associated with initiation of the electrochemical reaction, particularly the sluggish kinetics of the oxygen evolution reaction [132]. The second region is observed at intermediate current density and is called the region of *ohmic polarization*, characterized by a linear increase of cell potential with current density due to ohmic resistance resulting from resistance to the flow of ions in the electrolyte and resistance to the flow of electrons through the electrode, porous transport layer and bipolar plates [133]. The third region is observed at high current densities and is called the region of *concentration polarization*, characterized by a sharp increase in cell potential due to mass transport limitations which includes the formation of resistive gaseous films at the interface between the catalytic layers and the PTL and the two- phase water/gas flow through the PTL and the flow channels of the flow-field plate [18].

All three overpotentials (reaction activation, ohmic and mass transport limitation) exist at all current densities in a polarized cell, however, the extent to which one overpotential dominates the cell behaviour varies with current density and defines the shape of the polarization curve in that region. A good working electrolyser is

expected to display a polarization curve with low cell potential (voltage) at high current density.

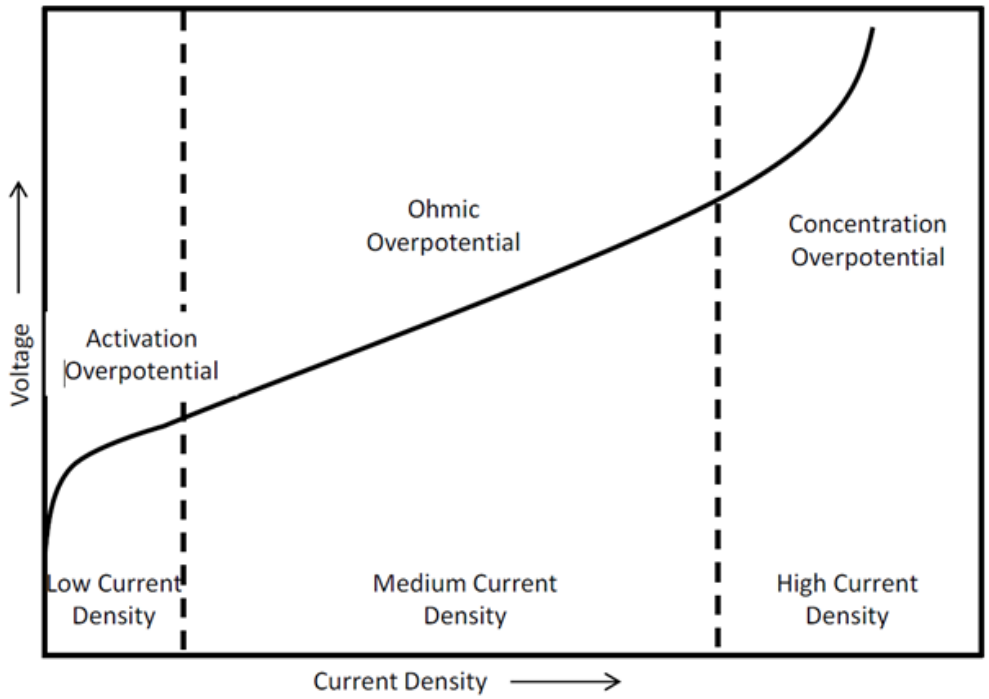

Figure 3.1. Typical polarization curve of a PEMWE showing the three main overpotential regions.

The polarization curves provide information on the performance of the cell under specific operating conditions; but do not produce much information about the performance of individual components within the cell. Polarization curve also fail to differentiate different mechanisms and is incapable of resolving time-dependent processes in the cell. For these reasons, other electrochemical methods, mainly electrochemical impedance spectroscopy (EIS) are often used complementarily.

3.1.2 Electrochemical Impedance Spectroscopy

Electrochemical impedance spectroscopy (EIS) is a powerful, dynamic, and non-destructive diagnostic method widely applied in electrochemical systems [94], [129]. EIS analyses the linear response of a system by applying a small sinusoidal AC voltage or current perturbation/signal (of known amplitude and frequency) to the cell, and the amplitude and phase of the resulting current or voltage signal are measured as a function of frequency. This is repeated over a wide range of frequencies (i.e. large frequency spectrum, hence the name "spectroscopy"). The

frequency of the AC perturbation is usually swept over a range from 1 MHz to 1 mHz [134]. The impedance is the ratio of the input AC perturbation and the output AC response and is evaluated as a function of frequency. Characteristic frequency ranges can often be related to particular electrochemical processes; thus EIS enables separate evaluation of the various resistances caused by the electrochemical reactions.

The electrochemical impedance is usually measured using a small excitation signal to preserve pseudo-linearity of the cell. In a linear (or pseudo-linear system) the response signal is a sinusoid at the same frequency as the perturbation signal but shifted in phase.

3.1.3 Theory of AC Impedance

A sinusoidal current signal of amplitude I_{AC} and frequency ω can be defined in Eq. (3.1) as:

$$I(\omega) = I_{AC} \sin(\omega t) \tag{3.1}$$

Where t is time and ω is the radial frequency, related to the frequency f (expressed in hertz) by $\omega = 2\pi f$. The output AC voltage signal from the electrochemical cell, shifted in phase and having different amplitude, is expressed in Eq. (3.2) as:

$$V(\omega) = V_{AC} \sin[(\omega t) + \theta] \tag{3.2}$$

Where V_{AC} is the amplitude of the output voltage signal and θ is the phase angle defined as the difference in the phase of the sinusoidal voltage and current signals. For the AC perturbation, the resistance of the electrochemical system which is not purely resistive will be a function of frequency of oscillation of the input signal. The impedance is therefore a complex value, which means it can take on both real and imaginary components. The complex impedance can be written in an Ohm's law form and described in Eq. (3.3) as:

$$Z(i\omega) = \frac{V(i\omega)}{I(i\omega)} \tag{3.3}$$

Where i is the imaginary number $i = \sqrt{-1}$ that allows the description of the out-of-phase component of the impedance making the imaginary component of the impedance a real measurable quantity.

Eq. (3.3) can be written in complex notation described in Eq. (3.4) as:

$$Z = Z' + Z'' \tag{3.4}$$

Where Z' is the real (in-phase) component of the impedance defined as:

$$Z' = Re(Z) = |Z| \cos\theta \tag{3.5}$$

And Z'' is the imaginary (out-of-phase) component of the impedance defined as:

$$Z'' = Im(Z) = |Z| \sin\theta \tag{3.6}$$

The magnitude $|Z|$ of the combined real and imaginary components can be calculated as:

$$|Z| = \sqrt{(Z')^2 + (Z'')^2} \tag{3.7}$$

And

$$\theta = \tan^{-1}\left(\frac{Z''}{Z'}\right) \tag{3.8}$$

The complex plane of the complex number Z is presented in Figure 3.2. As can be seen, the horizontal and vertical axes are called the real and imaginary axes respectively.

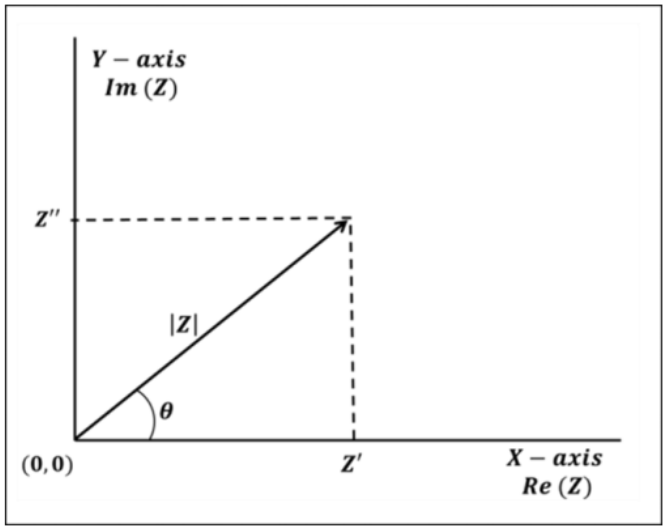

Figure 3.2. A plot of the real component of impedance versus the imaginary part describing the overall impedance Z as a plot of planar vectors using polar coordinates.

3.1.3.1 Presentation of Impedance Data

The data collected from EIS is usually presented in a Nyquist or Bode plot which involves various combinations of the parameters used to describe impedance at a given frequency namely: the real (Z') and imaginary (Z'') impedance, the phase angle (θ) and the impedance magnitude/amplitude ($|Z|$) [135].

Presented as a Complex plane or Nyquist plot (Figure 3.3(a)), the imaginary part (Z'') of the complex impedance (mostly presented with a negative sign) is plotted against the real part (Z') at each frequency. In this representation, the frequency is implicit; but the individual overpotentials and time constants are easily observed. The real part of the impedance is associated with pure resistance and the imaginary part is associated with capacitance and inductance. Figure 3.3(a) shows typical impedance spectra for PEMWE in Nyquist form with two arcs, where the frequency increases from the right to the left. The high frequency arc reflects the combination of the effective charge transfer resistance and the ohmic resistance. The low frequency arc is often associated with impedance due to mass transport limitations.

The other form of impedance data representation is the Bode plot. Here, the magnitude of impedance (amplitude) and phase of the impedance is plotted as a

function of frequency ($\log|Z|$ versus $\log\omega$ and θ versus $\log\omega$) as shown in Figure 3.3(b) and (c). For instance, the local maximum values in the Bode phase plot show the characteristic frequencies which are proportional to the inverse of the time constants of the processes [136].

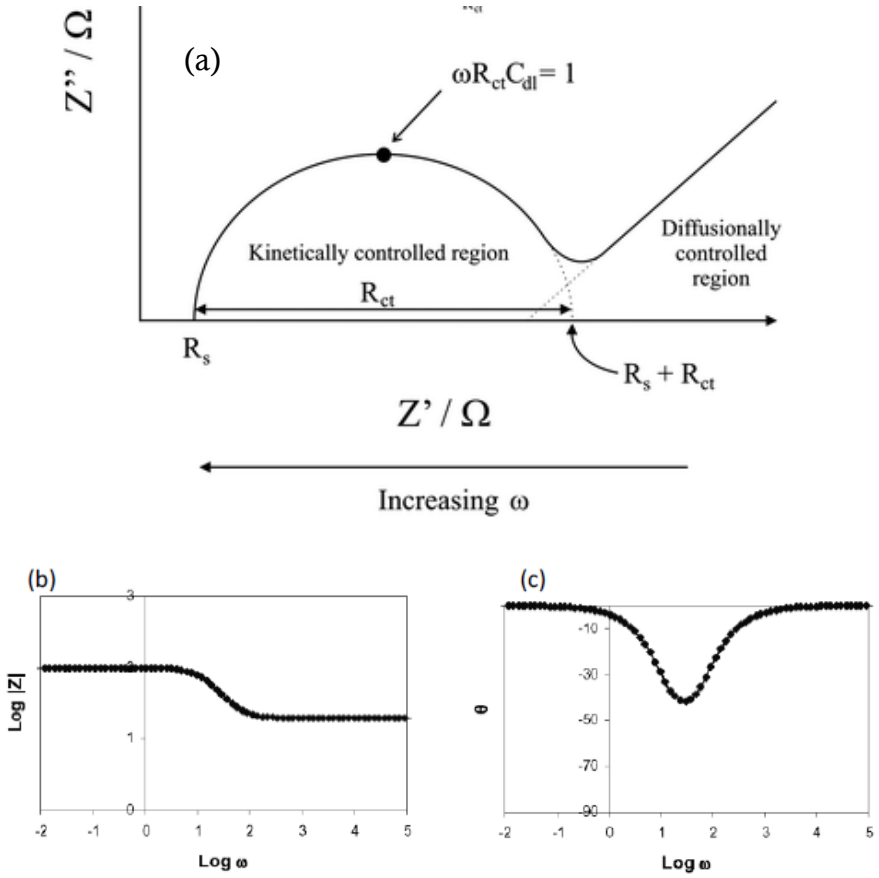

Figure 3.3. (a) Typical Nyquist impedance plot. (b) and (c) Bode plots

3.1.3.2 Equivalent circuit fitting

Equivalent circuit fittings are often used to analyse experimental EIS data to extract useful parameters and identify underlying process. The analysis consists of fitting a measured impedance diagram with combination of ideal (resistor, capacitor, and inductor) and non-ideal (constant phase element or CPE, Warburg element, etc.) electrical elements in series and/or in parallel.

The ideal circuit elements are resistors, capacitors and inductors. The resistor has no imaginary impedance component and is frequency-independent. Hence, a resistor is represented in a Nyquist plot as a single point on the real impedance axis. The impedance of a resistor is given in Eq. (3.9) where R is the resistance.

$$Z_R = R \tag{3.9}$$

A capacitor has only an imaginary component and the voltage output through the capacitor has a -90° phase shift with respect to the current input. The impedance of a capacitor is given in Eq. (3.10), which shows that the capacitive contribution is small at high frequencies and the impedance increases with frequency.

$$Z_C = \frac{1}{j\omega C} \tag{3.10}$$

An inductor has only an imaginary component similar to the capacitor. However, the voltage output in the inductor has a 90° phase shift with respect to the current input. As represented in Eq. (3.11), the inductor has the opposite impedance behaviour to the capacitor where its contribution is highest at high frequency and decreases with decreasing frequency.

$$Z_L = j\omega L \tag{3.11}$$

Real electrochemical systems, where complex reactions take place, rarely behave like ideal circuit elements. Therefore, their impedance behaviour is often modelled using non-ideal elements such as the constant phase element (CPE) which can be considered to be a leaky capacitor. Its name implies that the phase angle of the process described is independent of the frequency. The impedance of the CPE is given in Eq. (3.12) where the exponent n can vary between -1 and 1. The possible cases are when:

- n = -1, the CPE behaves as an inductor.
- n = 1, the CPE behaves as a pure capacitor.
- n = 0, the CPE behaves as a resistor
- n = 0.5, the CPE behaves as a Warburg element.

$$Z_{CPE} = \frac{1}{Q(j\omega)^n} \tag{3.12}$$

Any other intermediate value for n could be explained by the presence of inhomogeneities in the material tested. However, non-characteristic values make

the interpretation of the physical processes happening in the system more challenging.

3.1.4 X-ray Computed Tomography

X-ray CT is a non-destructive 3D imaging and analysis technique for investigation of internal structure of materials/samples at spatial resolutions down to a few hundred nanometres and has been used in numerous applications in fields such as food science [137], material science [138], earth science [139], and biology [140]. It is finding increasing application in the investigation of internal structure of electrochemical materials to establish structure-performance relationships in electrochemical systems [141], [142].

3.1.4.1 X-ray CT Background

X-ray CT originated from Computerized Axial Tomography (CAT or CT) scans that have been used in medical imaging for over 40 years [137]. CAT scanning was an extension of projection radiography, a technique capable of producing 2D images of samples internal structure. The main limitation of radiography is that features can only be located within the 2D plane of the image, resulting in information loss and image misinterpretation [143]. X-ray CT overcomes this drawback by combining information from a series of 2D absorption images obtained as the sample is rotated around an axis. Mathematical principles of tomography are then used to reconstruct the series of 2D radiographs into 3D images where each voxel (volume element or 3D pixel) represents the X-ray absorption at that point [137].

Thus, X-ray CT imaging combines X-ray absorption physics relevant for the 2D projection images and tomographic reconstruction mathematics relevant to the generation of a 3D volume from a series of 2D images.

3.1.4.2 Operation Principle and Image Acquisition

The X-ray CT assesses the internal structure of a sample by targeting the sample with a monochromatic X-ray beam and a X-ray detector placed behind the sample to obtain stuctural information. The principle is based on image contrast produced by differences in X-ray attenuation (absorption and scattering) arising primarily

from the differences in density and composition within the sample. Thus, the X-ray transmission level through the sample is determined by the sample mass as well as its absorption coefficient. X-rays are passed through the sample at various orientations on the rotation stage, resulting in an image which displays differences in density at numerous points in a 2D slice [144]. The total angle of rotation depends on the geometry of the beam and the sample but is typically 180° for a parallel beam (e.g. synchrotron) or 360° for cone beam (e.g. laboratory system). Figure 3.4 illustrates the principle of image acquisition of the X-ray CT system.

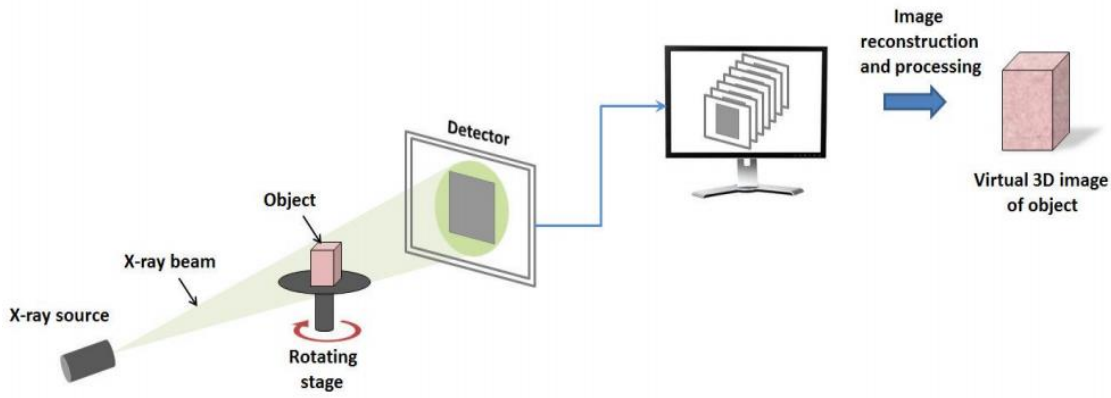

Figure 3.4. Schematic illustration of the measurement principle of X-ray computed tomography. Adapted from Ref. [145].

During the image acquisition, the collimated X-ray beam is directed towards the sample rotated on a translational stage while the detector collects the remnant attenuated radiation and transferred to the computer for visualization of the 2D image. Operating conditions such as beam energy, beam current, exposure time and sample-to-detector distance are optimized prior to scanning to obtain optimized radiographs [137].

Data from the numerous X-ray radiographs obtained are processed and reconstructed into 3D volume from which tomograms (3D representations of the sample's internal structure and composition) can be extracted. The image is comprised of volume elements (voxels) that represent the X-ray absorption at a specific point. The images can be presented as virtual slices through the sample at various depths and directions or the sample can be viewed as a whole [137].

Dedicated software packages enable manipulation and analysis of the data as well as reconstructions of cross-sections along all orientations. Reconstruction algorithms are classified into direct and iterative approaches [146]. Direct methods are often used, mainly the Filtered Back Projection (FBP) and Direct Fourier Inversion (DFI) methods.

3.1.4.3 Image Processing

Image processing and analysis is required to visualise CT data and extract required information such as porosity, tortuosity, pore size distribution etc. from the image. After image acquisition and initial reconstruction, subsequent image processing is used to enhance greyscale image quality and extract regions of interest within the entire 3D dataset to reduce computational requirement.

During image processing, the images are initially smoothed using filters to reduce random noise or remove unwanted artefacts in the greyscale image datasets and also ease segmentation. Common digital filters used are the Gaussian, median and non-local means filter. This step is followed by segmentation where the grey scale slices are transformed into a binary layout consisting of solid and void. Segmentation is usually done using thresholding techniques, i.e (1) selecting a global threshold that is relevant to all the voxels; (2) locally adaptive thresholds; (3) region-growing techniques; and (4) clustering by iterative techniques. Voxels containing grey values lower or higher than this threshold value are regarded as background or sample material, respectively. It is essential to perform noise-reduction and suppress artefacts by filtering, smoothening and applying beam hardening corrections to eliminate errors and unwanted information before analysis. Figure 3.5 illustrates an overview of the image data processing and analysis procedure used in this study.

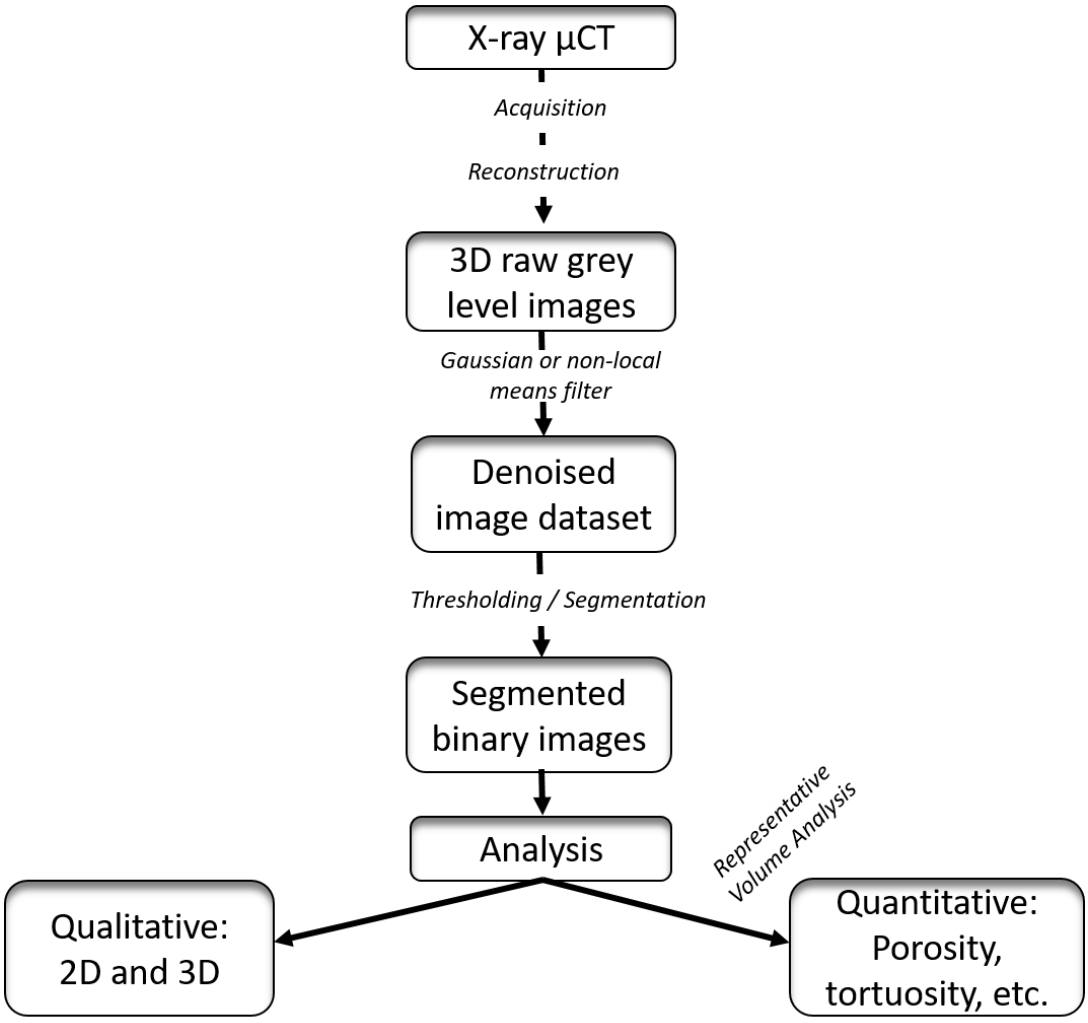

Figure 3.5. Schematic illustration of the image processing and analysis procedure used in this study.

3.1.4.4 Microstructural Quantification

After segmentation of the features of interest, microstructural quantification is performed to extract relevant structural parameters. In this work the key structural parameters of interest include porosity, pore size distribution, tortuosity, and porosity distribution. These parameters play a crucial role in understanding the relationship between the PTL microstructure and performance of the PEMWE cell. The determination of the parameters is discussed as follows:

1. **Porosity**

The porosity of a material is defined as the ratio of void volume to apparent geometric volume. Therefore, for a 3D reconstruction binarized into solid and pore

phase, porosity is the ratio of the number of voxels representing the pore phase volume to the total number of voxels in the entire 3D volume. This was implemented in this study using the Avizo image processing software package.

2. Pore size distribution

The continuous PSD method developed by Munch and Holzer [147] is implemented for the determination of pore size distribution in this work. The principle is based on expanding spheres from points along calculated centroid paths. In this method, the segmented phase is transformed into a distance map. The volume fraction of the pore phase that can be occupied by a sphere of a specific radius without crossing the pore boundary, is then measured. By plotting the radii versus the corresponding filled volumes, a cumulative continuous PSD curve is obtained. The full algorithm for the continuous PSD determination is presented in Ref [147] and the algorithm is provided for use as an open-source plugin for the Fiji ImageJ software package.

3. Tortuosity

Tortuosity describes the effect of convoluted transport pathways and variations of the pore path lengths in a material. It is considered an important feature of microstructure which may dominate the transport properties. In this thesis, the image-based quantification of tortuosity factor was performed using *Taufactor*, developed by Cooper [148], and implemented in MATLAB. It works by simulating the steady-state diffusive flow through the pore network of a segmented volume. The simulated flow rate through the pore network is compared to the calculated flow rate for a fully porous control volume with the same outer dimensions.

3.1.5 High-Speed camera Optical Imaging and Visualization

Optical imaging and visualization is an effective technique for both quantitative and qualitative investigation of dynamic behaviour of flow in electrochemical systems [89], [97], [149], [150]. The direct optical visualization has a number of advantages, mainly: ease of implementation and a high temporal and spatial resolution to obtain *in situ* fluid dynamics information.

A high-speed digital camera is used at high frame rates to record visualization results of single and two-phase flow in flow channels which are subsequently analysed in slow-motion video or as sequences of thousands of still pictures. A spot lamp is often used for illumination in order to capture clear images of the mass transport phenomena. This technique often requires that a transparent cell is designed to allow optical access to the flow channels of the cell [94], [107].

This technique has been used in a number of electrolysis studies to probe various aspects of two-phase flow during electrolytic gas evolution including measurement of bubble population [151], two-phase flow regimes [152]–[154], bubble size, bubble velocity and gas volume fraction [94], [97][99], [155] and is a key technique for mass transport investigation in this work.

3.1.6 Design of Experiments

The design of experiment (DoE) is a sophisticated statistical approach for analysing the combined effect of various input parameters (called factors) on a target parameter (called the response). The DoE methodology was first used by R.A Fisher in 1925 and many other scientists have contributed to its development over the last century, among them: F. Yates, R.C. Bose, G.E.P Box and more recently Taguchi [156], [157].

3.1.6.1 The DoE Approach

The DoE approach differs, in some respects, from the classical approach of experimental investigation that has been used for centuries by scientists. The classical experimentation approach involves holding all factors constant and varying just one factor, whose effect on the response is then studied. This approach is expected to provide important information on the sole effect of this one parameter on the response and is therefore called the 'one factor at a time' (OFAT) method. However, this method is time-consuming and, more importantly, ignores the interactions among the factors which can lead to inaccurate or misleading experimental results and deductions. DoE, on the other hand, systematically considers all factors simultaneously, and is increasingly considered a more effective approach [157], [158].

The distinctive feature of the DoE is its ability to, given an appropriate selection of design and factors, offer insight into the dependencies between variable factors and performance characteristics. This is important to determine the significant factors affecting the system/process under study and the combined effect of two or more factors on the response[157].

The input variables for the system/experiment are called *factors, k* and the measurands of the experiment, which characterizes the system performance, are called *responses*. Once the k input factors have been chosen, it is necessary to determine their range of variation (the experimental domain). If the experiments are performed only at lower bound and an upper bound of their possible ranges, it means only two *levels* of the factor are considered, and therefore 2^k experiments are required. These levels are spaced such that the difference in the response can be detected, but the levels are not outside the practical working range. The use of only two levels in the DoE implies that the analysis is based on an assumption of linear and monotonic change in the response variable. Each combination of the high/low levels for the various factors is called a *treatment* and the number of tests for each treatment is called the *replicates*, on which an analysis of variance (ANOVA) can be performed.

Selection of the satisfactory experimental design is the first step in the use of the DoE methodology. Afterwards, an adequate empirical model is selected, the influential process factors are evaluated through the ANOVA that estimates their statistical significance and the parameters of the selected model are determined using linear regression method.

Once the factors and levels are determined they are often presented in a table called a "design matrix" which systematically varies the levels of each of the factors to obtain maximum information about the response variable in the minimum number of experiments.

3.2 PEMWE Cell Fabrication

3.2.1 Optical Square cell

An optical square cell was designed and fabricated with the aid of CAD/CAM software (Rhino 4.0) and a CNC machine (Roland MDX 40) for high-speed imaging of oxygen evolution and two-phase flow in the anode flow channel of the PEMWE and is shown schematically in Figure 3.6. It consist of two endplates made from 20 mm-thick transparent polymethyl methacrylate (PMMA) material to allow optical access for gas-bubble and two-phase flow characterization. Both flow-field plates (at the anode and cathode) which also serve as the flow distributor are machined from a 1.6 mm-thick printed circuit board (PCB) material, which consists of an FR4 board clad with a 35 μm-thick copper layer. The copper layer was electroplated with a 12 μm-thick nickel layer and a 5 μm-thick gold layer to provide good conductivity and corrosion resistance. At the cathode side, a single serpentine flow-field with 1.76 mm channel width and rib width and 1.6 mm depth was fabricated.

Two flow-fields were designed for testing at the anode: a single serpentine flow-field (SSFF), a parallel flow-field (PFF). The SSFF consisted of a single meandering flow channel having nine linked vertical segments (each 30 mm long) and eight horizontal segments (each 1.76 mm long), whereas the PFF comprised nine parallel straight channels, each 30 mm long. Both flow-field designs have channel depth of 1.6 mm and a channel and rib width of 1.76 mm to maintain the same open ratio (ratio of channel area to MEA area) of 55.7% and provide a basis for comparison. To maintain compression and prevent leakage, transparent PVC gaskets of thickness 0.19 mm were placed between the flow-field plates and the end-plates. Titanium sinter having thickness 0.35 mm was used as the anode PTL and a 0.19 mm-thick unteflonated carbon paper TGP-H-060 (Toray, Inc.) was used as the cathode PTL. The MEA used was supplied by ITM Power, UK and has an active area of 3.0 × 3.0 cm^2. It consists of a Nafion 115 membrane and two electrodes with the anode composed of iridium / ruthenium oxide at a loading of 3 mg cm^{-2} and the cathode composed of platinum black at a loading of 0.6 mg cm^{-2}. The dry MEA supplied was activated by: (i) boiling in deionized water for 18 h at 60°C; (ii)

rinsing in DI water for 3 h; and (iii) in-situ activation by operating in a cell at current density of 0.1 A cm^{-2} for a period of 18 h.

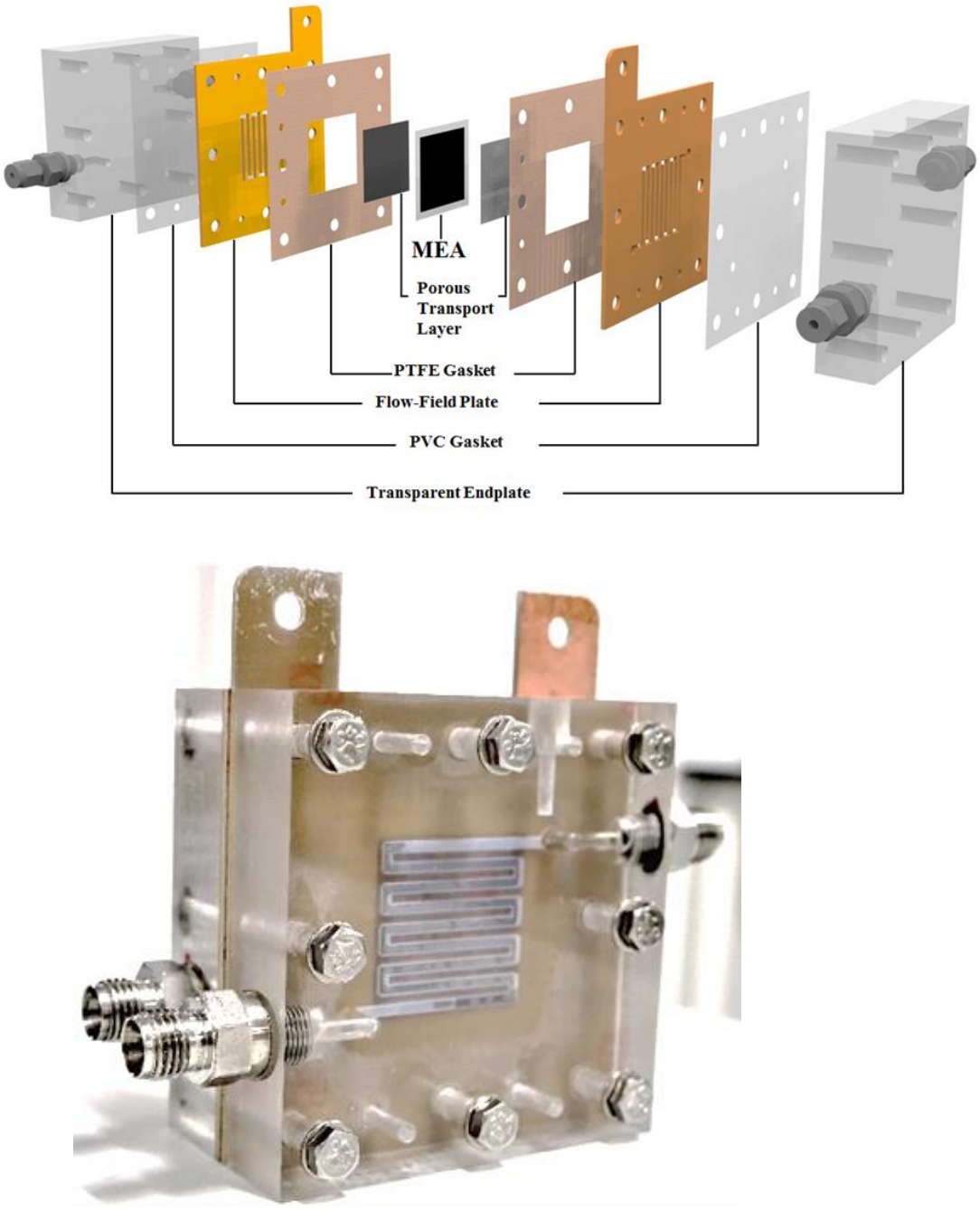

Figure 3.6. (a) In-house fabricated transparent PEMWE: (b) photograph of the assembled optical cell.

3.2.2 Single Channel Cell

A single-channel cell was designed and fabricated in-house for the investigation of influence of channel depth on two-phase flow evolution and performance presented in Chapter 5. The PEMWE cell is shown schematically in Figure 3.7. It consists of two endplates made from 20 mm-thick transparent polymethyl methacrylate (PMMA) material to allow optical access. Both the cathode and anode flow-field plates were machined from a 3.0 mm-thick titanium plate. The flow-field has a channel length of 90 mm and channel width of 5 mm. The cathode flow-field has a 3 mm depth and the anode channel depth was varied between 3.0 mm and 8.0 mm. To maintain compression and prevent leakage, transparent PVC gaskets of thickness 0.19 mm were placed between the flow-field plates and the end-plates. Porous titanium sinter having thickness 1.2 mm was used as both anode and cathode PTL.

The MEA used was supplied by ITM Power, UK and has an active area of 13.5 cm^2 (1.5 cm × 9.0 cm). The assembly consists of a Nafion® 117 membrane and two electrodes with the anode composed of iridium ruthenium oxide at a powder loading of 3.0 mg cm^{-2} and the cathode composed of platinum black at a powder loading of 0.6 mg cm^{-2}. The dry MEA supplied was activated by: (i) boiling in deionized water for 18 h at 60°C; (ii) rinsing in DI water for 3 h; and (iii) in-situ activation by operating in a cell at current density of 0.1 A cm^{-2} for a period of 18 h.

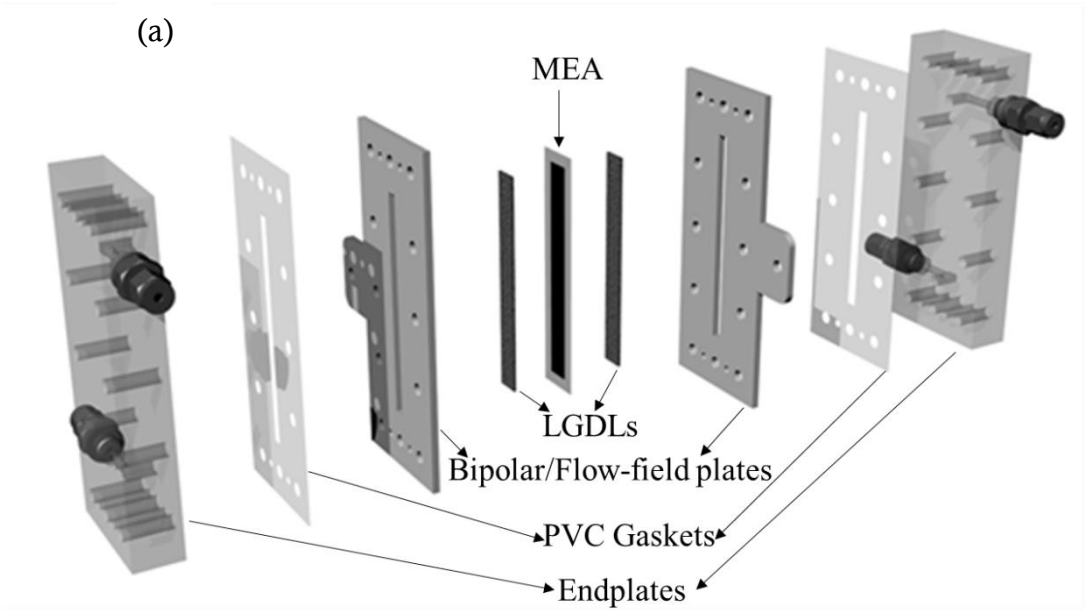

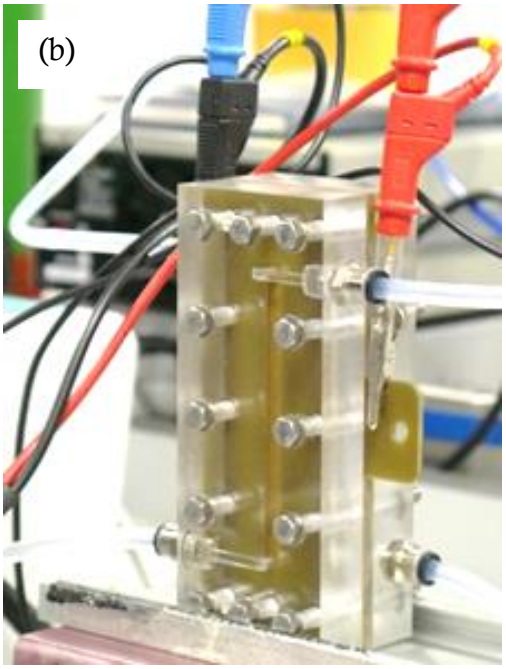

Figure 3.7. (a) Schematic of the single-channel PEMWE cell, (b) photograph of the assembled cell.

3.3 Test rig

Figure 3.8 shows the schematic and picture of the experimental setup including the electrolyser cell used in this study. DI water was supplied from a water reservoir to the PEMWE cell by a digital peristaltic pump (Watson Marlow 323U). The cell was operated at ambient pressure and heated to the desired temperature by preheating the inflowing deionized water supplied to both the anode and cathode side of the cell using a digital heated circulating bath (TC120, Grant Instruments Ltd). Excess unreacted water and product O_2 and H_2 gas are returned to the water reservoir where the gases are separated and vented while the DI water is recycled to the cell.

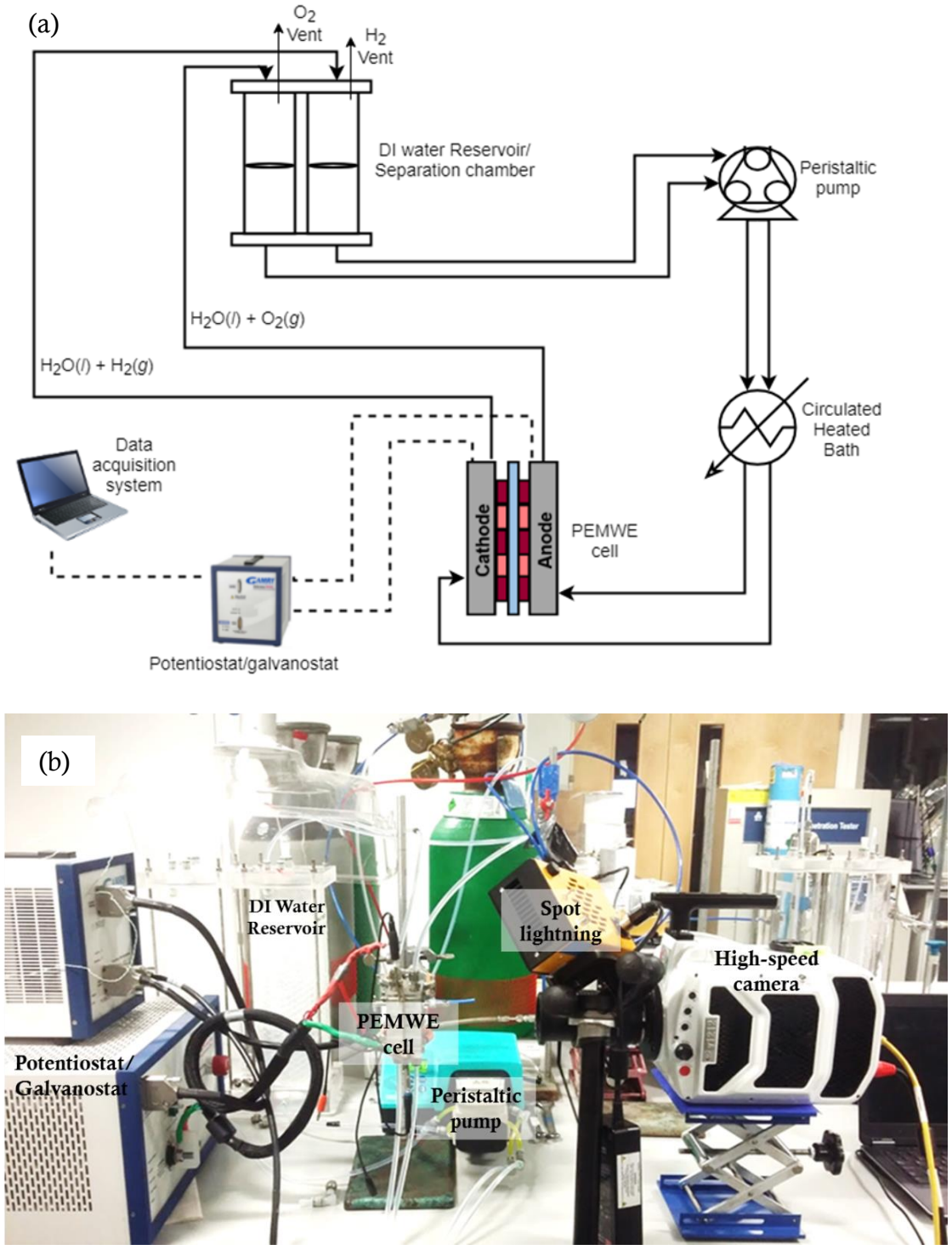

Figure 3.8. (a) Schematic of experimental setup for the measurements for simultaneous electrochemical measurement and high-speed imaging of two-phase flow in the PEMWE cell, (b) photograph of the experimental setup for optical imaging experiments.

3.4 Optical Visualization System

A CMOS high-speed imaging system (Phantom V1212, Monochrome) with a maximum resolution of 1280 × 800 pixels was employed in this experimental study with Nikon Micro-Nikkor 55mm f/2.8 lens to acquire continuous 10-bit images of the bubble evolution and two-phase flow behaviour of O_2 gas and water in the anode flow channel at 1000 frames per seconds. Adequate lighting is a key aspect of photography, especially during high speed imaging. Good illumination enables clear, definitive images to be recorded. Thus, an 84 W high-power LED lighting system (Photo-Sonics Ltd) which consists of an array of super bright LED lights was used to provide the high intensity illumination required for the high-speed imaging. The images were digitally evaluated using Phantom Camera Control (PCC, version v2.14.727.0.) software. Figure 3.8(b) shows an image of the high-speed camera and the lightings used in the study.

3.5 Electrochemical Characterization

3.5.1 Polarization measurements

The voltage–current polarization curves (*V–i* curves) were obtained using Gamry Reference 3000 Galvanostat/Potentiostat equipped with a Gamry 30k Booster (Gamry Instruments, USA). The data were acquired using the Gamry Framework software (version 6.24) on the potentiostat. In the polarization measurements, the cell electrolysis voltage was measured as the applied current was increased stepwise, at a scan rate of 0.1 A s^{-1} from 0.1 A to 30 A. Initial steady-state operation was ensured before all polarization curve measurement by applying an initial load of 0.1 A cm^{-2} to the cell for 15 min. A constant potential was attained within this time period, indicating the stability of the electrode. Three or more voltage-current polarization curves were run at all conditions investigated to test repeatability.

3.5.2 Electrochemical Impedance spectroscopy

Electrochemical impedance spectroscopy was performed at current densities of 0.1, 0.5 and 3.0 A cm^{-2} between 100 kHz and 0.1 Hz, with each test preceded by a conditioning period of 15 minutes at the respective current density to ensure steady-state operation. A variable AC perturbation of 5% of the DC value was applied

which was confirmed to be small enough not to interfere with the cell performance. The anode served as the working electrode, whereas the cathode was used as both counter and reference electrode. Impedance measurements were also done in triplicates for each test condition and were highly reproducible (standard deviation <0.5%). The impedance data in this study have been displayed in complex plane/Nyquist plots and the experimental impedance data were fitted using Zview software (Scribner Associates, Inc., v3.3d) to provide quantitative support for the discussion of the impedance results.

3.6 PTL Characterization

3.6.1 Scanning Electron Microscopy

Scanning electron microscopy (SEM) is used to reveal the surface morphology information on investigated material samples. In SEM, the surface of the sample is scanned in a raster pattern with a focused electron beam controlled by an accelerating voltage using an electron gun. Depending on the penetration depth, the electron beam interacts with atoms at various depths within the sample, producing signals such as back-scattered electrons (by elastic scattering) and secondary electrons (by inelastic scattering) which can be detected by specialized detectors. These signals are then amplified and displayed as variations in brightness in a computer-generated image.

In this study, SEM imaging was performed using an EVO MA 10 microscope (ZEISS, UK). PTL samples were cut into 5mm squares and gold-coated before imaging to prevent sample charging under the electron beam. The samples were then mounted onto stubs using adhesive carbon tape and placed in the SEM for imaging. Imaging was performed in a secondary electron mode at an electron accelerating voltage of 10 kV and a working distance range of 8-9 mm. Images of the surface structure were captured and collected using the built-in SmartSEM® image acquisition and processing software.

3.6.2 X-ray Micro-Computed tomography Imaging

In this research, laboratory-based micro-CT investigations were conducted using a ZEISS Xradia Versa 520 (Carl Zeiss Microscopy Inc., Pleasanton, USA) equipped

with micron spot size laboratory X-ray source with cone beam geometry which can achieve true spatial resolution of around 700 nm.

For each PTL investigated, the sample was carefully mounted onto a sample holder suited to the rotating sample stage of the X-ray instrument. All samples were scanned in pristine state and the scans were carried out with a source voltage of 150 kV with exposure time of 4 s per projection, acquiring 1801 projections per scan.

The raw transmission images from the scan were reconstructed using a commercial image reconstruction package (Zeiss XMReconstructor, Carl Zeiss X-ray Microscopy Inc. Pleasanton, CA), which uses a cone-beam filtered back-projection algorithm, resulting in a voxel volume of approximately 1.01 μm. A sub-volume of 800^3 voxels was extracted from each 3D volume to minimize computational requirements. An edge-preserving non-local means filter was applied to each dataset to reduce noise and aid phase segmentation. Segmentation of the solid and pore phases and 3D volume rendering of the resulting reconstructed volumes was performed using the Avizo software package (version 9.2. Thermo Fisher Scientific). Thresholding of the 3D volume was conducted based on the distinctive image contrast between the solid and pore phases, largely due to the disparate X-ray attenuation coefficients of titanium and air. Grey-scale and binary ortho-slices of each sample and 3D TIFF image files were generated. The segmented 3D TIFF image files were then processed for image-based quantification. The pore size distribution was obtained using commercial software (ImageJ v1.52d). The porosity distribution was obtained using pore quantification code implemented in MATLAB [159]. The bulk porosity and tortuosity factor were obtained using *TauFactor,* an open-source MATLAB software package which implements a diffusive flux-based approach for the determination of tortuosity factor [148].

3.7 Conclusions

In this chapter, the fundamental theory behind the diagnostic techniques used in this study was presented. These techniques include polarization curve, EIS, X-ray computed tomography, high-speed optical imaging, and design of experiment (DoE). Two optical PMWE cells were designed and fabricated for various studies including gas-bubble dynamics and two-phase flow characterization (Chapter 4),

effect of channel depth on PEMWE performance (Chapter 5), effect of PTL microstructure on performance (Chapter 6) and the investigation of critical mass transport parameters and their interactions (Chapter 7).

Chapter 4

Dynamic Two-Phase Flow Behaviour and Performance in the Anode Flow-Field Channels of a PEMWE

Sections of this work have been peer reviewed and published in the International Journal of Hydrogen Energy (J. O. Majasan, J. I. S. Cho, I. Dedigama, D. Tsaoulidis, P. Shearing, and D. J. L. Brett, *"Two-phase flow behaviour and performance of polymer electrolyte membrane electrolysers: Electrochemical and optical characterisation,"* Int. J. Hydrogen Energy, 2018. (doi:10.1016/J.IJHYDENE.2018.07.003) [160].

4.1 Introduction

Characteristics of gas-bubble evolution, two-phase flow behaviour and flow-field design are closely linked to the performance of PEMWEs. As reviewed in Section 2.7.1, only few studies in literature have studied the relationship between the two-phase flow behaviour in the flow channel and performance in PEMWEs. The majority of previous PEMWE studies were performed at relatively low current densities or have analysed two-phase flow in a single straight channel where the two-phase flow patterns are not fully representative. Others have modelled flow using flow regime maps rather than real-time flow visualization. Thus, an in-depth study of entire flow-fields that correlates design and real-time two-phase flow phenomena with performance at high current densities is desirable. Also, understanding the effect of operating parameters such as temperature, flow

circulation at anode only or at both electrodes (full circulation) and water feed rate on the two-phase flow behaviour at high current densities is essential for design and performance optimization.

This chapter examines the two-phase flow behaviour in a PEMWE in two different macroscopic anode flow-field designs in relation to the electrochemical performance. By using transparent endplates, direct visual inspection of the flow channels across the whole flow-field allows the gas-bubble dynamics and the two-phase flow behaviour to be recorded using a high-speed video camera at current densities up to 3.3 A cm^{-2}. Polarization curves (described in Section 3.1.1) were obtained to provide a fundamental understanding of the relationship between the two-phase flow behaviour and cell performance. The effects of various operating parameters including flow circulation at anode only or full circulation, water feed rate, and cell operating temperature were also investigated.

4.2 Experimental

4.2.1 Flow-Field Design

In this work, two types of flow field patterns were design and fabricated for testing at the anode: a single serpentine flow-field (SSFF) and a parallel flow-field (PFF), shown in Figure 4.1. The detailed structural parameters of each flow-field are presented in Table 4.1. The flow field plates were made of 1.6 mm thick PCB with an open ratio (ratio of channel area to MEA area) of 55.7% and provide a basis for comparison. The SSFF consisted of a single meandering flow channel having nine linked vertical segments (each 30 mm long) and eight horizontal segments (each 1.76 mm long), whereas the PFF comprised nine parallel straight channels, each 30 mm long. Both flow-field designs have channel depth of 1.6 mm and a channel and rib width of 1.76 mm to maintain the same open ratio.

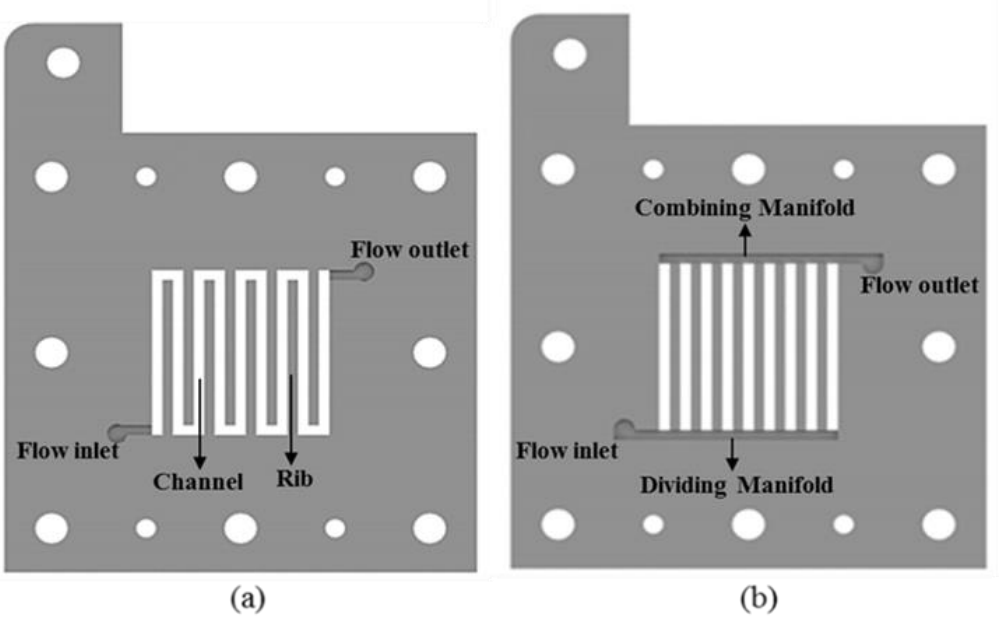

Figure 4.1. Flow-field designs (a) single –serpentine flow-field (SSFF), (b) parallel flow-field (PFF).

A 'diagonal flow mode' was adopted in both of the flow-field designs such that the water was fed to the flow-field from the lower left corner (as shown in Figure 4.1) while excess water and the gas produced was ejected at the upper right hand corner. Whereas the SSFF does not require a manifold and there is no flow branching, the PFF incorporates a dividing manifold at the bottom of the flow field and a combining manifold at the top (Figure 4.1(b)). Both manifolds have the same channel dimensions as the main flow channels. In the case of the PFF, the diagonal flow mode' is equivalent to a Z-type manifold configuration. As opposed to the U-type (where the outlet is on the same side as inlet), Z-type manifolding results in more uniform flow and pressure drop for fuel cells, electrolysers and cooling plates[161].

Table 4.1. Geometric parameters of the flow-fields

Parameters	SSFF	PFF
Effective area (cm^2)	9	9
Channel width (mm)	1.76	1.76
Channel length (mm)	270	30 (each)
Channel depth (mm)	1.6	1.6
Rib width (mm)	1.76	1.76
Open ratio (%)	55.70	55.70

4.2.2 Electrochemical Measurement

The voltage–current polarization curves (*V–i* curves) were obtained using Gamry Reference 3000 Galvanostat/Potentiostat equipped with a Gamry 30k Booster (Gamry Instruments, USA). The data were acquired using the Gamry Framework software (version 6.24) on the potentiostat. In the polarization curve measurements, the cell electrolysis voltage was measured as the applied current was increased stepwise, at a scan rate of 0.1 A s^{-1} from 0.1 A to 30 A. Initial steady-state operation was ensured before all polarization curve measurement by applying an initial load of 0.1 A cm^{-2} to the cell for 15 min. A constant potential was attained within this time period, indicating the stability of the electrode. Three or more voltage-current polarization curves were run at all conditions investigated to test repeatability.

4.2.3 Optical Imaging

The anode flow-field of the PEMWE cell was visualized in-situ at current densities ranging from 0.1 A cm^{-2} to 3.3 A cm^{-2}; three operating temperatures of 25°C, 45°C, and 80°C; and four different water feed rates of 15, 30, 45 and 60 ml min^{-1}. The flow velocity was determined by tracking the movement of bubble/slug from consecutive images based on the time interval (number of frames) for the bubble/slug to travel a given distance.

Notionally, a value of $\xi = 1$ is sufficient to sustain the electrolysis reaction at the anode. However, a value of $\xi = 5$ is typical in actual operation of large cells or stacks to prevent electrode starvation or membrane dehydration [162]. Based on

calculations using Eq. (2.5), for the range of current density and inlet water feed rates used in this study, ξ ranges between 7.5 at 3 A cm^{-2} when operated at 15 ml min^{-1} and 30 when operated at 60 ml min^{-1}. This implies that the water feed rates (15, 30, 45 and 60 ml min^{-1}) used are always in significant stoichiometric excess and sufficient to keep the MEA well hydrated throughout the electrolysis operation.

4.3 General features of gas-bubble dynamics in the anode flow-field of the PEMWE.

Before examining the specific features of different flow-field designs and operating conditions, generic features of the bubble distribution and flow characteristics in the flow channels are considered. In general, the lighter areas in the images represent single-phase liquid flow and areas containing small bubbles; whereas the darker areas correspond to larger bubbles or slug flow, through which the dark PTL/electrode becomes visible through the gas phase. The change in shape, size and flow regimes of gas bubbles with an increase in current density for any single channel showed the following general trend. At very low current density, numerous small, spherically-shaped gas bubbles emerge from various locations on the PTL surface and remain attached due to surface tension forces. The gas bubbles become detached when the dynamic pressure of the flowing water exceeds the surface adhesion force and the gas bubbles join the flow of water. Initially, the bubbles are dispersed in the flow of liquid water, characterised by the bubbly-flow regime.

As current increases and more gas is produced, and/or as the bubbles depart and coalesce with newly formed bubbles further along the channel, transition to the slug flow regime occurs. This regime is characterized by elongated 'cylindrical' bubbles also known as Taylor bubbles, whose lengths are several times larger than the width of the channel. As more gas is produced with further increase in current density, the gas void fraction increases and strings of Taylor bubbles separated from one another by clusters of small bubbles move along the channel. The slug flow, in which bubbles fill the majority of the channel cross-section, with only a thin boundary layer of water at the edges, has a 'sweeping' effect on the nascent bubbles forming at the surface of the PTL, and acts to clear the channel along the downstream region. As will be shown below, in a flow-field with extended channel length (the

SSFF in our case), as more gas is produced at high current densities, the two-phase flow enters a regime known as annular flow, where most of the liquid flows along the channel walls as the central channel core is dominated by long gas slugs. The process of bubble emergence, growth, detachment, coalescence and eventual sweeping by slug or annular flow was a feature observed across the range of flow-field designs and operating conditions examined.

4.3.1 Two-phase flow behaviour in the Single Serpentine Flow-field (SSFF)

Figure 4.2(a) shows the cell polarization curve obtained for the SSFF operated at a temperature of 80°C and inlet water feed rate of 15 ml min^{-1}. Figure 4.2(b) shows the images of the SSFF at selected current densities corresponding to Points A to H in Figure 4.2(a). The images show that the total amount of gas present in the flow channel increases continuously with increase in current density.

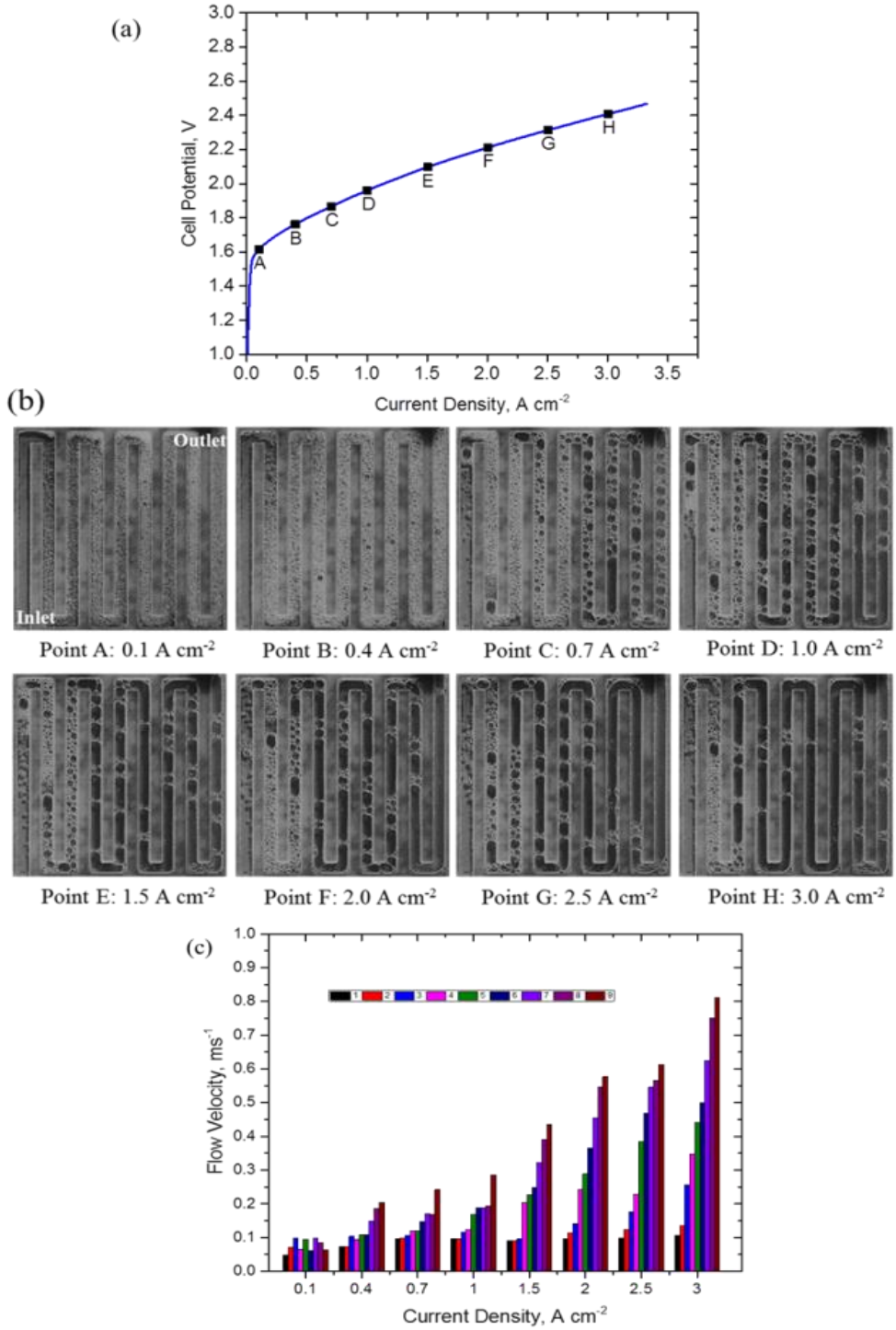

Figure 4.2. (a) Polarization curve for SSFF design at a temperature of 80°C and water feed rate of 15 ml min^{-1}; (b) O_2 gas-bubble behaviour at selected current densities; and (c) flow velocity profile in sub-channels 1 to 9 of the SSFF at various current densities.

At very low current density of 0.1 A cm^{-2}, corresponding to point A, numerous tiny bubbles were observed in the flow channel. Then, as current density increased to 0.4 A cm^{-2}, corresponding to point B, the quantity and size of the gas bubbles increased significantly due to increased gas generation and bubble coalescence, and the flow pattern observed is described as the bubbly regime. As current density increased to 0.7 A cm^{-2} (Point C), gas fraction and bubble coalescence along the channel length increased leading to the formation of larger spherical bubbles and emergence of short cylindrical gas slugs along the channel downstream. The short gas slugs coexist with the smaller bubbles present and the flow pattern observed is described as an intermediate between the bubbly and slug regime. Also, along with the emergence of slugs, the flow velocity starts to increase for each sub-channel.

As current density increased to 1.0 and 1.5 A cm^{-2}, corresponding to point D and E, longer gas slugs are formed accompanied by a corresponding increase in flow velocity. At these current densities, the flow channel is observed to be divided into two regions, the downstream dominated by pockets of long cylindrical gas slugs separated by spherical gas bubbles, and the upstream region filled with relatively smaller gas bubbles. At the high current densities of 2.0, 2.5 and 3.0 A cm^{-2}, corresponding to points F, G and H, respectively, the gas slug grows rapidly along the meander as the smaller bubbles coalesce earlier along the channel. Thus, at these high current densities, a larger portion of the flow channel is filled with continuous meandering gas slugs (annular regime). At an average current density of 3 A cm^{-2} (Point H), about 80% of the flow channel is filled with continuously meandering gas slugs; as only the two sub-channels closest to the channel inlet are slug-free.

An interesting feature of the two-phase flow in the SSFF is that the channel corners (switchbacks) were convenient locations for the coalescence of gas bubbles/slugs. Gas bubbles and slugs were more likely to coalesce when they go around the corners, which might have significant implication for the transition between flow regimes.

The flow velocity in each of the nine sub-channels of the SSFF design is presented in Figure 4.2(c). The flow velocity was determined by tracking the movement of bubble/slug from consecutive images based on the time interval (number of frames) for the bubble/slug to travel a given distance. It is evident that at a given current density, the velocity increases along the length of the meander from the inlet to the outlet. The lowest velocity was recorded in the sub-channel closest to the inlet (sub-channel 1) and the highest velocity recorded in the sub-channel closest to the outlet (sub-channel 9) for each current density considered. Also, the increase in flow velocity across the flow-field was observed to correspond to slug formation. As gas bubbles accumulate and coalesce along the channel length, the void fraction of the gas-phase thus increases with channel length and consequently slugs are formed along the channel downstream. The increased gas void fraction and slug formation towards the channel downstream thus lead to decrease in the cross-sectional area of the liquid-phase flow which increases the flow velocity.

4.3.2 Two-phase flow in Parallel Flow-field (PFF)

Figure 4.3(a) shows the cell polarization curve obtained for the PFF operated at a temperature of 80°C and water feed rate of 15 ml min^{-1}. Figure 4.3(b) illustrates the corresponding images of the two-phase flow behaviour at selected current densities on the polarization curve, which correspond to Point A to H in Figure 4.3(a).

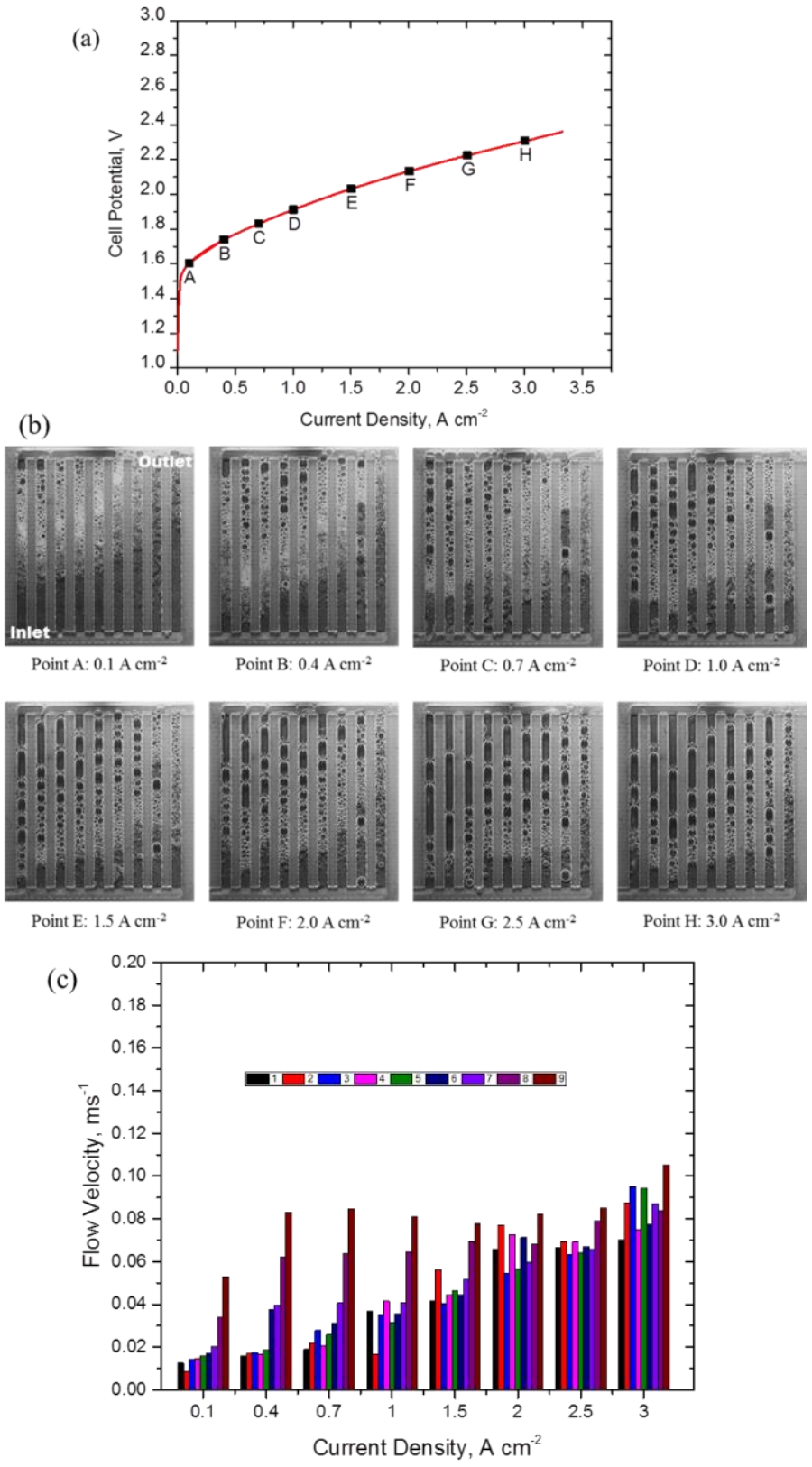

Figure 4.3. (a) Polarization curve for PFF design at a temperature of 80°C and water feed rate of 15 ml min^{-1}; (b) anode two-phase flow behaviour at selected

current densities; and (c) flow velocity in the PFF channels 1 to 9 at various current densities.

It can be seen from Figure 4.3(b) that in the PFF, the quantity of gas and hence the size of gas bubbles, increased with current density, consistent with the observations in Figure 4.2(b). Depending on the current density, for any given channel there is the trend for the flow regime to evolve as described above for the SSFF. However, the PFF shows a non-uniform distribution of flow between the channels. The liquid flow rate was highest in the channel farthest from the inlet and lowest in the channel closest to the inlet. This is attributed to the well-known inertial effect of fluid flow out from a dividing manifold into multiple T-junctions, which makes the fluid prefer the straight direction (horizontally along the manifold) rather than branching (vertically into the channels) [161]. This has an important effect on the resultant two-phase flow evolution in each of the channels.

At low current density of 0.1 A cm^{-2}, corresponding to Point A in Figure 4.3(a), the lower portion of the channels are filled with liquid water with the upper portion consisting mainly of gas bubbles with width smaller than the channel cross-section. It can be seen that the quantity of bubbles in the channels varies, with the channel closest to the inlet having a large quantity of tiny bubbles whereas the channels furthest from the inlet have a significantly smaller amount of bubbles due to the higher flow velocity and consequent lower gas volume fraction. This trend was observed at all current densities considered for flow visualization and is attributed to non-uniform distribution of flow in the channels. As current density increased to 0.4 A cm^{-2} (point B), both the quantity and size of the gas bubbles have increased markedly, with increase to 0.7 A cm^{-2} (Point C) bubble coalescence leads to emergence of short gas slugs in the channels closest to the cell inlet while the other channels remain noticeably bubbly.

As the average current density increased to 1.0 and 1.5 A cm^{-2}, corresponding to point D and E, short gas slugs begin to form in the middle channels, while the early-appearing gas slugs in the channels closest to the inlet begin to lengthen and move downstream. A similar trend was observed at higher current densities of 2.0,

2.5 and 3.0 A cm^{-2} corresponding to points F, G and H respectively. Further gas generation and bubble coalescence led to the formation of gas slugs in the channels farther away from the inlet, and at 3.0 A cm^{-2}, only the two channels furthest away from the inlet remain exclusively bubbly. The overall trend in this flow-field pattern is a transition from bubbly to slug regime and occurs at progressively longer times as the channels move away from the manifold inlet.

Notably, the transition to gas slugs spanning entire flow channels (annular regime) did not occur in this flow-field configuration because the gas slugs enter the combining manifold before this transition could occur. Figure 4.3(c) shows the flow velocity in the PFF channels corresponding to various current densities tested at inlet water feed rate of 15 ml min^{-1}. It can be seen that the flow velocity increased approximately linearly (within the error of flow velocity measurements) with average current density (ranging from a flow velocity of 0.02 m s^{-1} at 0.1 A cm^{-2}, to 0.09 m s^{-1} at 3 A cm^{-2}), which is consistent with a linear increase in gas generation (gas void fraction) and constant water inlet flow. However, the distribution of flow velocities across the nine channels changes, becoming increasingly uniform with increasing current density. Numerous factors will affect this flow distribution, the two-phase flow state of the combining manifold being one of them, but in general gas-filled channels (higher gas void fraction) will present a lower pressure drop (i.e. channels towards the water intake), thus acting to balance the flow velocity into each channel. It should be noted that the theoretical flow velocity, assuming single-phase water flow through the channels equally, is calculated to be 0.01 m s^{-1}, which implies that, as expected, the presence of gas increases the flow velocity in the channels at the current densities considered.

4.4 Performance Comparison in Serpentine and Parallel Flow-field designs

Figure 4.4 compares the performance of the PFF and SSFF designs. The experiments were performed at two water feed rates (15 ml min^{-1} and 60 ml min^{-1}) and a fixed inlet water temperature of 80°C. It is clear from Figure 4.4(a) and (b) that for the same water feed rate the PFF showed better performance than the SSFF, especially at higher current densities. For instance, at 3 A cm^{-2} for water feed

rate of 15 ml min^{-1}, the PFF performed better by about 100 mV compared to the SSFF. The improved performance observed in the parallel flow-field design compared to the single serpentine flow field has also been reported in previous work by Ito *et al.* [91].

To explain this observation, we compare the performance (polarization) curve results with the flow visualization results presented in previous Section 4.3. Two key differences can be observed in the visualization results of the two flow designs. First, the flow velocity in the two designs differs markedly (Figure 4.4(c)). The flow velocity is significantly higher in the SSFF than in the PFF design. More so, in terms of general trend, the flow velocity in the SSFF increased approximately linearly across the flow-field, while in relative terms there is hardly any velocity variation across the channels for the PFF. This difference in velocity is attributed to the fact that only a single meandering channel is present in the SSFF, whereas in the PFF the inlet flow is divided between the channels (nine, in this case). Since coalescence increases rapidly along the single channel length in SSFF, longer gas slugs are formed, and the flow velocity is noticeably higher in the upper part of the channel. Higher flow velocities have been reported to improve mass transfer in DMFCs [163], [164]. However, the evidence presented here suggests that this is not the case in PEM electrolysers. Therefore, attention turns to the other key difference in the two-phase flow behaviour of these flow-field designs, which is the flow regime of operation. As discussed in Section 4.3, the bubble dynamics and two-phase flow regime differ markedly for the SSFF and PFF flow designs. In the SSFF, at a current density of 3.0 A cm^{-2}, a flow regime described as annular flow is observed, where continuous channel-filling gas slugs occupy the channel core with a thin layer of water flowing only at the walls.

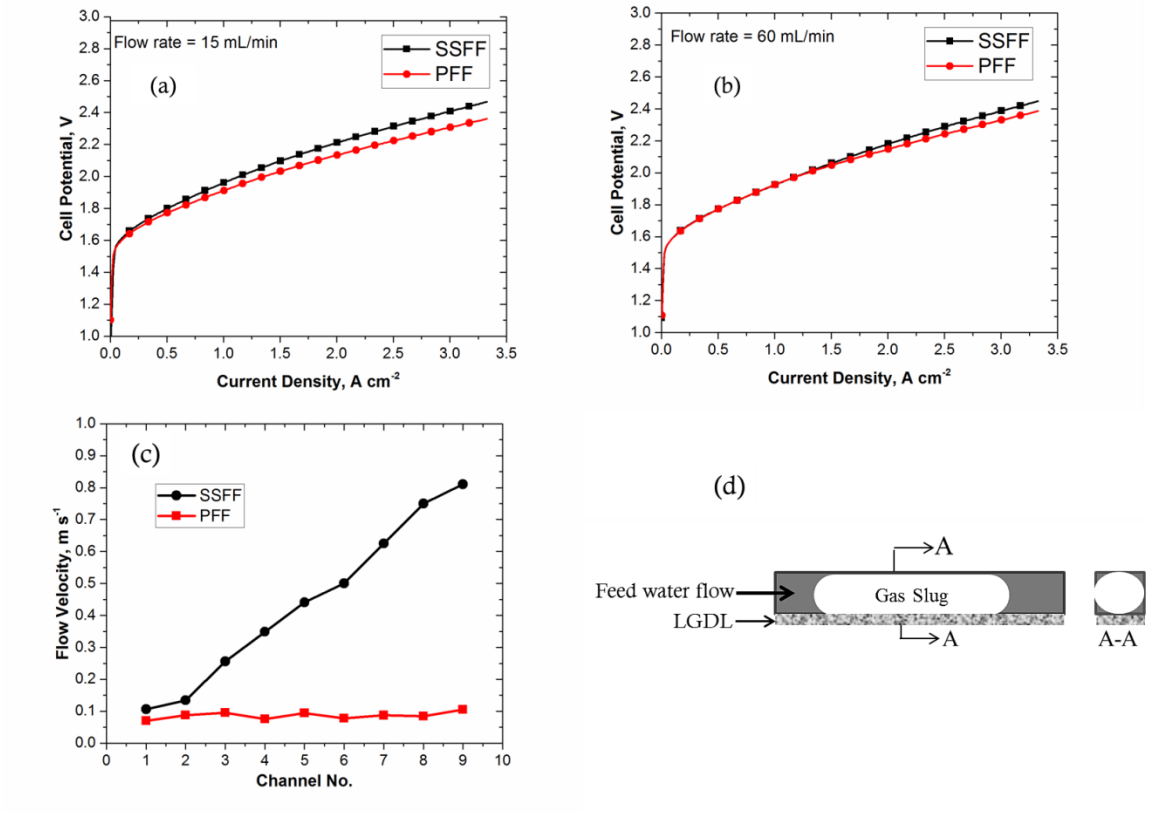

Figure 4.4. Performance curve of PEM electrolyser equipped with different flow-fields at water feed rates of (a) 15 ml min-1 and (b) 60 ml min-1 at an inlet water temperature of 80°C; (c) comparison of flow velocity in the flow channels for the two flow-field designs at 3 A cm^{-2} at an inlet water feed rate of 15 ml min^{-1}; (d) illustrated model of gas slug in flow-field channel showing the probable PTL-blocking action.

In this situation, as depicted in the model in Figure 4.4(d), it can be seen that the presence of long gas slugs spanning almost the entire length of the channel can block the access of water to the PTL and lead to a deterioration in performance. This might explain why performance was worse in the SSFF, where continuous gas slugs spanning about 80% of the entire channel length can be found in the annular flow regime; whereas in the PFF, gas slugs formed towards the upper part of the channel rapidly exit into the combining manifold. Thus, in the PFF, due to its short channel length, the discontinuous gas slugs formed are removed before they could develop into annular flow. Moreover, the effect of the fully developed gas slug in

removing bubbles and clearing the channel, described by Dedigama *et al.* [94], is more pronounced in the PFF due to the shorter channel length. This observation, therefore, suggests that in terms of the two-phase flow behaviour in the PEMWE, the key performance-influencing difference between the SSFF and the PFF is the length of the flow path and hence the flow regime. The shorter flow path for gas removal in the PFF seems to enhance performance, and conversely, the elongated flow path of the SSFF allows gas accumulation and coalescence along the channel length that develops into annular flow that might hinder adequate water access to the electrocatalyst layer through the PTL. Since the higher flow velocity in the SSFF did not lead to better performance, as predicted by similar DMFC research, it is inferred that the transition to annular flow regime exerts a higher impact than flow velocity on mass transport limitation and hence performance in PEMWEs.

The mass transport is directly proportional to the pressure drop between inlet and outlet of the cell. Hence, the pressure drop is expected to affect the performance of PEMWE depending upon flow field design pattern. To predict the disparity of pressure drop behaviour within the flow-fields, a larger pressure drop is expected in the SSFF due to the longer path length for fluid flow. However, this is not expected to be the case for a PFF which has several straight branches to deliver the liquid water so that there several distributary streams over the whole flow field. Under this condition, all the branch channels share the total amount of water fed through the same manifold. As a result, the water feed rate and pressure must be separated by each single channel.

4.5 Effect of operating conditions on the two-phase flow behaviour and cell performance

4.5.1 Effect of feed water circulation on cell performance

In PEMWE operation, water molecules accompany the transfer of protons from the anode to the cathode through the polymer electrolyte membrane, a phenomenon known as electroosmotic drag. Consequently, provided there is sufficient water at the anode, the membrane can be kept hydrated without an external supply of water to the cathode. However, water circulation at both electrodes is possible and is used

in some commercial systems [165]. Thus, it is possible to operate with no water flow at the cathode (anode-only circulation), with stagnant water at the cathode, or with full water circulation at both cathode and anode. Figure 4.5 presents the results of anode-only circulation and full circulation at both anode and cathode obtained at temperatures of 25 ˚C and 80 ˚C and water feed rates of 15 ml min^{-1} and 60 ml min^{-1} in the cell equipped with the PFF.

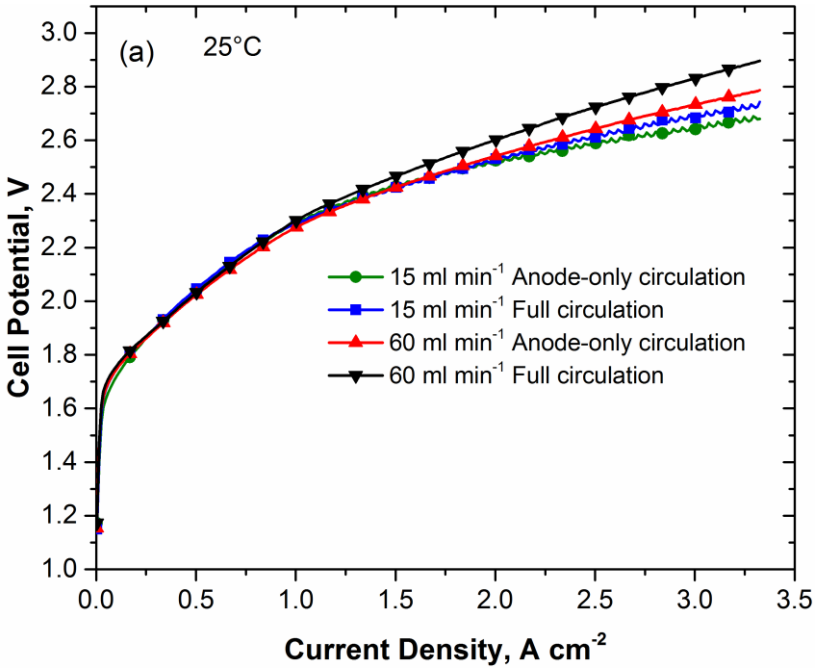

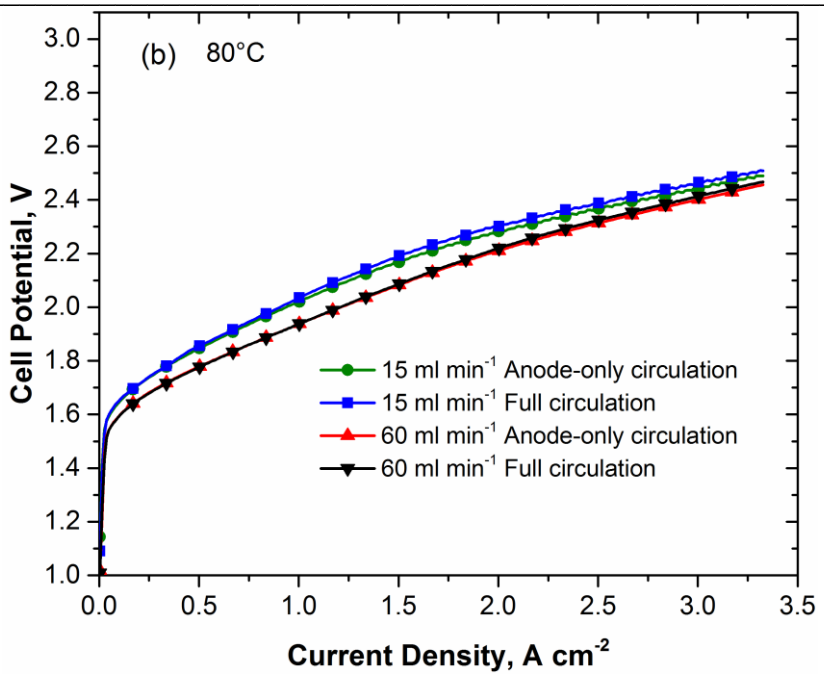

Figure 4.5. Effect of feed water circulation on performance at (a) 25°C and (b) 80°C using the PFF design at the cell anode and water feed rates of 15 ml min^{-1} and 60 ml min^{-1}.

As can be seen in Figure 4.5(a), at 25˚C, the full circulation showed worse performance than the anode-only circulation at both feed rates tested, the performance being worse at the higher feed rate. However, at 80˚C, (Figure 4.5(b)), the cathode flow conditions shows little to no effect on the electrochemical performance at both feed rates tested, the performance being worse at the lower feed rate (in contrast to the 25˚C case). This is attributed to a thermal effect in which the Joule heating associated with operation at high current density has a beneficial effect on the proton conductivity of the membrane electrolyte. Both higher anode feed rate and additional cathode recirculation act to cool the cell. At 80˚C the cell is close to thermal equilibrium, and the flowing water does not have a cooling effect. Thus, full water circulation at this higher temperature has little to no impact on the cell performance.

4.5.2 Effect of water feed rate on two-phase flow and performance

Figure 4.6 shows the effect of anode water feed rate (15, 30, 45 and 60 ml min^{-1}) at a range of temperatures (25, 45 and 80°C) investigated using an anode-only water circulation.

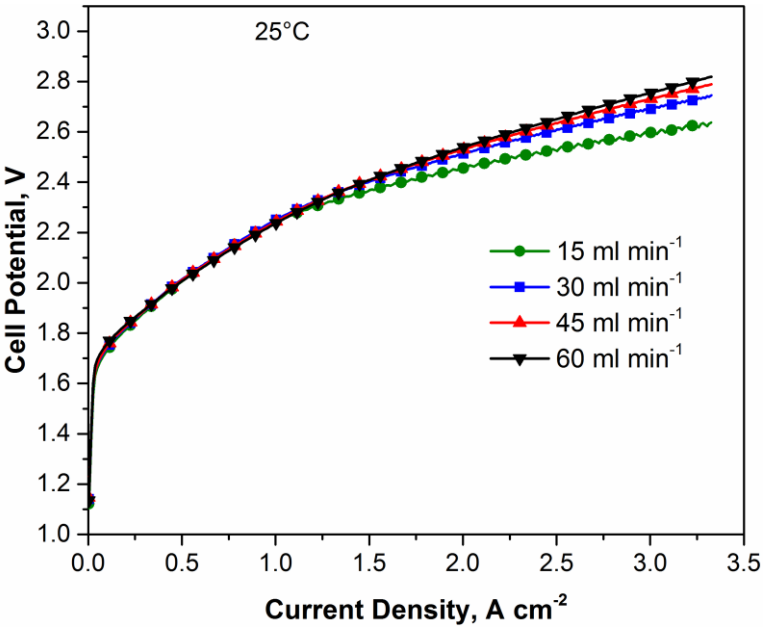

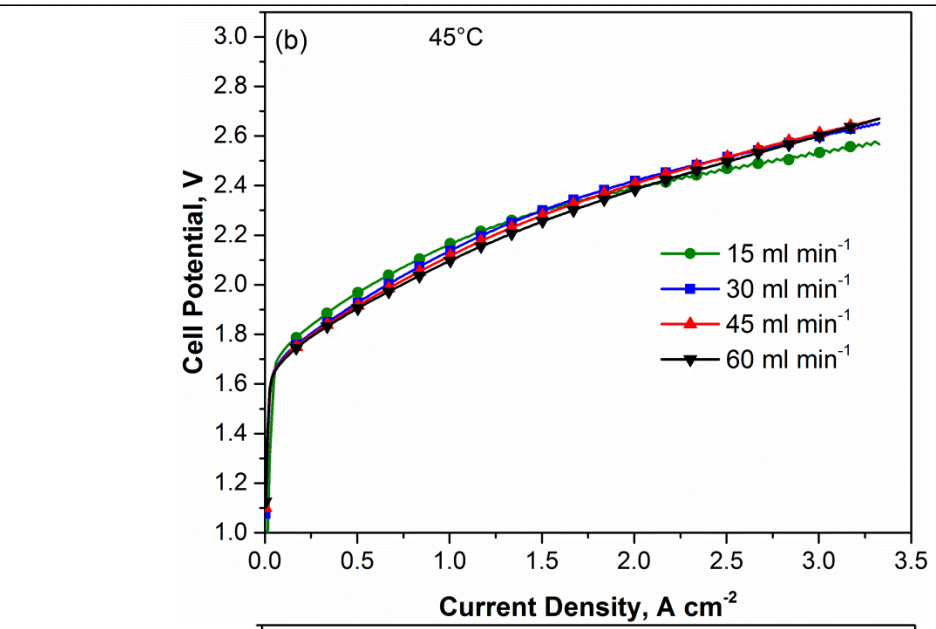

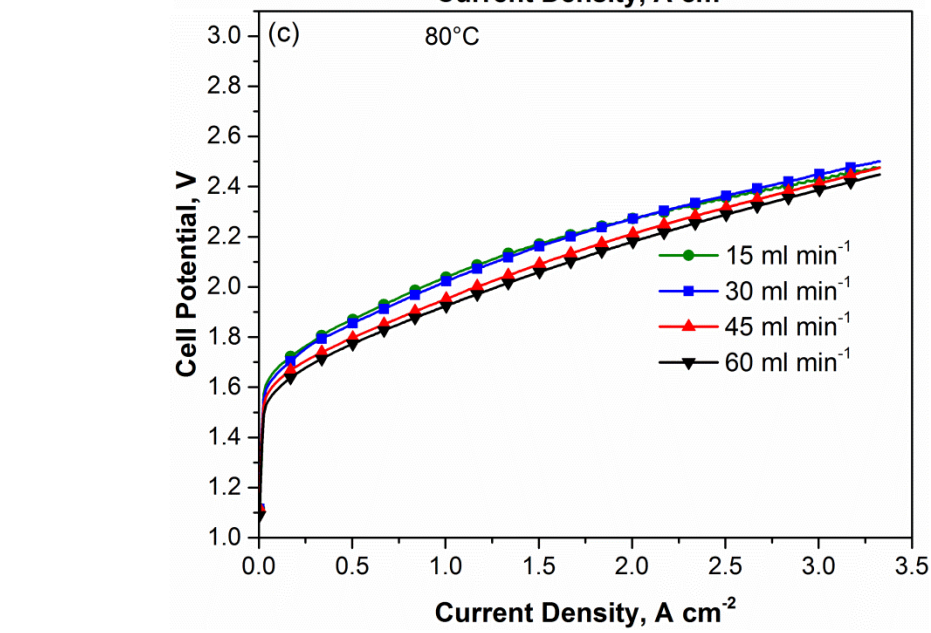

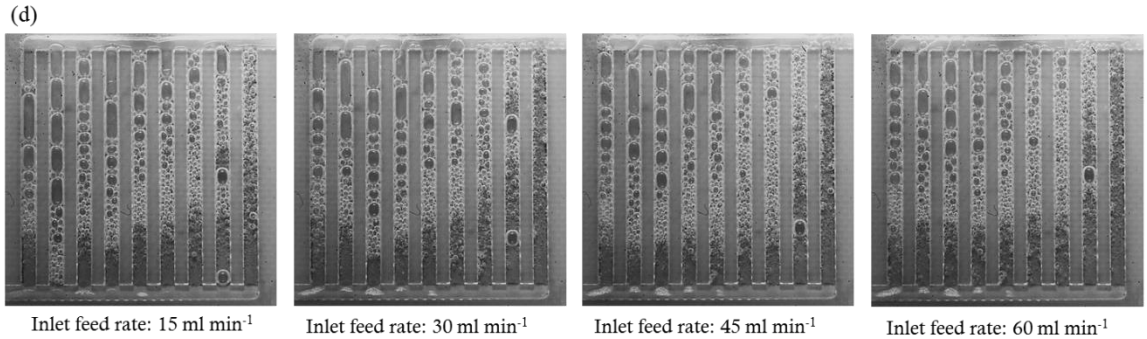

Figure 4.6. Effect of water feed rate on performance at different temperatures (a) 25°C, (b) 45°C, (c) 80°C, (d) the two-phase flow behaviour under different anode feed rates at 2 A cm^{-2} and 80°C using an anode-only circulation.

It can be seen that the performance trend with increasing anode water feed rate changes from being deleterious at low temperature (25°C) to advantageous at high temperature (80°C), with relative insensitivity at intermediate temperature (45°C). As described in Section 4.5.1, water feed rate has a significant effect on performance at low water inlet temperature due to its cooling effect at higher current density when significant heat is being generated from the electrolyser. At the relatively high temperature of 80°C, cell performance improves slightly with an increase in feed rates. This is attributed to the greater heat being supplied through the enthalpy of the higher flow water stream and ensures good reactant availability to the anode electrode. Also, from the two-phase flow perspective (Figure 4.6(d)), the slug length is shortened with reduced residence time as water feed rate is increased from 15 ml min^{-1} to 60 ml min^{-1}. As a result, an increased effective contact area between inlet feed water and the PTL enhances mass transfer leading to improved cell performance.

4.5.3 Effect of cell operating temperature on two-phase flow and performance

Figure 4.7 show the effect of temperature on PEMWE at a water feed rate of 15 ml min^{-1}. The experimental results indicate that cell performance improved with increasing temperature. At a current density of 3.0 A cm^{-2}, increasing the operating temperature from 25°C to 80°C resulted in a 242 mV improvement in cell potential. The improvement in performance with temperature can be explained by two reasons. First, at high temperatures, the activation overpotential is reduced, and the reaction kinetics is improved, which leads to an acceleration of the electrochemical reaction and improved performance. Also, the ohmic cell resistance is reduced at elevated temperatures since the ionic conductivity of the Nafion membrane (the largest contributor to ohmic resistance) is enhanced at high temperatures, provided sufficient membrane hydration can be ensured. This improvement in cell performance at high temperatures has been well reported [69], [166], [167]. Figure 4.7(b) shows the effect of temperature on the two-phase flow at a current density of 2.0 A cm^{-2}. More gas bubbles are observed in the channels at higher inlet water temperature despite the same total current and amount of O_2 generated. This is attributed to the effect of temperature on the ideal gas law and the fact that oxygen

solubility in water is strongly temperature dependent and decreases at higher temperatures.

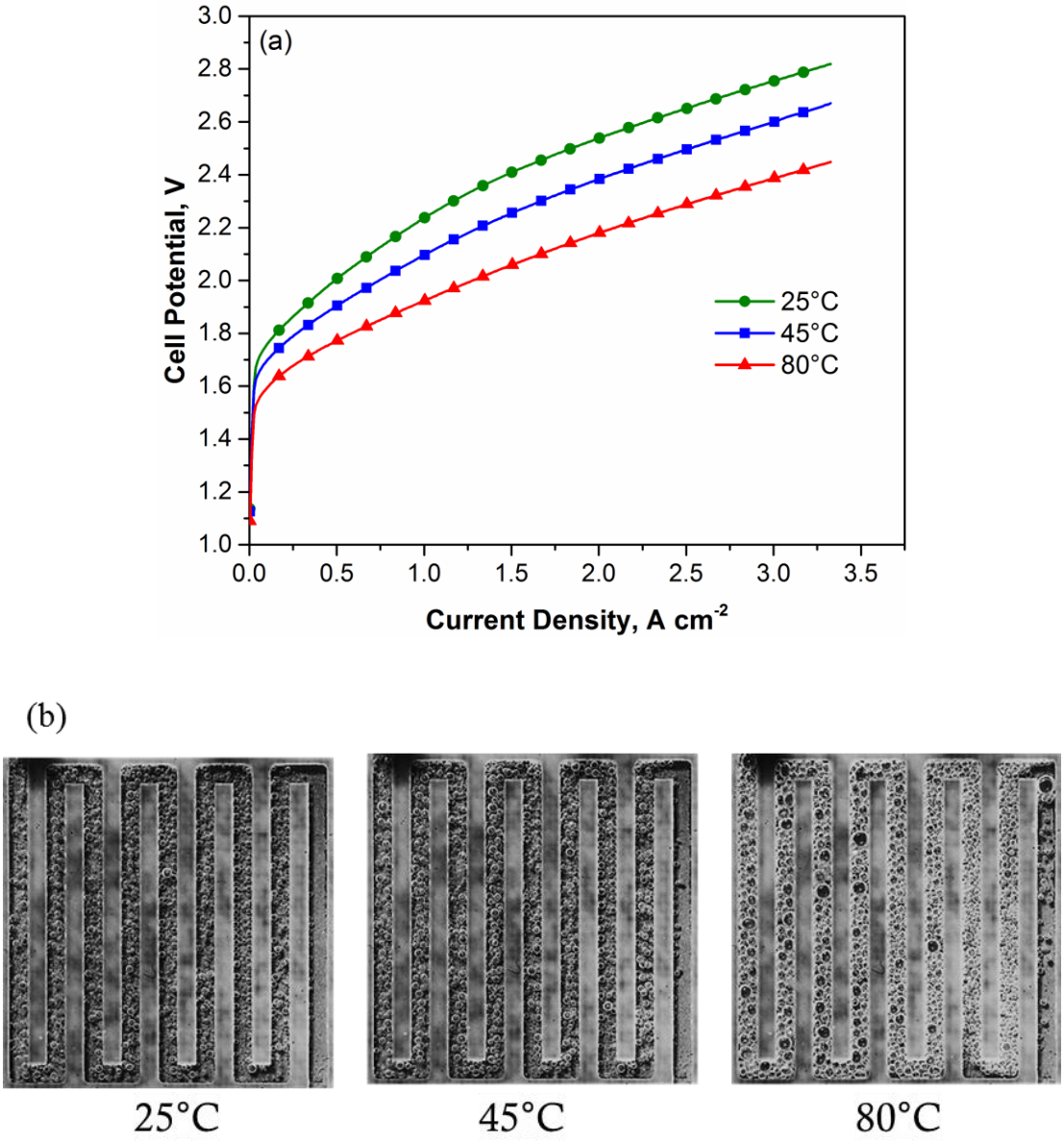

Figure 4.7. (a) Effect of temperature on PEMWE performance, (b) two-phase flow behaviour under different operating temperatures at a current density of 2 A cm^{-2} and water feed rate of 15 ml min^{-1}.

4.6 Conclusion

Understanding the two-phase flow behaviour is important for design and performance improvement in PEMWEs. In this chapter, the two-phase flow behaviour in the anode flow channel of a PEMWE was investigated using

optical visualization and related to the electrochemical performance for two commonly used flow-field designs. The effect of different operating parameters such as water circulation, water flow rate, and temperature on cell performance was also explored.

The results showed that the flow-field design affects two-phase flow behaviour and hence, performance in the PEMWE cell. The length of gas slugs and therefore the flow regime of operation are influenced by the path length of the flow-field channel. It was found that the PFF yielded better performance than the SSFF at high current densities under identical operating conditions; attributed to the annular flow regime observed in the SSFF design where the channel-spanning long gas slugs formed hinders water access to the gas diffusion layer and electrocatalyst surface. Also, a higher water flow rate delays bubbly-to-slug transition and leads to the formation of smaller bubbles and shorter slugs and the effect of the water flow rate on performance was found to depend on the cell operating temperature.

Simultaneous electrochemical characterization combined with optical visualization has undoubtedly extended the understanding of two-phase flow in PEMWEs, revealing the various flow regimes and their impact on performance, which is expected to greatly influence flow-field design and modelling efforts for improved performance in PEMWE. In addition to flow-field configuration, flow channel geometry such as depth, width and land-to-width ratios can also influence two-phase flow behaviour and hence performance. Thus, the investigation of the effect of channel depth on the performance characteristics is presented in Chapter 5.

Chapter 5

Effect of Flow-field Channel Depth on Two-phase Flow and Performance of PEMWE

Sections of this work have been peer reviewed and published in ECS Transactions: J. O. Majasan, J. I. S. Cho, M. Maier, I. Dedigama, P. Shearing, and D. J. L. Brett, *"Effect of Anode Flow Channel Depth on the Performance of Polymer Electrolyte Membrane Water Electrolyser*, *ECS Trans.*, vol. 85, no. 13, pp. 1593–1603, 2018.

5.1 Introduction

The bipolar/flow-field is a vital component of the PEMWE; it supplies the reactant liquid water to the active sites of the MEA, removes the produced H_2 and O_2 gases, distributes the applied current and provides structural support for the thin MEA [55]. Sub-optimal design of the flow-field could result in mass transport hindrance, which degrades performance. Therefore, well-designed and optimized flow-field plates are required for designing efficient and cost-effective PEMWE stacks, especially at high current densities [55], [91]. Most of the research efforts on flow-field development for PEM electrolyser in the literature have focused on optimization of the flow-field pattern [61], [91], [94], [97], [106], the influence of channel geometry such as channel depth on electrolyser performance has not been explored largely due to the difficulty in fabricating flow plates having various depth profiles.

This chapter presents a first attempt at filling that gap to understand the effect of anode channel depth on cell performance. First, in order to explain the relationship between the channel depth and the performance of the PEM electrolyser, the theoretical flow velocities corresponding to various channel depths are calculated. Then, using electrochemical impedance spectroscopy (described in section 3.1.2), the influence of channel depth on performance is investigated.

5.2 Flow-field design

The effect of anode channel depth was investigated under the condition of the same channel width (5.0 mm) and the same channel length (90 mm), but varying anode channel depth from 3.0 mm to 4.5 mm, 6.0 mm, and 8.0 mm as shown in Figure 5.1.

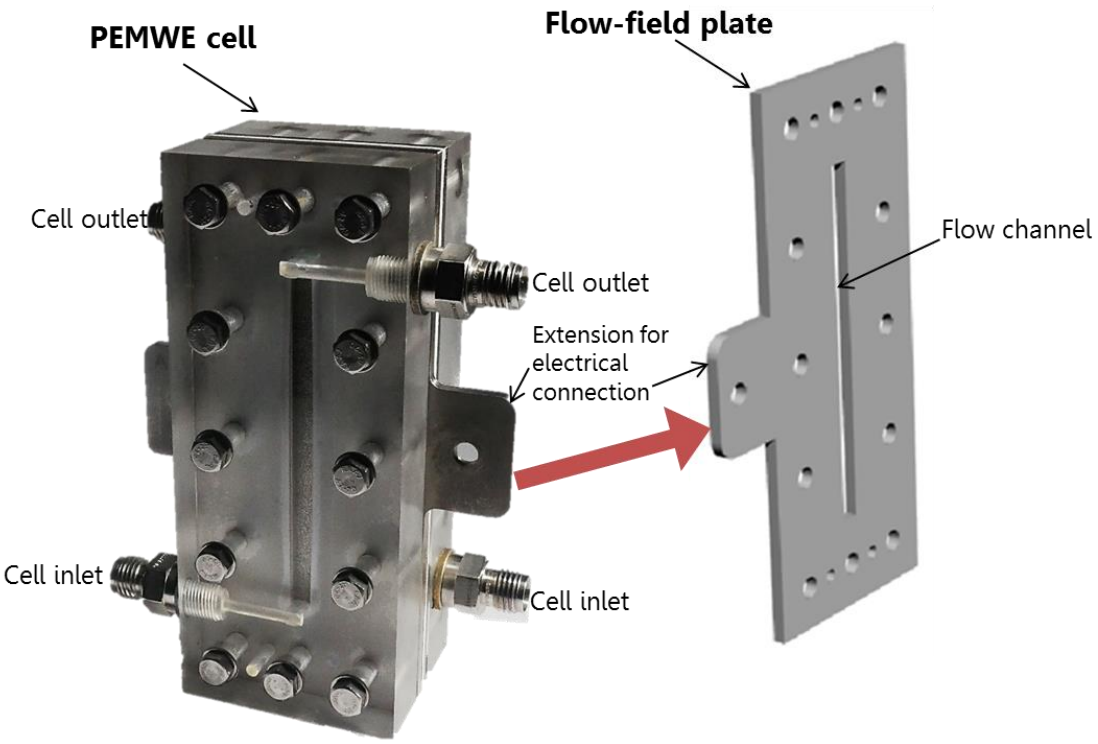

Figure 5.1. Photograph showing the single-channel PEMWE cell assembly and the and the anode flow-field plate.

5.3 Electrochemical Impedance Spectroscopy

EIS measurements were obtained using a Gamry Reference 3000 galvanostat/potentiostat equipped with a Gamry 30k Booster (Gamry Instruments, USA) in two-electrode set-up with the anode as the working electrode and the cathode as the reference electrode. The scanning frequency was varied from 100 kHz to 0.1 Hz probing the high-, medium- and low-frequency responses of the P cell, and recorded with 10 points of data per decade. A variable AC perturbation of 5% of the DC value was applied. To achieve steady-state before EIS testing, the electrolyser was operated at the respective current density for 30 min until a steady state voltage was obtained. Typically, 2-3 impedance measurements were carried out at each current density for each flow channel depth tested. All the trends in performance were preserved, and cell performance was repeatable to within 5%. Impedance data have been displayed using the complex plane (Nyquist) plot and parameters were extracted from the impedance curves by fitting the experimental data to the equivalent circuit (EC) using Zview software (Scribner Associates, Inc., v3.3d).

5.4 Relationship between Channel Depth and Flow Velocity

First, the flow velocity was calculated based on the single linear channel cell configuration. The flow velocity is defined as the volumetric feed rate divided by the cross-sectional area of the channel. Figure 5.2 shows the graph of the theoretical flow velocity as a function of channel depth. The plot shows that at a given volumetric feed rate, the velocity decreases with increase in channel depth.

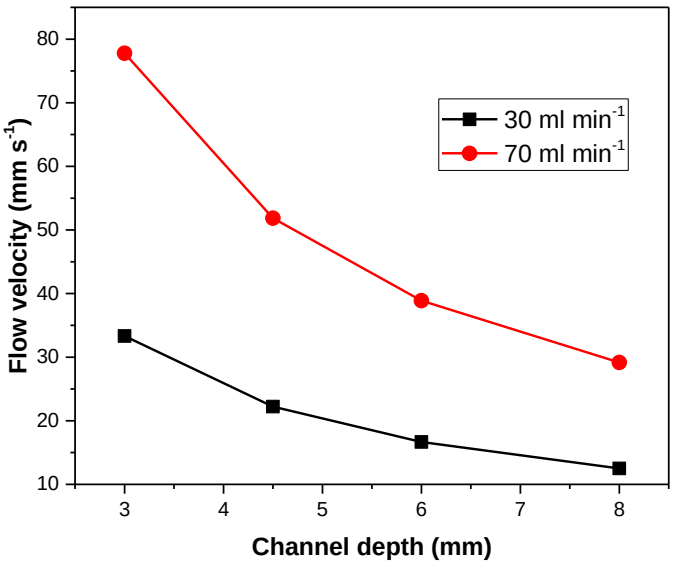

Figure 5.2. Flow velocity as a function of channel depth at volumetric feed rates of 30 ml min^{-1} and 70 ml min^{-1}.

5.5 Effect of Anode Channel Depth at Low Current Density

The effect of anode channel depth on the performance of the single-channel cell at various depths from 3.0 mm to 8.0 mm were tested, whereas the cathode channel depth was fixed at 3.0 mm. The experiments were conducted with water feed rate of 30 ml min^{-1} and at 80 °C and ambient pressure. Figure 5.3 shows the impedance spectra at a current density of 0.1 A cm^{-2}.

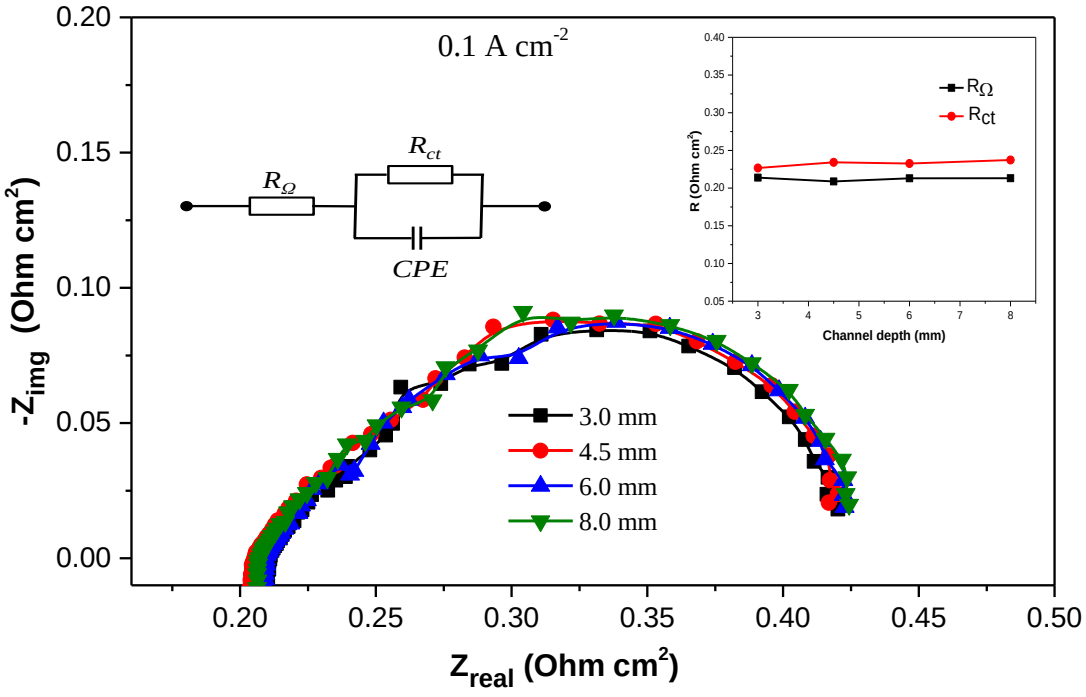

Figure 5.3. Impedance spectra showing the effect of channel depth on cell performance at a low current density of 0.1 A cm^{-2}. Inset show the plot of R_{Ω}, and R_{ct} and the equivalent circuit model.

The impedance spectra consist of a single semi-circular capacitive loop associated with charge transfer resistance. The plot shows a high-frequency inductive response usually attributed to the parasitic inductance in the system. The high-frequency intercept represents the ohmic resistance, R_{Ω} which includes the resistances of all the electrolyser components including the bipolar plate, PTLs, membrane and electrodes and their associated interfacial resistances. The diameter of the capacitive arc at low current densities represents the charge transfer resistance, R_{ct} of the OER at the anode, assuming that the charge transfer resistance at the cathode is relatively insignificant due to the faster kinetics of the hydrogen evolution reaction (HER). From Figure 5.3, both the R_{Ω} and R_{ct} were unchanged with an increase in channel depth, indicating that the ohmic resistance and the reaction kinetics were unaffected by the increase in channel depth.

5.6 Effect of Anode Channel Depth at Medium Current Density

Error! Reference source not found. shows the impedance spectra obtained at a medium current density of 0.5 A cm^{-2} and water feed rate of 30 ml min^{-1}. Compared to the data presented in Figure 5.3, the impedance spectra shows considerably smaller diameter arcs for all depths tested. Here, the diameter of the kinetic loop has decreased significantly as current density increased, which signifies the decrement of the charge transfer resistance. Specifically, the charge transfer resistance, R_{ct} decreased from 0.23 Ω cm^2 at 0.1 A cm^{-2} to 0.07 Ω cm^2 at 0.5 A cm^{-2}. Also simultaneously, as the current density increased, a mass transfer resistance, R_d is observed at low frequencies. However, this impedance was small and relatively unchanged at the various channel depth investigated.

In summary, results in Figure 5.3 and **Error! Reference source not found.** show that at low-to-medium current densities, change in channel depth shows negligible effect on cell performance, indicating that the primarily activation-controlled nature at low current densities and the primarily ohmic-controlled nature at medium current densities are unchanged by variation in the depth of the flow channel.

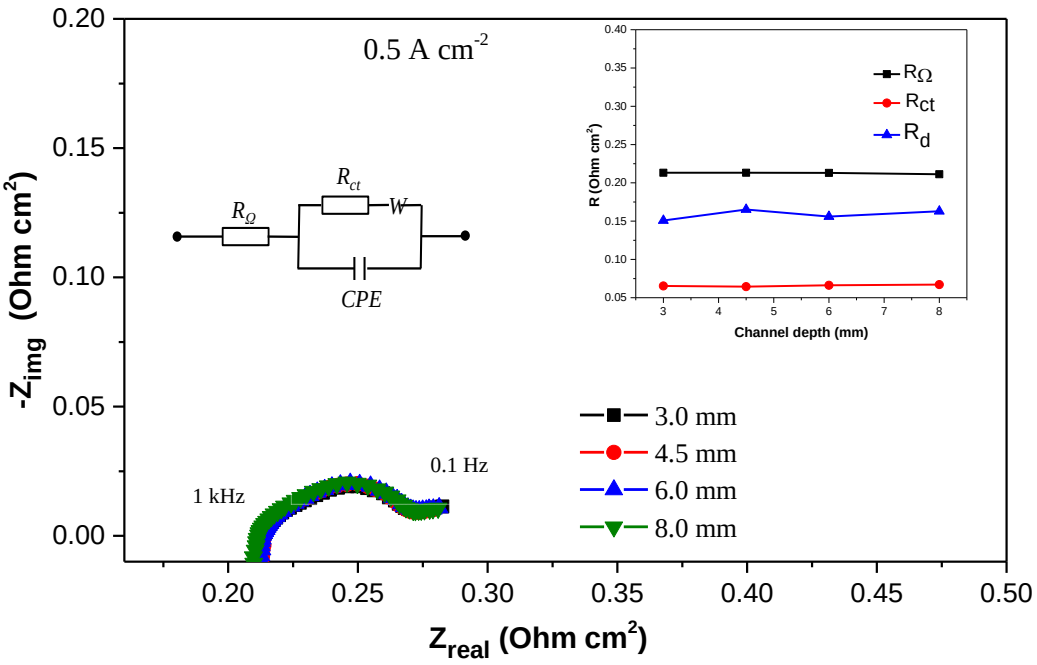

Figure 5.4. Impedance spectra showing the effect of channel depth on cell performance at a current density of 0.5 A cm^{-2}. Inset shows the plot of R_{Ω}, R_{ct} and R_d and the EC model.

5.7 Effect of Anode Channel Depth at High Current Densities

As the current density increased to 1.0 A cm^{-2}, shown in Figure 5.5, the spectra become mass transfer-dominated, seen as a second arc at low frequency. Furthermore, with the selected frequency annotated in Figure 5.5, it is evident that the second arc emanates from the low-frequency perturbation of the cell (i.e. 10 Hz – 0.1 Hz region). The low-frequency region probes slower processes and is normally associated with mass transport limitation. At this current density, there was significant variation in the size of the low-frequency arc with an increase in channel depth, which confirms the influence of channel depth on performance due to mass transport. The diameter of the low-frequency arc was lowest at 4.5 mm depth and highest at 3.0 mm depth. Therefore, a non-monotonic response of performance with an increase in channel depth was observed; with the maximum performance obtained at 4.5 mm channel depth and the others in the order 8.0 mm > 6.0 mm > 3.0 mm. An explanation for this observation will be discussed later.

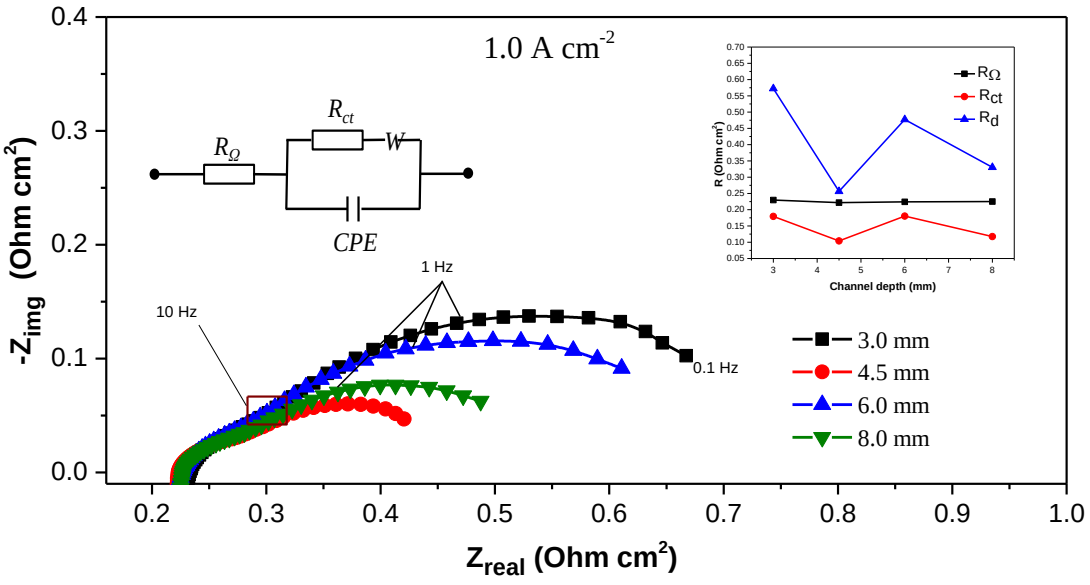

Figure 5.5. Impedance spectra showing the effect of channel depth on cell performance at a current density of 1.0 A cm^{-2}. Inset shows the plot of R_{Ω}, R_{ct} and R_d and the equivalent circuit model.

Figure 5.6 shows the impedance spectra at a current density of 2.0 A cm^{-2}. At this current density, it can be seen that the low-frequency arc has become bigger at all channel depths tested which is attributed to increased mass transport limitation. On the other hand, the high-frequency resistance and charge transfer resistance, though significantly reduced, are similar for all channel depths. At this current density, similar to the trend at 1.0 A cm^{-2}, the cell performance shows a non-monotonic dependency on variation in channel depth. The shallowest channel depth showed the worst performance, as was the case at a current density of 1.0 A cm^{-2}, which might be due to the dominance of gas slugs in the channel at this depth. The maximum performance at this current density was obtained for the 6.0 mm channel depth with the 4.5 mm and 8.0 mm depth showing slightly worse performance in that order. However, the magnitude of change in performance among the deeper channels was small.

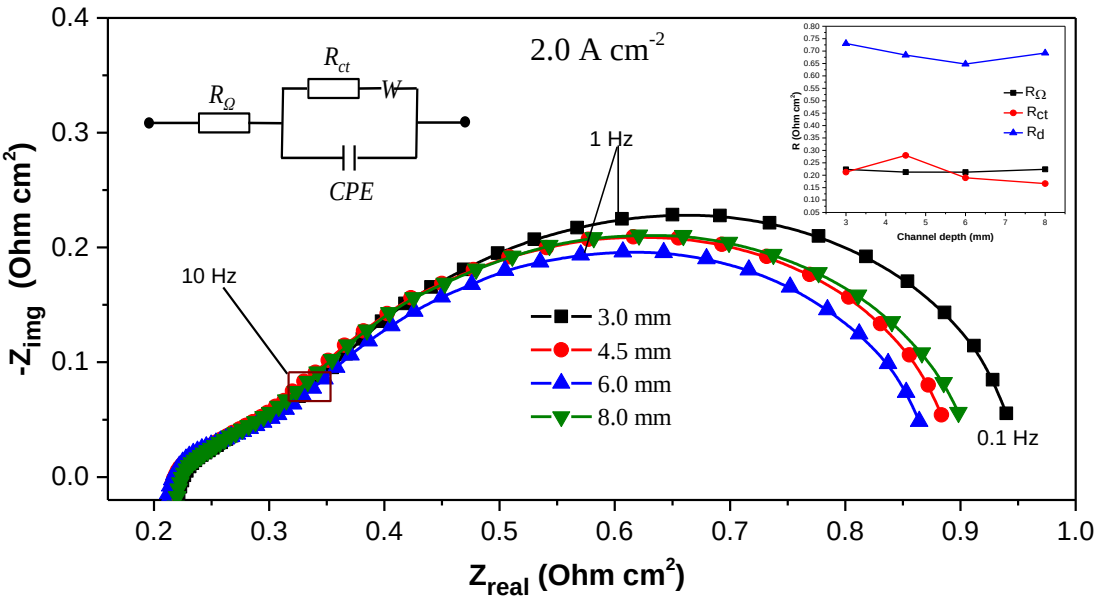

Figure 5.6. Impedance spectra showing the effect of channel depth on cell performance at a current density of 2.0 A cm^{-2}. Inset shows the plot of R_{Ω}, R_{ct} and R_d and the EC model.

This study suggests that this non-monotonic dependence of channel depth on performance observed at high current density can be attributed to the combined impact of flow velocity and mass transfer characteristics produced when channel

depth is varied. At a specified volumetric feed rate, increase in channel depth leads to decrease in the linear velocity of the liquid water (Figure 5.2) which could slow down the detachment and removal of the gas bubbles and slugs from the channel thus increasing the risk of water starvation at the catalyst active site. Therefore, at low velocities and high current densities, oxygen gas occupying the flow channel might block water access to the PTL and the active sites. On the other hand, increasing channel depth increases the effective mass transfer area between the incoming liquid water and the surface of the PTL and facilitates better bubble management, therefore, promoting efficient transport of water to the MEA. Due to the opposing nature of these effects, it is possible that, depending on the operating conditions, one might dominate the other or they might offset each other completely. Therefore, it is hypothesized that the combined effect of flow velocity and bubble/slug transport and removal could present a complex and non-monotonic variation of performance with depth seen under the conditions investigated in this study. However, the reasoning provided in this work is largely qualitative. It would be difficult to estimate the contributions of each phenomenon quantitatively.

Based on this explanation, the effect of flow velocity on the cell performance was investigated. The theoretical flow velocities were kept at a constant value regardless of the anode channel depth by adjusting individual feed rates; that is, feed rates of 20, 30, 40 and 53 ml min^{-1} for channel depth of 3.0, 4.5, 6.0 and 8.0 mm, respectively. This feed rate adjustment gives a resulting flow velocity value of 2.2 cm s^{-1} for all the channels. The cell was operated at 80°C and ambient pressure at a current density of 1.0 A cm^{-2}. The corresponding cell performance is presented in Figure 5.7.

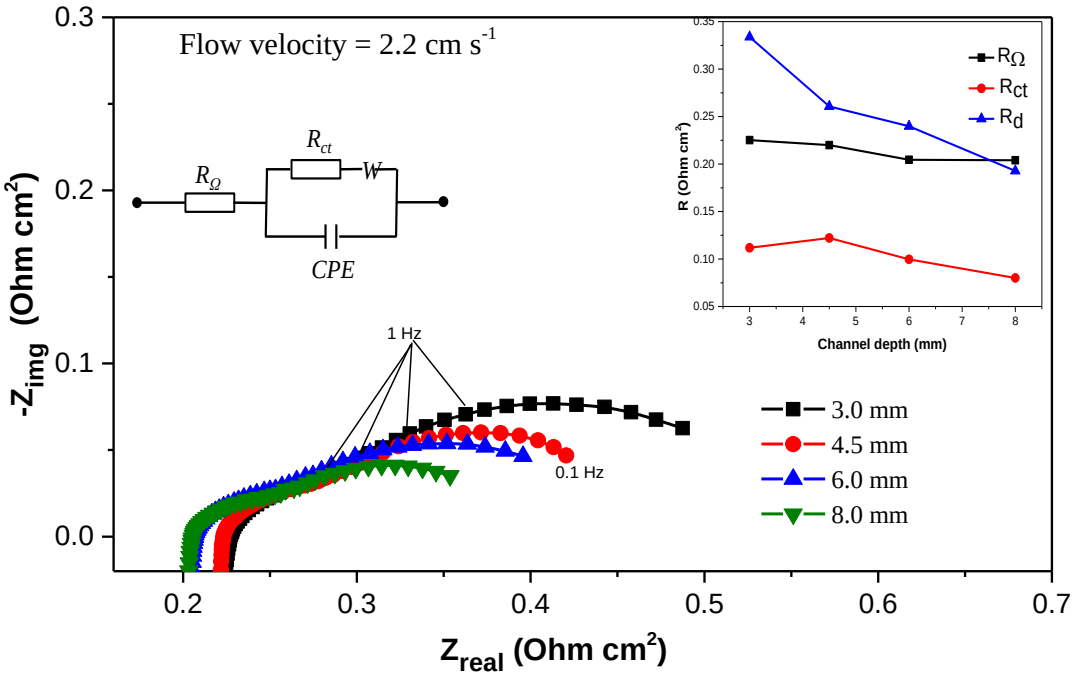

Figure 5.7. Impedance spectra showing the effect of channel depth on cell performance at a constant flow velocity of 2.2 cm s^{-1} and a current density of 1.0 A cm^{-2}.

It can be seen that the diameter of the impedance spectra decreased monotonically with increase in channel depth, which suggests that the observed variation in performance with anode channel depth cannot be explained by flow velocity alone. We suggest that the difference in performance at similar flow velocity can be attributed to the gas bubble management in the cell at various channel depths. It is worth noting that, from the inset in Figure 5.7, the variation in performance at the constant water flow velocity condition is non-linear. A possible explanation is that the complex interplay of surface tension, buoyancy, flow-induced shear, bubble coalescence, cooling effect with increased water flow and even the increase in flow velocity with the presence of bubbles in the channel could create a non-linear dependency of mass transfer on performance.

5.8 Effect of Channel Depth-to-Width Ratio on Two-Phase formation

The results presented in this chapter show the effect of channel depth on performance and indicate that there exists an optimal channel depth for the same

channel width when water is supplied to the cell; either shallower or deeper channels will lead to a reduced cell performance. Visual inspection of two-phase flow (not presented here) shows that the bubbles move outward away from the PTL layer towards the surface of the channel enclosure, with the two-phase flow separating into two layers, a bubble regime at the top, and a stream of water flow below in the area closer to the surface of the PTL. This improved access of water to the PTL surface might further explain the improvement in performance in deeper channels.

Although these experiments have been performed at constant channel width, it is expected that the channel depth-to-width ratio will impact the bubble evolution and two-phase flow dynamics in the cell, and hence overall performance. A wider channel for instance might influence the two-phase flow bubbly-to-slug transition by delaying formation of slugs in the channel.

5.9 Conclusion

In this Chapter, the effect of anode channel depth on the performance of a PEMWE has been investigated using electrochemical impedance spectroscopy. The impedance results revealed that the cell performance was invariant with channel depth at low and medium current densities, which indicate that the activation-controlled nature at low current densities and the ohmic-controlled nature at medium current densities are unchanged by variation in the depth of the flow channel. However, a non-monotonic variation in cell performance was observed at high current densities, which is attributed to the opposing impact of flow velocity and mass transfer characteristics produced with varying channel depth. Therefore, the obtained results have demonstrated for the first time in literature that modifying the anode channel depth might bring into play different factors which combine to determine cell performance.

Chapter 6

Effect of Porous Transport Layer Microstructure on Performance of PEMWE

Sections of this work have been peer reviewed and published in the International Journal of Hydrogen Energy (J. O. Majasan, F. Iacoviello, J.I.S Cho, M. Maier, X. Lu, T.P Neville, I. Dedigama, P. R. Shearing, and D. J. L Brett, "Correlative study of microstructure and performance for porous transport layers in polymer electrolyte membrane water electrolysers by X-ray computed tomography and electrochemical characterization," *Int. J. Hydrogen Energy*, vol. 44, no. 36, pp. 19519–19532, 2019) [168].

6.1 Introduction

The PTL, positioned between the MEA and the bipolar plates at both electrode sides, is a key component of the PEMWE, responsible for mass transport of liquid and gas between the electrodes and the flow channels, as well as electrical and heat conduction in the cell. These functions of the PTL require high liquid permeability and gas diffusivity of the pore phase and high electrical and thermal conductivity of the solid phase.

In ideal operation, the PTL contributes minimally to ohmic, interfacial, thermal and mass transport losses, such that the liquid water is fed to the electrode and the product gas is expelled from the catalytic layer through the PTL unhindered. However, the build-up of oxygen gas in the form of bubbles (gas voids) in the vicinity of the anode can reduce the available active area for reaction and gas

bubbles trapped in the pores of the PTL could hinder the mass transport of liquid water to the electrode. Therefore, the PTL plays a key role in determining the performance of PEMWEs.

The PTL is characterized by its morphology and structural parameters, such as powder size, porosity, pore size distribution, tortuosity, permeability, thickness, and pore size. It is, therefore, necessary to understand the effect of the structural properties and achieve a tailored pore morphology that optimizes electron, heat and mass transport across the porous structure.

Carbon materials (carbon paper and cloth) which are typically used as cathode and anode PTLs in PEM fuel cells are unsuitable for use in PEM electrolyser anodes due to the high operating potential, which corrodes carbon materials. Thus, the most widely used anode PTLs in PEMWEs are titanium (Ti)-based materials, such as sintered titanium powders, felt type titanium fibre, expanded sheets and titanium foam [56]–[60], [117].

Several studies have reported that the performance of PEMWEs is influenced by structural parameters of the anode PTL, such as powder size, thickness, porosity and pore size [51], [56]–[60], [75], [169]–[173]. Grigoriev *et al.* [57] were the first to investigate sintered powder PTLs in PEM electrolysers experimentally and suggested that an optimal mean pore diameter (MPD) of 12-13 μm, optimal porosity in the 30-50% range and optimal powder size in the range 50-75 μm for Ti sintered powder PTLs. These values were proposed as a compromise between capillary effects, which manifest at pore sizes below 10 μm, and parasitic ohmic losses associated with large pore sizes. Hwang *et al.* [58] investigated the effect of fibre size, MPD and porosity on performance using titanium felt PTLs in a unitized reversible fuel cell operating in electrolysis mode. They reported a poorer performance with an increase in MPD and fibre size and further suggested that the MPD, rather than porosity, is the more crucial parameter for electrolysis performance. Similar results for felt-type PTLs were reported by Ito *et al.* [59] as they also observed that the electrolyser performance deteriorated with increasing MPD when the MPD was larger than 10 μm. They pointed out that for porosity greater than 50%, further increase in porosity had no significant effect on

performance. In another study, Ito *et al.* [56], suggested that the oxygen bubbles produced at the anode may block the PTL when the MPD is less than 50 μm.

Other attempts at PTL improvement have introduced microporous layers (MPLs) analogous to those associated with improved performance in PEMFCs [174]–[177]. For example, Hwang *et al.* [172] investigated the integration of a backing or microporous layer by loading a Ti felt with Ti powder. Lettenmeier *et al.* [178] reported performance improvement at high current densities with MPL integration. The effect of transport properties such as thermal conductivity, electrical conductivity and permeability have been investigated recently by Zielke *et al.* [126] using micro-computed tomography. The authors reported an exponential relationship between the PTL porosity and thermal conductivity and also between the in-plane electrical conductivity and water permeability. More recently, Mo *et al.* [131], [179]–[181] investigated PTLs with controlled morphologies, by using thin/tunable PTLs having a planar surface with straight-through pores and reported promising results compared to the current state-of-the-art.

Thus, the importance of the anode PTL design is highlighted by a clear relationship between PTL microstructural properties and PEMWE performance. However, the structure-performance relationship is not yet fully understood, especially how the microstructural properties influence ohmic and mass transport losses in the PEMWE at high current densities.

In this Chapter, four commercial sintered titanium powder PTLs with distinctive mean pore sizes are characterized ex-situ by scanning electron microscopy and X-ray computed micro-tomography for properties such as surface morphology, porosity, pore size distribution, porosity distribution and tortuosity. Then, the microstructural properties are correlated with electrochemical performance based on polarization curves and electrochemical impedance spectroscopy at current densities up to 3.0 A cm^{-2}.

6.2 Materials and Methods

6.2.1 PTL Samples

Four commercially available sintered titanium powder PTLs purchased from Baoji Qixin Titanium Co, Ltd are used for this study; the technical data supplied by the manufacturer is summarized in Table 6.1. The PTL samples were coated with a 0.5 μm platinum layer to provide corrosion resistance for high current density use. The samples are labelled as PD16, PD40, PD60 and PD90 where "PD" refers to "pore diameter" and the two-digit number that follows is the manufacturer-supplied values of the mean pore diameter in μm. The mean pore diameter of the PTL is a key microstructural characteristic expected to influence performance [56]–[59], [172]. According to the data, the PD90 sample has a mean pore diameter roughly six times that of PD16; therefore, this provides a wide range of pore diameter to investigate how PTL structure can affect electrolyser performance. As shown in Table 6.1, the PTLs have similar thicknesses of ca.1 mm and the powder size is in the range of 150-1000 μm.

Table 6.1. Properties of investigated PTLs.

PTL sample	Mean pore diameter (μm)	Thickness (mm)	Particle size (μm)
PD16	16	1.00	150-250
PD40	40	1.00	270-380
PD60	60	1.09	380-830
PD90	90	1.04	380-1000

6.2.2 Ex-situ Morphology and Microstructural Characterisation

6.2.2.1 SEM Analysis

The surface morphology of the PTL samples was examined using scanning electron microscopy (SEM, Zeiss EVO MA10, Carl Zeiss, USA). A 5 mm diameter disc of each PTL sample was used for imaging. High-resolution images were obtained at an electron accelerating voltage of 10 kV on secondary electron imaging mode at a

working distance range of 8-8.5 mm. Images of the surface structure of the samples were captured and collected using the built-in SmartSEM® image acquisition and processing software.

6.2.2.2 X-ray Computed Tomography Image Acquisition

X-ray computed micro-tomography is a powerful non-invasive, radiographic 3D imaging technique which allows both quantitative and qualitative investigation of the structure and properties of various materials non-destructively [141], [142], [169]. It involves directing an X-ray beam towards the sample, while rotating the sample on a rotation stage about an axis perpendicular to the incident X-ray beam. The X-rays pass through the sample to create 2D radiographs which reflects the density and compositional variation at various points within the sample. The series of 2D radiographs are then reconstructed into a 3D volume using mathematical transformation algorithms [182] from which tomograms, comprising of 3D elements called voxels (extension of the term pixel in 2D imaging) are extracted. These 3D data are then analysed using dedicated software packages to obtain 3D quantitative information about the sample structure.

In this study, investigation of the microstructure of the PTL samples was performed by X-ray computed micro-tomography (ZEISS Xradia Versa 520, Carl Zeiss X-ray Microscopy Inc., Pleasanton, CA). All samples were scanned in pristine state and the scans were carried out with a source voltage of 150 kV with exposure time of 4 s per projection, acquiring 1801 projections per scan. Images from the scan were reconstructed using Zeiss XMReconstructor software, which uses a cone-beam filtered back-projection algorithm, resulting in a voxel volume of approximately 1.01 μm. A sub-volume of 800^3 voxels was extracted from each 3D volume to minimize computational requirements. An edge-preserving non-local means filter was applied to each dataset to reduce noise and aid phase segmentation. Segmentation of the solid and pore phases and 3D volume rendering of the resulting reconstructed volumes was performed using the Avizo software package (version 9.2. FEI, VSG). Manual thresholding of the 3D volume was chosen due to the good image contrast between the solid and pore phases, largely due to the disparate X-ray attenuation coefficients of titanium and air. Grey-scale and binary ortho-slices of each sample and 3D TIFF image files were generated. The

segmented 3D TIFF image files were then processed for image-based quantification. The pore size distribution was obtained using commercial software (ImageJ 1.31v). The porosity distribution was obtained using pore quantification code implemented in MATLAB [159]. The bulk porosity and tortuosity factor was obtained using the *TauFactor* software plug-in for MATLAB [148] based on a uniform shrink representative volume analysis.

6.2.3 Electrochemical Characterisation

Electrochemical characterisation was performed using a Gamry Reference 3000 galvanostat/potentiostat equipped with a Gamry 30k Booster (Gamry Instruments, USA). All electrochemical characterization data was acquired using the Gamry Framework software (version 6.24).

In the steady state current-voltage polarization curves (*i-V* curves), the current density was increased from 0 A cm^{-2} to 3.0 A cm^{-2} in 0.1 A increments. Initial steady-state operation was ensured before recording a polarization curve by applying an initial load of 1.0 A cm^{-2} to the cell for 15 minutes, during which a constant potential was attained, indicating the stability of the electrode. In addition to randomising the order of the experiments, the polarization curves were generated in triplicates for each PTL tested and were highly reproducible (standard deviation <3%). The reported results are the averages of the three polarization curves generated.

Electrochemical impedance spectroscopy (EIS) was performed at current densities of 0.1, 0.5 and 3.0 A cm^{-2} between 100 kHz and 0.1 Hz, with each test preceded by a conditioning period of 15 minutes at the respective current density to ensure steady-state operation. A variable AC perturbation of 5% of the DC value was applied which was confirmed to be small enough not to interfere with the cell performance. The anode served as the working electrode, whereas the cathode was utilized as both counter and reference. Impedance measurements were also done in triplicates for each test condition and were highly reproducible (standard deviation <0.5%). Impedance data have been displayed using the complex plane (Nyquist plot), and parameters were extracted from the impedance curves by fitting the

experimental data to an equivalent circuit using Zview software (Scribner Associates, Inc., v3.3d).

6.3 Results

6.3.1 Surface Morphology of PTL Samples by Scanning Electron Microscopy

The surface morphology of the PTLs was characterized using SEM. Figure 6.1 presents the top-view micrographs of the PTLs obtained at 200× magnification. The SEM micrographs demonstrate significant differences in pore sizes across the four PTL samples consistent with the intended pore size variability for the study. PD16 and PD40 show a relatively small micro-pore structure, whereas PD60 and PD90 show an open large macro-pore structure. The shape and size of the pores in the PTL samples was irregular, attributed to the agglomeration of titanium powder to form clusters during the sintering process. In addition, several closed micropores can be observed on the surface of the PTLs, particularly of the larger pore PTLs. In a typical PEMWE configuration (Figure 2.1), the PTL is pressed directly against the electrode catalyst layer, and as the average pore size of the catalyst layer is about 10-200 nm [183], [184] (one to two orders of magnitudes smaller than the average pore size of the PTL), it is estimated that the highly open macro-pore structure of the larger pore PTL samples, for instance PD60 and PD90 samples, would lead to a decrease in the number of PTL/catalyst layer connection per unit MEA area, and thus result in an increased interfacial contact resistance between the PTL/catalyst layer and the PTL/flow-field plate. This claim is verified later in this work.

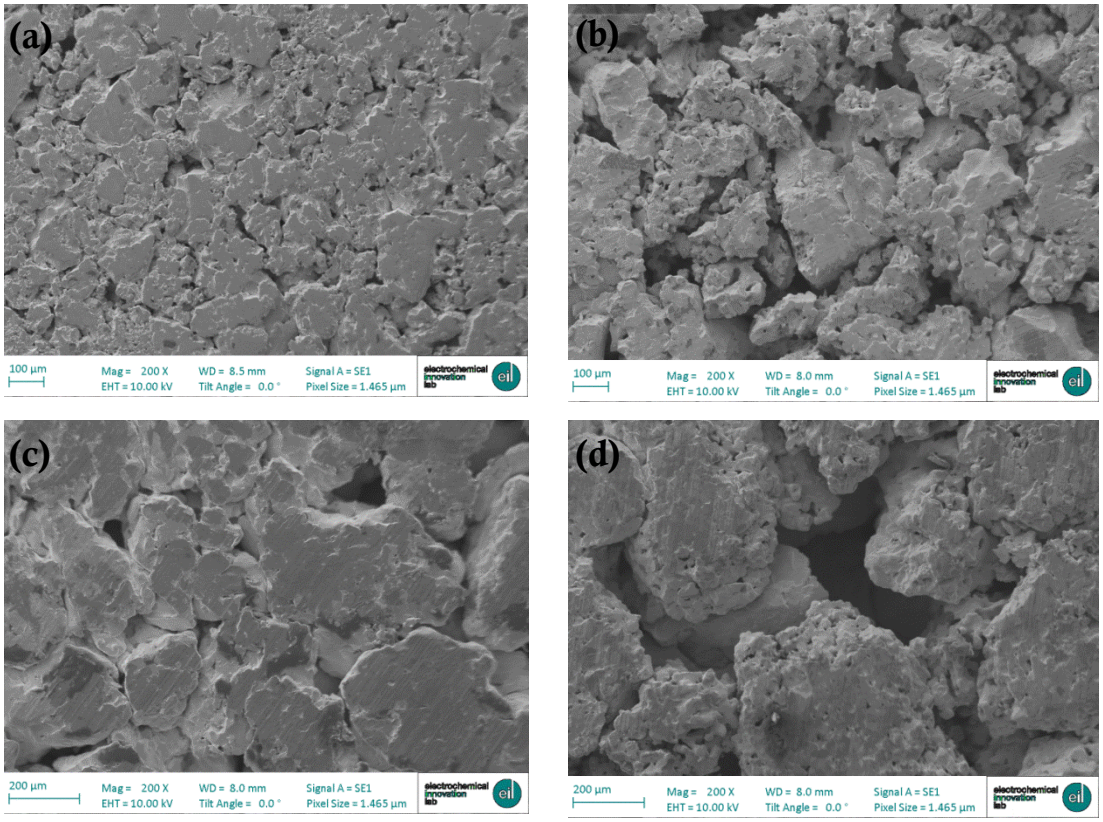

Figure 6.1. Micrographs of the PTLs (200× magnification). (a) PD16 sample, (b) PD40 sample, (c) PD60 sample, and (d) PD90 sample.

6.3.2 3D Reconstruction, Pore Size Distribution, Porosity Distribution and Tortuosity Analysis

The differences between samples in pore size and microstructure were further detected by X-ray computed tomography and the segmented images are presented in Figure 6.2. The binary images of the reconstructed tomograms show the highly X-ray-attenuating solid titanium in white and the less-attenuating pore spaces in black. From Figure 6.2, the variation in pore sizes can be identified visually. It is also possible to notice that the PD90 contains bigger pores and a wider pore size variation than the other samples. The PD16 sample shows a larger cross-sectional pore count, albeit with comparatively smaller-sized pores, while on the other hand, as the mean pore size increases, the cross-sectional number of pores and solid cluster decreased significantly.

The three-dimensional volume renderings of the PTL samples are shown in Figure 6.3. The reconstructed 3D tomograms further reveal the variation in porous structure of the PTLs. A well-connected network of pores is apparent that offers a variety of continuous pathways through the solid structure. To further visualize the complementary pore spaces, the middle images (in green) show the connected pore network and also indicate the presence of isolated pores in the structures. Isolated pores are generally unavailable to fluid transport and might influence the performance of the PTLs.

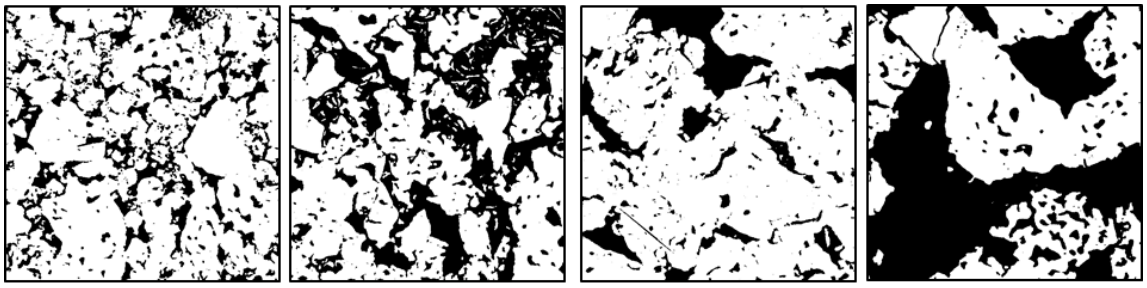

Figure 6.2. Binarized tomography ortho slices corresponding to (a) PD16, (b) PD40, (c) PD60, and (d) PD90. The pores are shown in black and the solid phase in white.

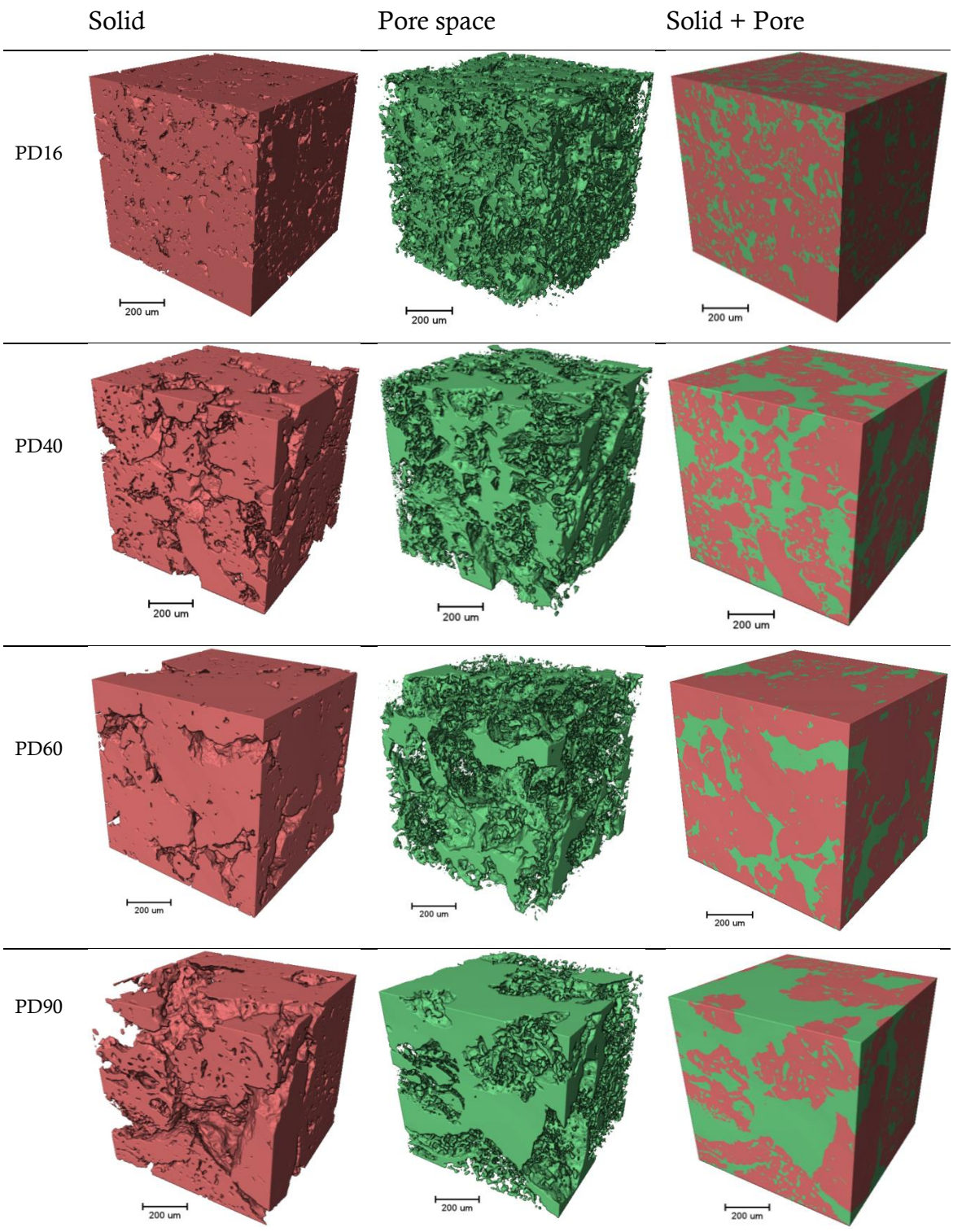

Figure 6.3. 3D volume renderings of the PTL samples. (a) PD16 (b) PD40 (c) PD60 (d) PD90. Each cube is an extracted 800^3 volume with the solid phase in red and pore space in green.

The pore size distribution and the corresponding cumulative frequencies (on the basis of pore volume) for the PTL samples are shown in Figure 6.4. It is evident that the distribution becomes broader with increasing powder size/MPD, with the PD90 sample exhibiting a range of pore sizes an order of magnitude larger than that of the PD16. Although pore sizes as small as 1 μm were observed in all the samples, the maximum pore diameter was 46 μm in PD16 compared to 263 μm in PD90. Also, a greater variability of pore distribution in the larger MPD samples was apparent. For example, PD16 shows a narrow band of pore sizes, where pores with diameter ≤18 μm constitute about 80% of pores; whereas broader bands of pore sizes are seen for larger MPDs. PD90, for instance, shows an apparent multimodality where at least two distinct pore clusters can be observed with 40% of pores having a diameter ≤50 μm, and another peak between 70 and 110 μm representing another 40% of the total pore volume. It is suggested that PTLs with a larger pore size/pore volume could enhance mass transport, but at a cost of decreased electrical conductivity. Detailed quantification of pore size and pore volume fraction is summarized in Table 6.2.

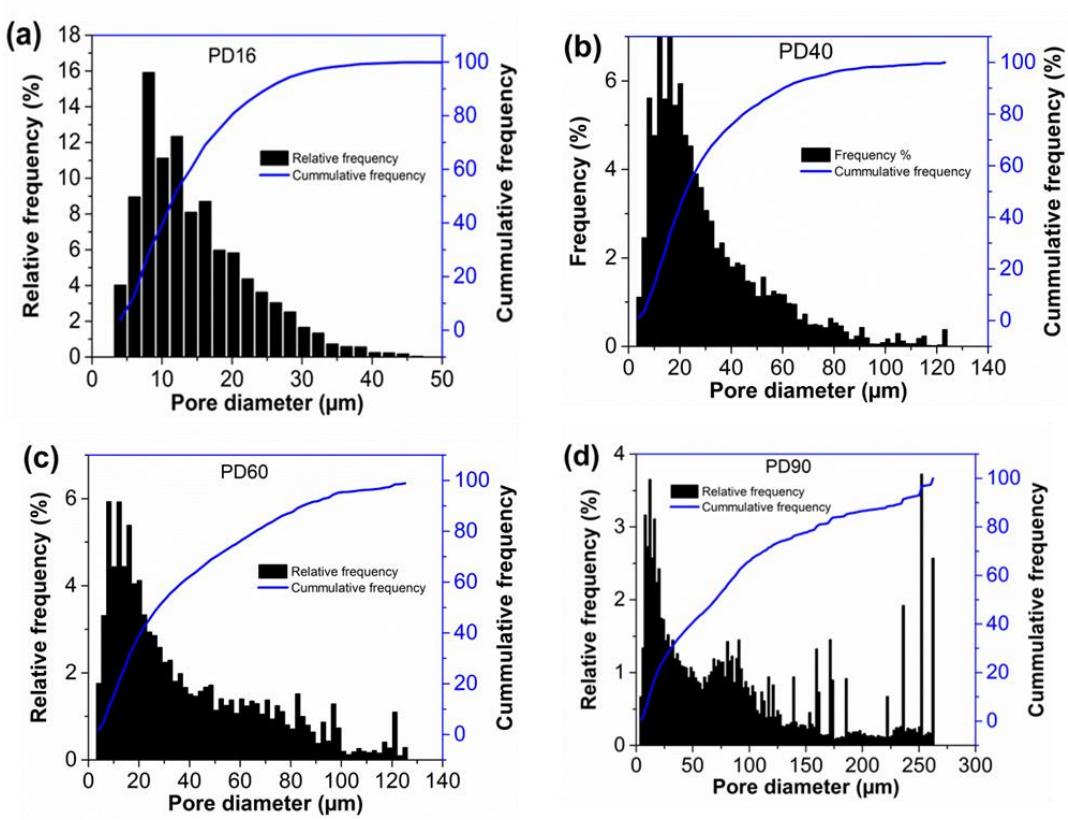

Figure 6.4. Pore size distribution in (a) PD16, (b) PD40, (c) PD60, and (d) PD90.

Table 6.2. Quantitative analysis of pore size distribution of PTLs from X-ray computed tomography.

	PD16	PD40	PD60	PD90
Pore volume fraction	21.84	35.56	20.39	37.83
Mean Pore diameter (μm)	14.66	30.28	38.00	90.96
Maximum pore diameter (μm)	45.51	123.16	125.18	262.47

To assess the directional uniformity of the pores in the PTL structure, the slice-by-slice porosity distribution was investigated from the reconstructed 3D volume. Each slice was limited to the spatial (slice) resolution which was ~1.01 μm for all the PTL samples. The areal porosity in the *x-y* plane along the PTL thickness was analysed and presented in Figure 6.5(a). Fluctuation of porosity along the PTL thickness is observed, which was unsurprising due to the apparent random structure of the PTLs. As can be seen from Figure 6.5(b), higher standard deviation values are obtained at larger mean pore diameter of the PTLs, which indicates higher heterogeneity in the PTL porous structure with increase in mean pore size. Figure 6.5(b) also shows the average fraction of the porosity distribution. The average areal porosity fraction of PTLs was 21.84%, 35.56%, 20.39% and 37.83% respectively. In general, the average areal porosity was higher for larger pore PTLs. However, PD60 shows an unexpectedly low average areal porosity which is attributed to the powder packing during manufacturing which might suggest that the porosity does not scale directly with the powder size but is also influenced by the powder packing during the manufacturing process.

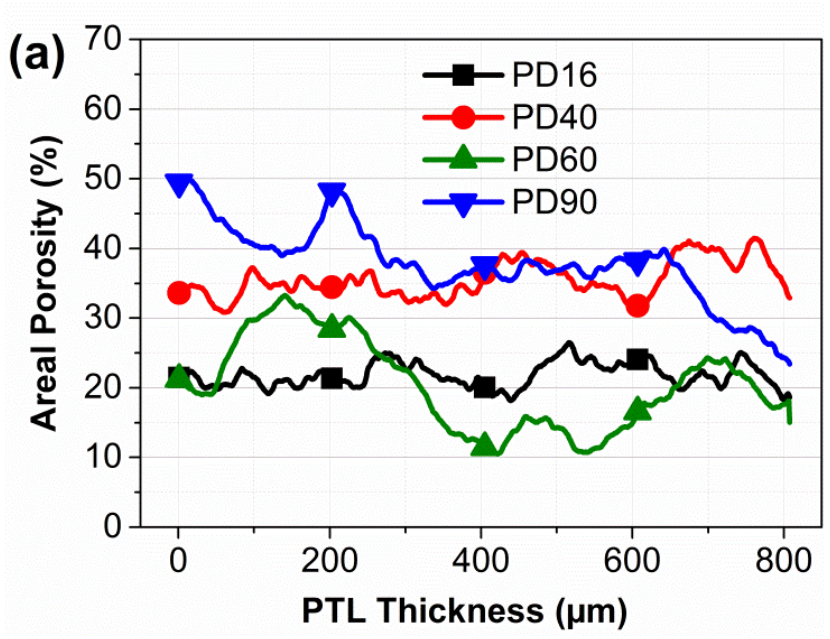
(a)
PD16
PD40
PD60
PD90
Areal Porosity (%)
PTL Thickness (μm)
0
10
20
30
40
50
60
70
0
200
400
600
800

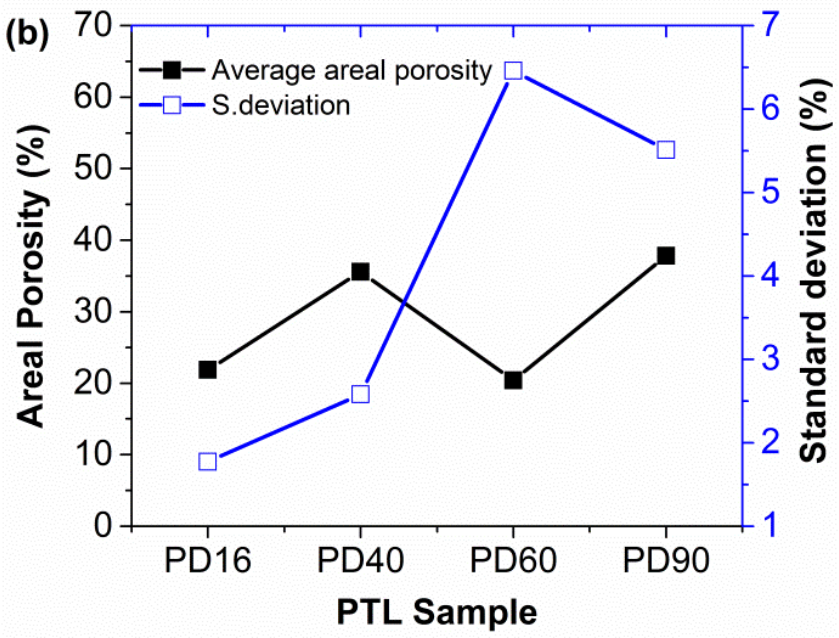
(b)
Average areal porosity
S.deviation
Areal Porosity (%)
Standard deviation (%)
PTL Sample
PD16
PD40
PD60
PD90
0
10
20
30
40
50
60
70
1
2
3
4
5
6
7

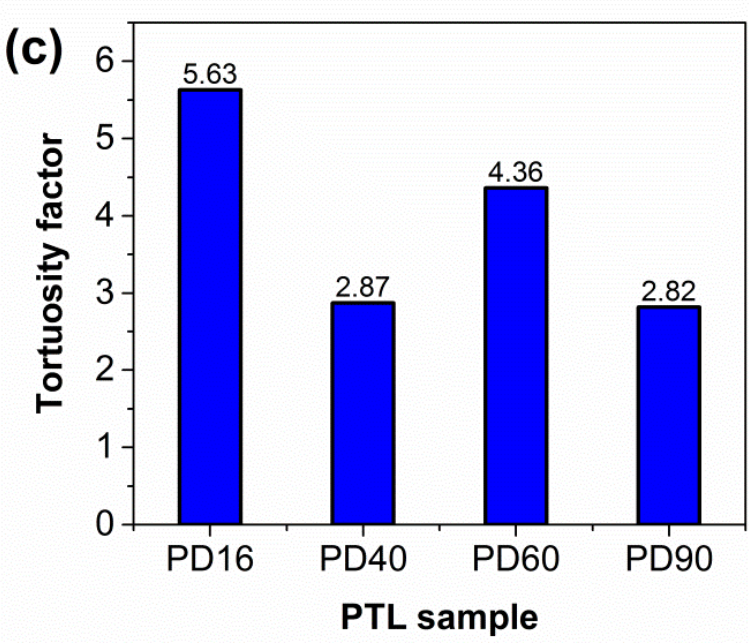

Figure 6.5. (a) Areal porosity distribution showing slice-by-slice porosity in the through-plane (thickness) direction for the PTL samples, (b) average value and standard deviation of porosity, (c) tortuosity factor for the PTLs in the *z*-direction (along the PTL thickness).

Figure 6.5(c) presents the tortuosity factor of the PTLs in the through-plane direction, which is a factor in determining the resistance to diffusive transport caused by convolutions in the flow paths [185]. The values obtained for the tortuosity factors are 5.63, 2.87, 4.36 and 2.82 for PD16, PD40, PD60 and PD90, respectively. This suggest PD16 has the most tortuous flow path of the PTLs with the PD90 being the least tortuous. The tortuosity was unexpectedly higher in PD60; however, this is consistent with the observations presented in Figure 6.3 and Figure 6.5(a) and (b), which show the lower porosity and more closed structure of this particular sample. The samples with higher porosity (PD40 and PD90) also show a low tortuosity factor while the low porosity samples (PD16 and PD60) show a high tortuosity. This is the first time this relationship has been observed in titanium sinter used for PEMWEs; however, this inverse relationship between porosity and tortuosity has been invoked when analysing transport phenomena in electrochemical systems [186]. The quantification of tortuosity is relevant to performance due to the dependency of permeability and effective diffusivity and

hence, mass transport on tortuosity. It is expected that increasing the tortuosity factor of the PTL would be unfavourable for mass transport and contribute to mass transport resistance due to reduced effective gas/liquid diffusion.

6.3.3 Polarization Behaviour of the PEMWE with Various PTLs

In this section, the electrochemical performance of the various PTLs is investigated. The steady-state polarization performance of the four PTL samples was studied at a water feed rate of 15 ml min^{-1} (Figure 6.6). The measurements were performed at a feed water temperature of 80 °C and ambient pressure. All operating parameters and PEMWE components were kept the same between cell assemblies with only the PTL varied. As seen in Figure 6.6(a), PD16 shows the best performance (lowest cell potential at given current density) of the four PTLs at both water feed rates and the performance decreased monotonically in the order PD16 > PD40 > PD60 > PD90. For instance, at 15 ml min^{-1} and a current density of 3.0 A cm^{-2}, the cell potential was 2.54 V in PD16, 2.64 V in PD40, 2.65 V in PD60 and 2.74 V in PD90. The cell performance was similar for all four PTLs at low current density. However as current density increased, the influence of the PTLs became apparent. The difference in cell performance observed is attributed to the difference in the PTL microstructure since the same MEA and cell fixtures were used under the same test conditions with the only change being the PTL. Notably, the order of performance of the PEMWE with the various PTLs was consistent with the MPD of the PTLs at both water feed rates. Considering this, the correlation of MPD and cell performance was tested. As can be seen from Figure 6.6(b), a strong linear correlation ($R^2 \approx 0.93$) is evident. This apparent strong correlation of MPD with performance supports previous findings by other researchers [57]–[59].

Although the polarization curve provides a good qualification of overall cell performance, it does not lend itself readily to quantification of the individual overpotential effects. In the next section, electrochemical impedance spectroscopy is used to deconvolute the various voltage contributions [94], [129], [187], [188].

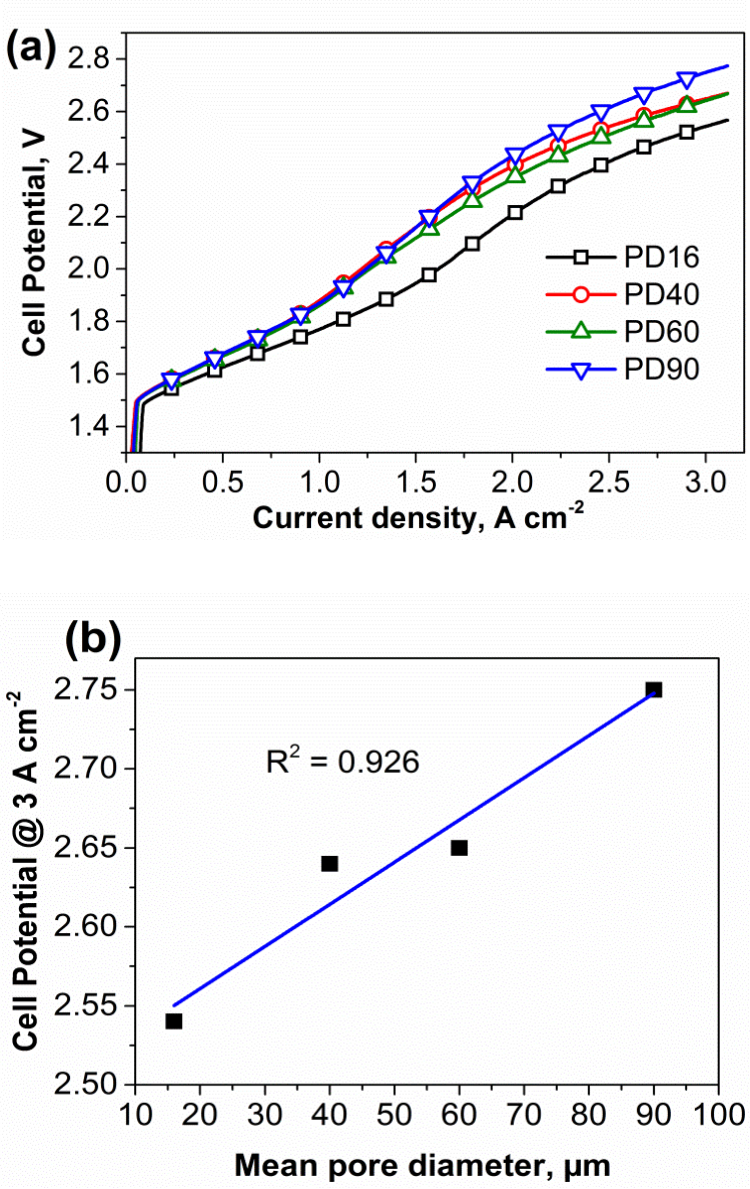

Figure 6.6. Polarization curves showing the performance of the four PTL at water feed rate of 15 ml min^{-1} and atmospheric pressure. (b) Correlation of mean pore diameter and cell potential at current density of 3.0 A cm^{-2}.

6.3.4 Impedance Spectroscopy of the PEMWE with Various PTLs

Electrochemical impedance spectroscopy was applied at 0.1, 0.5 and 3.0 A cm^{-2} to enable evaluation of the overpotentials at 'low', 'medium' and 'high' current densities, respectively. Figure 6.7 shows the impedance response of the PEMWE cell in a Nyquist plot representation, measured at the various current densities. The measurements were performed at 80 ºC, at atmospheric pressure and a volumetric water feed rate of 15 ml min^{-1}. It should be noted that for current densities of 0.5

and 3.0 A cm^{-2}, the high frequency intercept of the Nyquist plot were normalized to zero, for direct visual comparison of the impedance arcs.

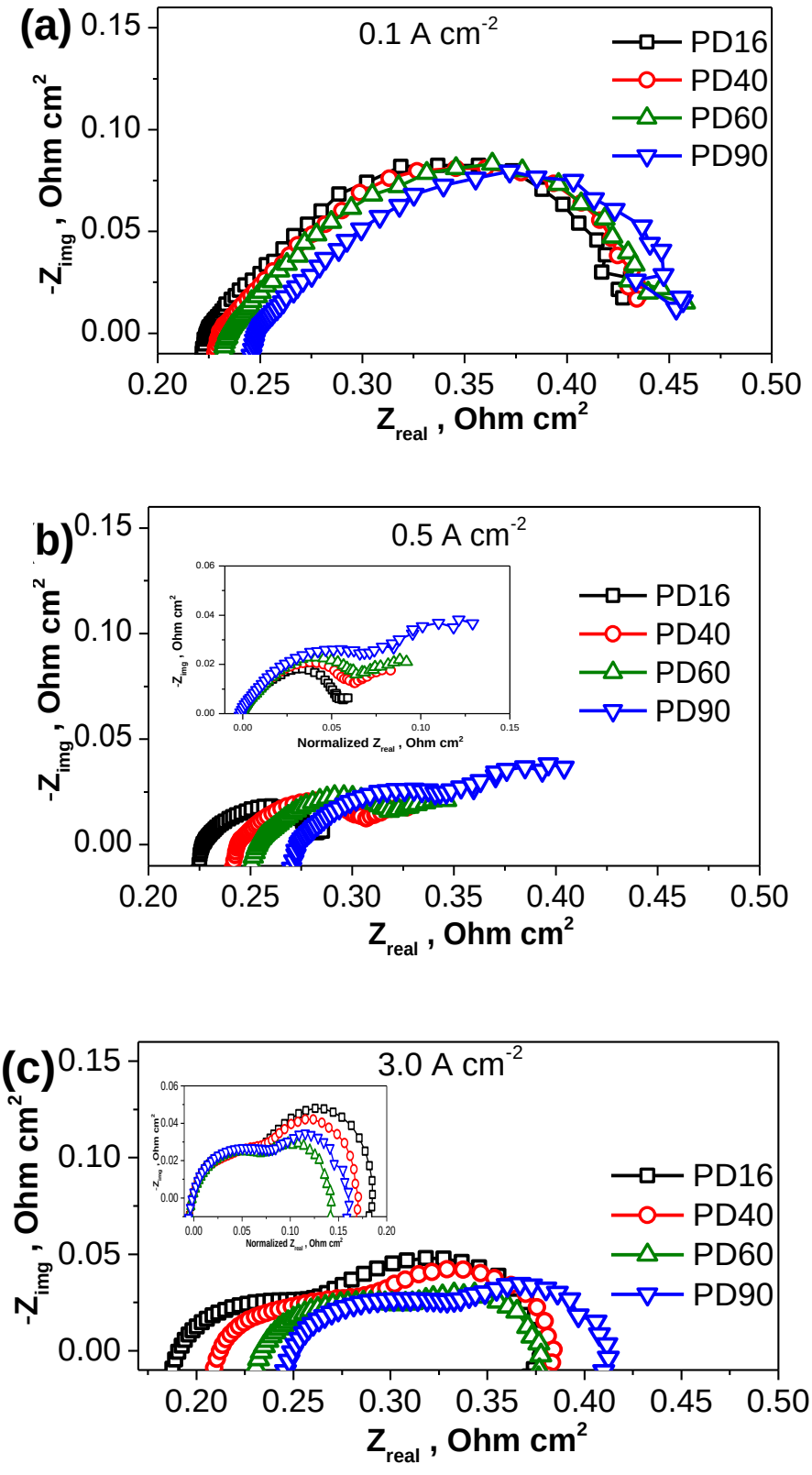

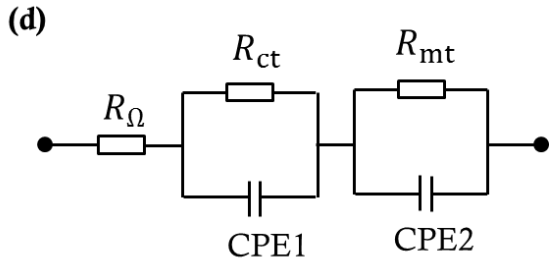

Figure 6.7. Nyquist plots showing the performance of the various PTLs at a water feed rate of 15 ml min^{-1} and a current density of (a) 0.1 A cm^{-2}, (b) 0.5 A cm^{-2}, (c) 3.0 A cm^{-2}. The insets show the same graph on a normalized *x*-axis for visual comparison. (d) Equivalent circuit for the electrolyser cell showing the ohmic, charge transfer resistances and mass transport resistances.

At current density of 0.1 A cm^{-2} (Figure 6.7a), the Nyquist plot consist of two main features: a single capacitive arc, the width of which primarily corresponds to the charge transfer resistance and an inductive response at high frequency attributed to the parasitic inductance present in the system [129]. At this current density, the Nyquist plots show a similar diameter for the capacitive arc of each PTL, suggesting negligible impact of the variation of PTL properties on the charge transfer resistance. However, the ohmic resistance, represented by the high frequency intercept with the real axis, varied and increased monotonically in the order PD16 < PD40 < PD60 < PD90; corresponding to the increase in the MPD and the trend in the polarization curve presented in Figure 6.6(a). The ohmic resistance comprises the bulk resistances of the membrane/PTL/bipolar plate resistance and their interfacial contact resistance. However, since the same PEMWE construction is used in all the cases, with the only change being the PTLs, the increase in ohmic resistance can be ascribed to the increase in mean pore diameter of the samples leading to increased interfacial contact resistance between the PTL surface and the electrode layer. This is explained by the fact that the electrons must move longer distances, on average, along the surface of the catalyst layer before a contact between the catalyst layer and the PTL is found in the case of the larger pore PTL. Thus, the ohmic resistance is lowest in PD16 and highest in PD90.

With increase in current density to 0.5 A cm^{-2} (Figure 6.7b), in addition to the charge transfer capacitive arc at high frequency, a second inchoate arc is seen at low frequencies. This is attributed to mass transport limitations [94], [178], [188], [189] and increases with larger mean pore diameter. One explanation is the positive influence of capillary-driven water transport, which is greater for smaller pore diameters. Further increase in current density to 3.0 A cm^{-2} results in an increase in the low frequency arc as seen in the inset in Figure 6.7(c). Here, the mass transfer arc for PD60 is the smallest and largest for PD16, indicating that at elevated current density, the mass transport resistance is highest in the PTL with the smallest average pore size. The size of the low frequency arc from the smallest to the largest was in the order PD60 < PD90 < PD40 < PD16. This shows a trend towards reduced mass transport limitation with increased pore size; however, the trend is non-monotonic, suggesting that there is an optimal pore size that minimises overall mass transfer limitations.

It is worth noting that a pseudo-inductive feature is observed at low frequency. Low-frequency pseudo-inductive loops are known to be caused by adsorption processed reactions with intermediate species such as the poisoning of PEM fuel cell anodes by carbon monoxide and water transport characteristics in the membrane [190]. However, the reason for it here at high current density is unclear but may be associated with a change in the macroscopic two-phase flow regime, which is known to influence local current density [94], [97].

6.3.5 Contributions of Individual Losses in the PEMWE Cell with Various PTLs

In order to evaluate the relative effect of the losses in the PEMWE cell, the various resistances were quantified by equivalent resistance analysis. The impedance spectra were fit to the equivalent circuit shown in Figure 6.7(d). The intercept with the real axis represent the ohmic resistance in the electrolyser cell and represented by a resistor (R_Ω). The high and low frequency arcs are attributed to the anode charge transfer and mass transport process in the PEMWE represented by ($R_{ct}CPE1$) and ($R_{mt}CPE2$) respectively. Constant phase elements (CPE) were used instead of pure capacitances to account for the porous nature of the electrode. The variation of the various resistances (ohmic R_Ω, charge transfer R_{ct}, and mass

transport R_{mt} resistances) for different current densities, obtained from the equivalent circuit model is presented in Figure 6.8. It can be noted that the ohmic resistance increased approximately linearly with increase in MPD, across all three current densities (Figure 6.8a). At 3.0 A cm^{-2}, the ohmic resistance increased from 0.19 Ω cm^2 in PD16 to 0.25 Ω cm^2 in PD90 confirming the higher ohmic resistance of the larger pore PTL. The charge transfer resistance, R_{ct}, decreased by about threefold from 0.22 Ω cm^2 to 0.07 Ω cm^2 as current density increased from 0.1 A cm^{-2} to 3.0 A cm^{-2} showing the faster activation and reaction kinetics at high current density. No major difference or clear trend in the charge transfer resistance with MPD (Figure 6.8b) was observed, indicating the PTL has no significant effect on the electro-catalysis in the electrode. As shown in Figure 6.8(c), mass transport resistance was observed at intermediate current density (0.5 A cm^{-2}) and at high current density (3.0 A cm^{-2}) but was higher, as expected, at high current density. Also, at the high current density, the mass transport resistance decreased with increasing MPD up to PD60 then increased at PD90 which suggests an optimal mean pore diameter beyond which mass transport resistance would increase. Overall, across the PTLs from PD16 to PD90, R_{Ω} increased by ~0.06 Ω cm^2 whereas R_{mt} decreased by ~0.04 Ω cm^2 at 3.0 A cm^{-2} and R_{ct} was relatively unchanged. Thus, a net increase in ohmic resistance suggests that the ohmic resistance is the overriding factor in determining cell performance over this current density range.

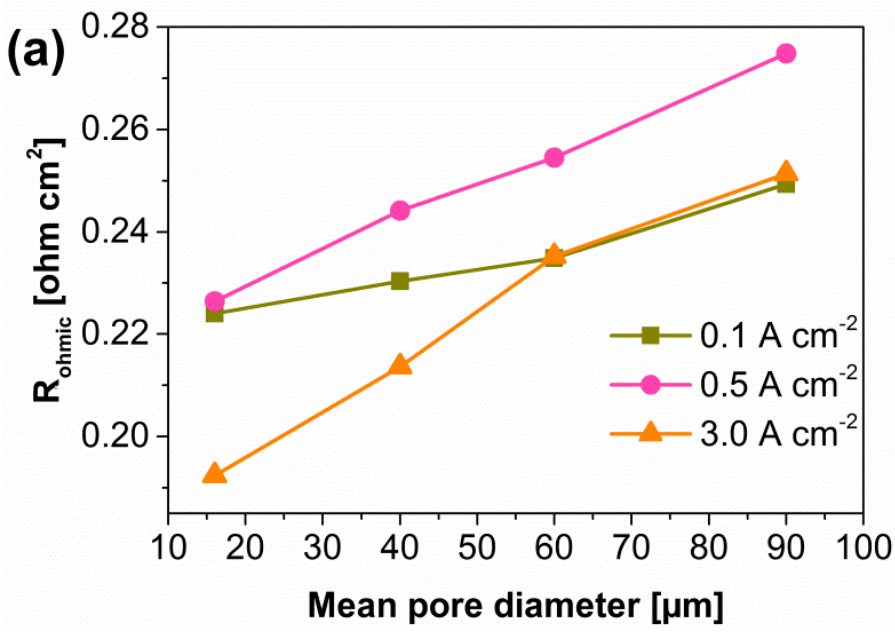

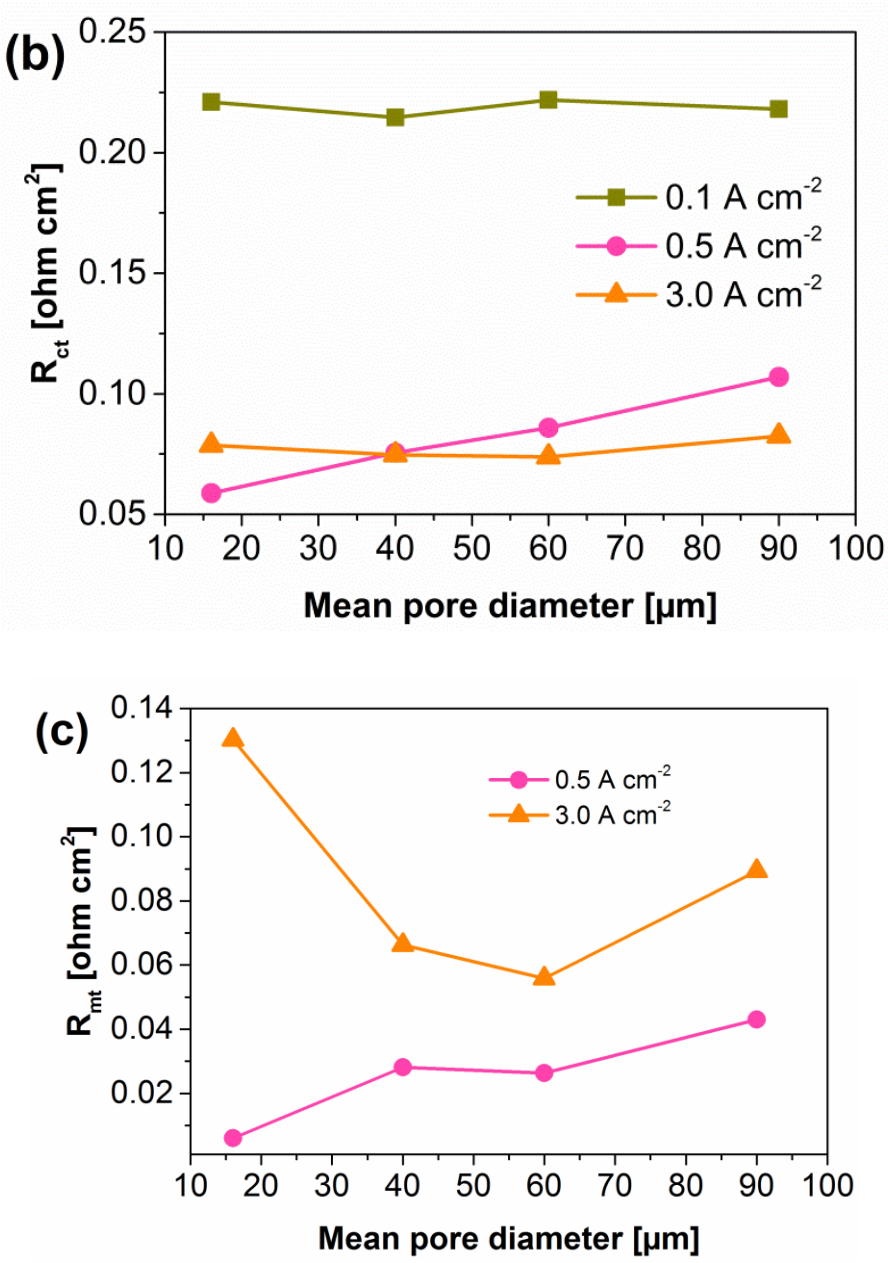

Figure 6.8. Comparison of EIS parameters using equivalent circuit models at current densities of 0.1, 0.5 and 3.0 A cm^{-2} (a) ohmic resistance, R_Ω (b) charge transfer resistance, R_{ct} and (c) mass transport resistance, R_{mt}.

6.3.6 Conclusions

The electrochemical analysis showed that there is a trade-off to consider for PTL design: smaller pore size results in better electron conductivity but poorer two-phase liquid-gas mass transport at high current density. Smaller pore PTLs result in lower interfacial contact resistance, as there are more contact points with the catalyst

layer. However, the better ohmic resistance is at the expense of mass transport capability at high current density.

The mass transport resistance trend in relation to pore size and current density implies that multiple factors are at play. Effective mass transport in a PTL involves water ingress and access to the catalyst as well as product gas (O_2) egress. At lower current density of 0.5 A cm^{-2} (Figure 6.7(b)), where mass transport effects start to become noticeable, the mass transport resistance follows a trend where smaller pores lead to better mass transport, as would be promoted by capillary-driven water transport. However, at higher current density of 3 A cm^{-2} (Figure 6.7(c)), the rate of gas generation is significantly higher and mass transport can be expected to be limited by how rapidly O_2 can be expelled from the system, the results imply that larger pores do this more effectively. The compound effect of these two factors leads to an optimum MPD of ~60 μm.

Overall, the apparent trade-off between minimised interfacial contact resistance (at small pore size) and maximised mass transport ability (at large pore size) must be carefully considered for optimized PTL design for the PEMWE, especially at high current density operations where mass transport becomes a limiting factor. Therefore, it is suggested that a graded pore size PTL would be most beneficial, in aggregating the advantage of the reduced interfacial resistance at smaller pore and improved mass transport at larger pores.

Chapter 7

Analysis of Mass Transport Phenomena in the PEMWE using a Full Factorial Design of Experiment Approach

7.1 Introduction

As discussed in Chapter 2, the effectiveness of mass transport in the PEMWE depends on several factors including the anode water feed rate, the flow field design, channel geometry, PTL design, etc. The influence of these various design and operational factors has been investigated individually in Chapters 4, 5, and 6. However, mass transport in the PEMWE is a complex, multicomponent and multiphase phenomenon, therefore a systemic understanding of the interaction of various factors, rather than their stand-alone effect, is desirable.

One way to approach this problem is to apply a design of experiments (DoE) methodology. DoE is a powerful statistical experimental design method for identification of the influence of the most important factors and the factor interactions in a system [156], [157]. When several variables influence performance, it is crucial to design a valid and reliable experiment from which sound conclusions can be drawn effectively and efficiently. Conventionally, experiments give the output or response value for a given fixed set of input factors influencing the system. By varying one particular input factor while keeping the rest of the input factors constant, an idea of the effect of that particular input factor on the response can be inferred. However, in reality, a combination of simultaneous variation in

input factors may result in different responses due to interactions among input factors [191]. However, this information cannot be obtained in conventional experimentation.

Therefore, one of the main advantages of the DoE methodology is that it explores the influence of several factors on overall system performance and the inter-connections between the factors and levels. Three main DoE methodology are widely used in various industries and academic fields, depending on the requirements of the situation: full-factorial, fractional factorial, and Taguchi orthogonal arrays [192]. The full-factorial design iterates all possible combinations within the experimental space and may thus require a prohibitive number of experimental runs; however, it offers precise results on the interaction between factors and avoids information loss and misleading conclusions. The fractional factorial method and the Taguchi orthogonal array exclude some of the factor-levels from the full-factorial design to achieve an optimized combination with minimum time and computational cost [193].

Despite the DoE's advantages as a statistical method capable of increasing experimental efficiency, and facilitating scientific objectivity in experimental data analysis, the DoE has seen only limited application in electrolyser and fuel cell research, although it is becoming increasingly employed in fuel cell optimization studies [193]–[197]. Dante *et al.* used a two level four factor fractional design experiment to optimize the power output of a commercial PEFC stack [198]. Flick *et al.* used DOE to evaluate the effect of six operating parameters on the micro porous layer of a PEM fuel cell [199]. Kahveci *et al.* used the response surface methodology (a special type of the DOE) to investigate water and heat management in PEM fuel cells [200]. Barari *et al.* applied DOE for temperature measurement accuracy in solid oxide fuel cells (SOFC) [201]. Wahdame *et al.* recommended the use of DOE in various areas of fuel cell research[202]. Lohoff *et al.* applied the DOE methodology to a DMFC stack for operational optimization [203]. A recent study by Toghyani *et al.* [204] used a thermodynamic modelling approach combined with the Taguchi method to optimize various operating parameters in the PEMWE. They showed that the relative contribution of various parameters to the overall cell overvoltage can be

determined. Similarly, to optimize PEMWE operation especially at high current density, it is necessary to understand the relative contributions and interactions between various design and operational mass transport parameters.

Hence, this chapter focuses on an exploratory work to investigate the effect of mass transport variables on the PMWE performance using a full-factorial design. Three key variables were considered at two levels representing the two extreme applied values of the factor, in order to determine their relative significance and/or their interactive effects on performance.

7.2 Experimental

7.2.1 Collection of Experimental Data

The experimental setup described in Section 3.2 was used. A constant current of 3.0 A cm^{-2} was applied for 45 mins and the corresponding cell voltage was measured. Two different flow-field designs (parallel and serpentine) were used, two anode PTLs (MPD 16 and 60 μm) and two water feed rates (15 and 60) were used in this study.

7.2.2 Experimental Design Methodology

The first step in the DoE is to identify the factors and the levels under investigation, which requires a fundamental understanding of the physics of the process. Based on present understanding, the three factors considered for the experimental design were the anode flow-field design, the anode porous transport layer, and the water feed rate. The levels of water feed rate was chosen based on ranges used in previous studies [91], [160]. Two of the most common, yet disparate, flow-field designs (parallel and serpentine designs) [91], [160], [205] are selected to show the effect of flow-field configuration; and the range of anode PTL was selected based on various mean pore diameter that has been explored in literature and previously in this study [57]. Hence the PTL levels for this analysis were selected in the range of 16 μm, labelled small-pore PTL (SP-PTL) to 60 μm labelled large-pore PTL (LP-PTL).

The full-factorial design which tests all possible conditions was used for this study for a test matrix of three factors and two-levels; which implies performing 2^3 or 8 experiments. This design takes into account all main effects and interaction effects of the factors. The experimental design and analysis of the factorial experiments were performed using MINITAB 17 (PA, USA) statistical software. Each experiment was replicated twice and a total of 16 experiments were performed. The running order was randomized to minimize the effects of undesirable disturbances or external factors which were uncontrollable during the experiment.

A summary of the variables and the levels for the experiment are presented in Table 7.1. Each factor was studied at both low and high levels. The regression model with three factors and their interactions is approximated by Eq. 7.1:

$$Y_i = b_0 + b_1X_1 + b_2X_2 + b_3X_3 + b_{12}X_1X_2 + b_{13}X_1X_3 + b_{23}X_2X_3 + b_{123}X_1X_2X_3 \quad (7.1)$$

where Y_i represents the experimental response, X_i is the coded variable (at low and high levels), b_i represents the estimation of the principal effect of the factor i for the response Y_i, whereas b_{ij} represents the estimation of interaction effect between factor i and j for the response. The coefficient b_0 represents the average value of the response of the eight combinations; b_{123} represents the interactions between three factors.

Table 7.1. Design factors and their levels.

Mass transport factors	Symbol	Level 1	Level 2
Anode flow field design	A	Serpentine	Parallel
Anode porous transport layer	B	SP-PTL	LP-PTL
Water feed rate	C	15 ml min^{-1}	60 ml min^{-1}

7.3 Results and Data Analysis

7.3.1 Electrochemical Performance

The measured experimental responses for the mass transport analysis are recorded and presented in Table 7.2. The value of the cell potential at various combinations and the replicate is presented. The analysis was performed on a "smaller the better" type since, in a PEMWE, the cell potential for a given operational current density must be minimized.

Table 7.2. Experimental design layout and results.

Std order	**Run Order**	**Flow–field design**	**Anode PTL**	**Water feed rate**	**Cell Potential @ 3.0 A cm^{-2} (1)**	**Cell Potential @ 3.0 A cm^{-2} (2)**
1	1	Serpentine	SP-PTL	15 ml min^{-1}	2.409	2.426
4	2	Parallel	LP-PTL	15 ml min^{-1}	2.489	2.489
2	3	Parallel	SP-PTL	15 ml min^{-1}	2.359	2.341
7	4	Serpentine	LP-PTL	60 ml min^{-1}	2.300	2.290
6	5	Parallel	SP-PTL	60 ml min^{-1}	2.241	2.244
3	6	Serpentine	LP-PTL	15 ml min^{-1}	2.494	2.494
8	7	Parallel	LP-PTL	60 ml min^{-1}	2.343	2.341
5	8	Serpentine	SP-PTL	60 ml min^{-1}	2.306	2.315

Figure 7.1 presents the performance of the various factor combinations in the PEMWE cell at constant operating temperature of 80°C and ambient pressure, labelled according to the run order. It is evident that different mass transport parameter combinations influence cell performance differently. For instance, at 3.0 A cm^{-2}, the cell voltage in the best performing combination (Run 5) was about 250 mV lesser than the worst performing combination (Run 6). This suggests that optimization of mass transport parameters in the PEMWE requires identifying the best combination of component designs and parameters.

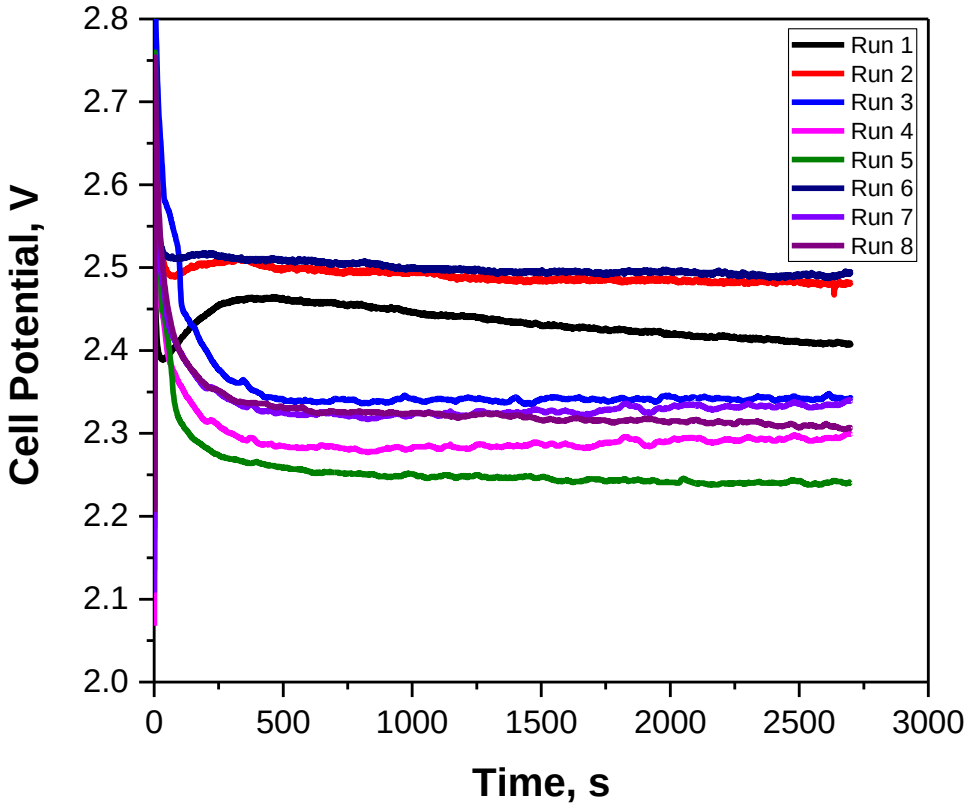

Figure 7.1. Cell potential as a function of time for various component and parameter combination at constant current density of 3 A cm^{-2} and operating temperature of 80°C and ambient pressure.

7.3.2 Analysis of variance (ANOVA) of experimental data

The full factorial design was applied to establish the relationship between the cell performance (cell potential at 3.0 A cm^{-2}) and the factors (anode flow-field design, anode PTL and water feed rate). The main procedure for determining the main and interaction effects of factors on the PEMWE performance is the analysis of variance (ANOVA). A confidence interval of 95% was selected within the Minitab software for the statistical analysis.

The degrees of freedom (Df), adjusted sum of squares (Adj SS), adjusted mean of squares (Adj MS), F-values and P-values are presented in Table 7.3. The F-value is defined as the ratio of the respective mean square effect and the mean square error. The P-value tests the null hypothesis that the coefficient obtained for the variable is

equal to zero (i.e. no effect). Thus a low P-value (in this study, P-value ≤0.05) indicates that the null hypothesis can be rejected and that the factor in question has a correlation with the response. The F-value, used in conjunction with the P-value therefore indicates how strongly a given factor influences the studied response [206]. A larger F-value means that the factor has greater significance for the cell performance; and an effect is considered statistically significant if P≤0.05 [207]. The effects plots, presented in later sections, illustrate the statistical analysis and provide the variation of significant effects. The ANOVA results show that at the 95% confidence level, all three factors, 2-way and 3-way interactions of the anode flow-field design, anode PTL and water feed rate significantly influence the PEMWE performance.

Table 7.3. Analysis of variance (ANOVA) for factors and their interactions.

Source	**Df**[a]	**Adj SS**	**Adj MS**	**F-Value**	**P-Value**
Model	7	0.112700	0.016100	315.69	0.000
A	1	0.002601	0.002601	51.00	0.000
B	1	0.021170	0.021170	415.10	0.000
C	1	0.076176	0.076176	1493.65	0.000
AB	1	0.007140	0.007140	140.00	0.000
AC	1	0.000900	0.000900	17.65	0.003
BC	1	0.003782	0.003782	74.16	0.000
ABC	1	0.000930	0.000930	18.24	0.000
Model	S	R-Sq.	R-Sq.(adj)	R-Sq.(Pred)	
Summary	0.0071414	99.64%	99.32%	98.56%	

The model P-values of 0.000 (100% confidence level) and 0.003 (99.7%) indicate that all the individual factors and their two-way and three-way interactions are significant. The R-Sq. value implies that the sample variation of 99.6% could be attributed to the parameters indicating that the model fits the data very well.

7.3.3 Normal Effects Plot

Figure 7.2 shows the normal plot of the standardized effects. The straight line in the plot indicates the points where the factors exhibit no effects. Thus, interception of points with the line indicates that the factors are insignificant, and the effects are close to zero whereas points lying away from the line signify factors with significant effects. Using α =0.05, the significant effects have been labelled. As can be seen, all the studied factors and their two-way and three-way interactions are significant.

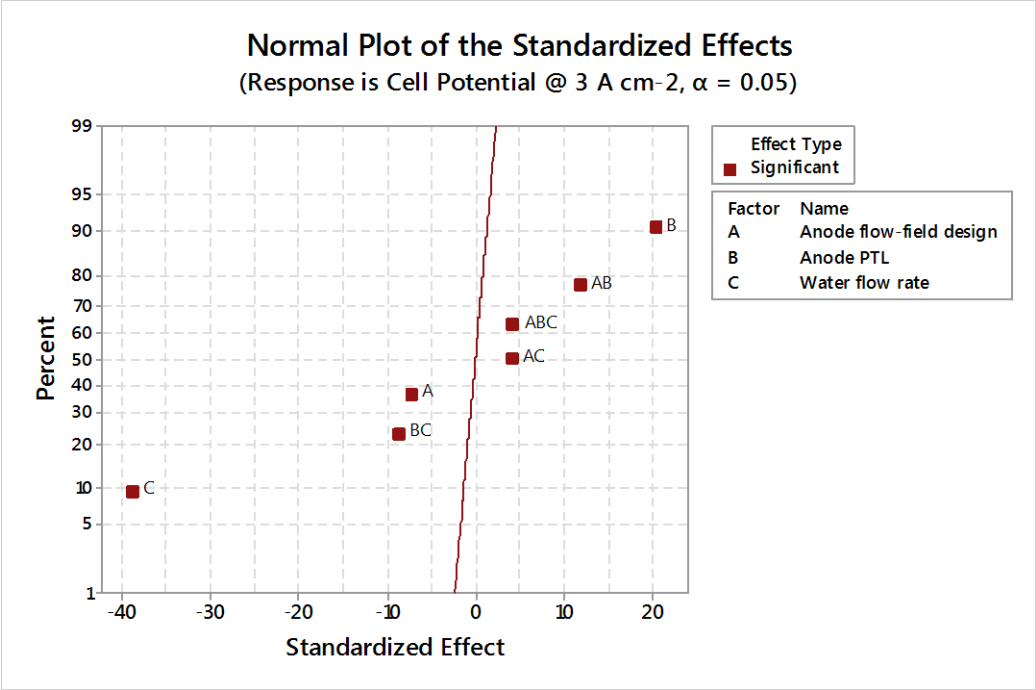

Figure 7.2. Normal plot of standardized effects of mass transport parameters.

7.3.4 Pareto Chart

The importance of each design factors and interactions can be graphically interpreted by constructing Pareto chart, presented in Figure 7.3. Pareto chart is a bar graph arranged in descending order from top to bottom. The bars not only represent the frequency but denote significance of the investigated factors and related interactions as well. In this way, the chart visually depicts which factors or interactions are most significant. Figure 7.3 shows that factor C (water feed rate) was the most significant factor on the performance, followed by B (anode PTL), and then AB (interaction between anode flow-field design and anode PTL) and so on. It can be seen from the graph that all the three factors and their interactions are

significant, as the standardized effects were greater than the margin error of 2.31 (red line).

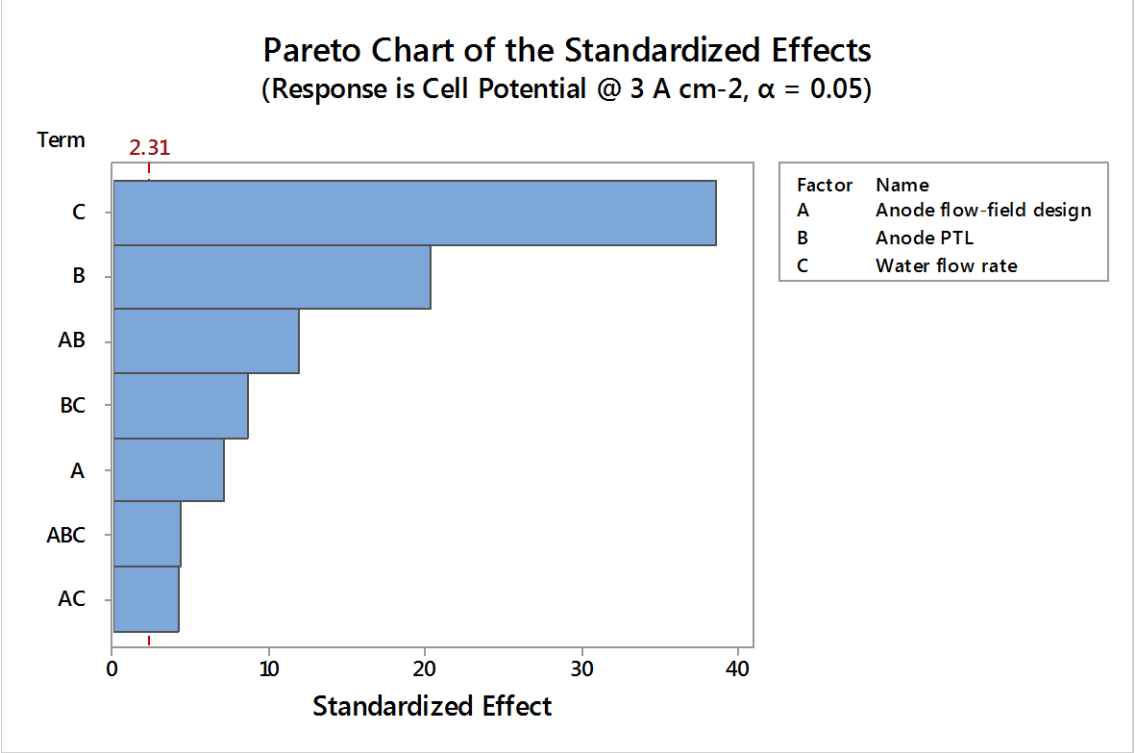

Figure 7.3. Pareto chart showing relative significance of the investigated factors and interactions.

7.3.5 Main Effects Plot

Figure 7.4 presents the main effect plot which shows the cell performance response to changing levels of each of the design factor. A bigger main effect is depicted by a line with steeper slope compared to the effects contributed by a less significant factor. The horizontal reference line at the middle of the plot shows the grand mean (the calculated average of all the data). To calculate the main effects, Minitab procedure subtracts the mean response at the low or first level of the factor from the mean response at the high or second level of the factor. It can be seen from Figure 7.4 that changing the level of water feed rate has the single highest influence on the cell performance. At its high setting of 60 ml min^{-1}, the cell performance improved by ~140 mV compared to its low setting of 15 ml min^{-1}, showing the most significant shift in performance when the factor levels are altered. This is followed by the effect of the anode PTL, which showed an improvement of about ~80 mV

when a SP-PTL (16 µm mean pore diameter) was used compared to LP-PTL (60 µm MPD). The least individual effect on the performance was observed in the anode flow-field design which showed an improvement of ~30 mV in the parallel design compared to the serpentine design.

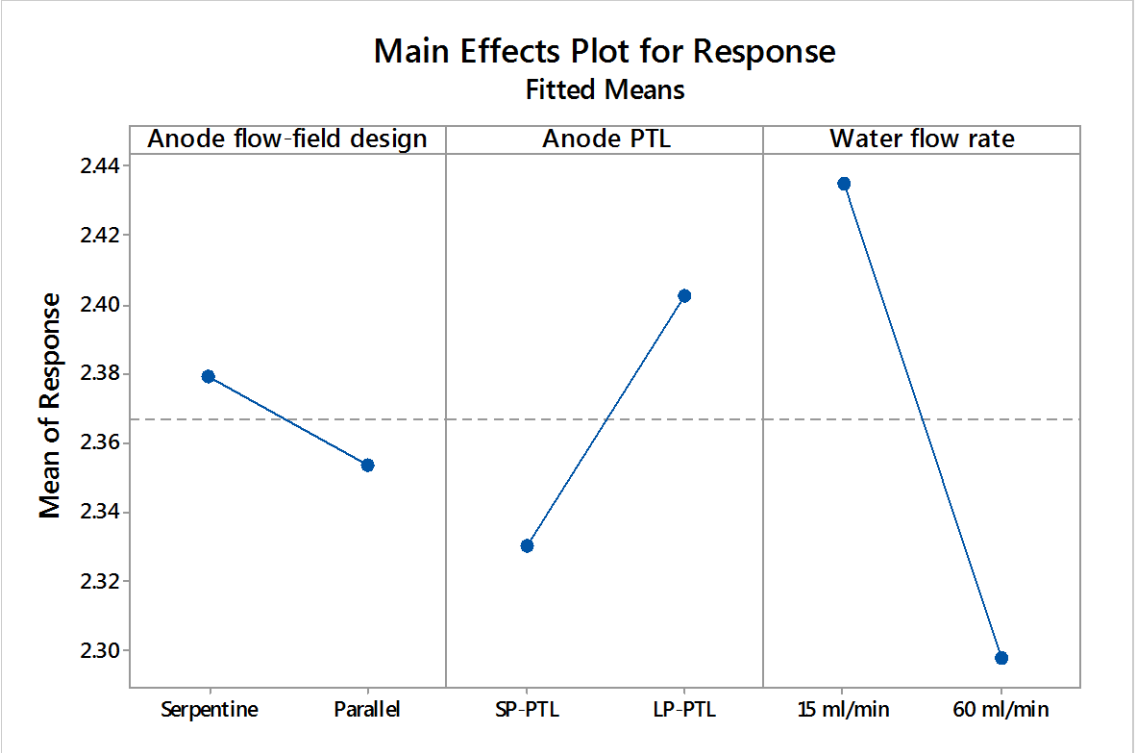

Figure 7.4. Effects of factor A (anode flow-field design, B (anode PTL), and C (water feed rate) on the cell performance at 80°C and ambient pressure.

These results are in accordance with the earlier studies presented in Chapters 4 and 6 which indicates that higher water feed rates ensures good reactant availability to the anode electrode and greater heat is supplied through the enthalpy of the higher flow water stream. Also, from the two-phase flow perspective, the slug length is shortened at higher flow which reduces residence time; therefore enhancing mass transfer leading to improved cell performance. Also, as presented in Chapter 4, the parallel flow-field design was found to perform better than the serpentine design, attributed to the longer flow path length in the serpentine design resulting in annular flow regime at high current density which degrades cell performance. Also,

as presented in Chapter 6, smaller pore PTLs showed better overall performance due to better interfacial contact resistance and therefore lower ohmic losses.

7.3.6 Interaction Effects Plot

Figure 7.5 shows the effect on the cell performance of varying one factor, keeping the second factor at its low and high level, and the third factor fixed (constant). These are called interaction plots, because they show how the response is impacted for any two factor combination. In these plots, non-parallel lines indicate that the effect of one factor on the response (cell performance) is dependent upon the setting of the other factor, the greater the lines depart from being parallel, the greater the strength of the interaction, whereas parallel lines indicate non-interaction [157].

As can be seen in Figure 7.5(a), the interaction of the anode flow-field and the anode PTL is evident, by the clearly non-parallel lines. The effect produced by the anode PTL is influenced by the type of flow-field used. The SP-PTL showed better cell performance when the parallel flow-field was used, and conversely, the LP-PTL showed slightly better cell performance when the serpentine flow-field was used. Overall, the cell performance is maximized (lowest cell voltage) when the smaller pore PTL and parallel flow-field are combined.

From Figure 7.5(b), it can be seen that there is an interaction between the anode flow-field and water feed rate, albeit weak, as the lines are almost parallel. This suggests that there is only a minor effect of water feed rate at different anode flow-field design. However, the interaction plot indicates that the cell performance is maximized when a parallel flow-field design is used combined with a high water feed rate.

Figure 7.5(c) illustrates the interaction plot between water feed rate and anode PTL. The non-parallel lines indicate a strong interaction. As can be seen from the plot, the effect of anode PTL on the cell performance is different at low and high level of water feed rate. The cell performance is maximized at high water feed rate in the small pore PTL. Conversely, the worst performance was observed at low water feed rate in the large pore PTL.

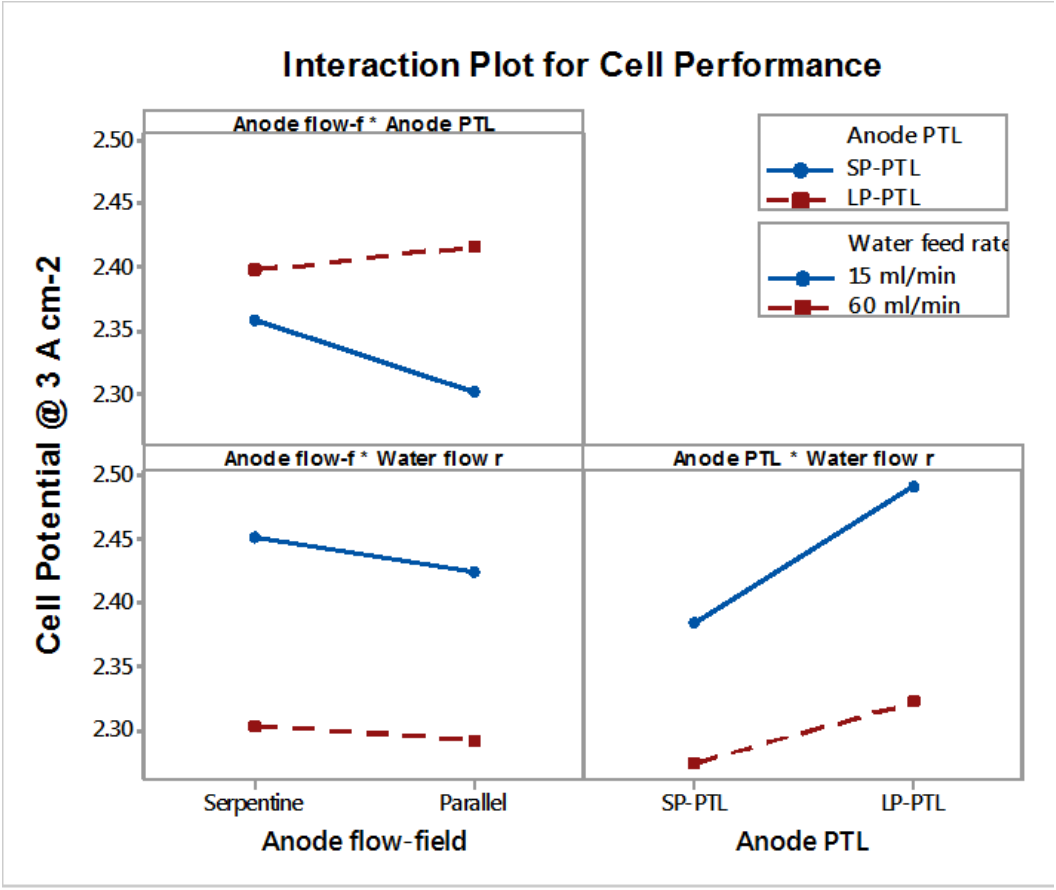

Figure 7.5. Interaction plots (anode flow-field design, anode PTL and water feed rate).

7.3.7 Regression Model

A regression model based on the statistically significant main effects and interactions is formed to predict the cell performance within the ranges of the factors selected. The estimated coefficients generated from the factorial analysis were used to obtain the predictive regression model of cell potential in coded variables as follows:

$$Cell\ Potential\ (V) = 2.36650 - 0.01275A + 0.03638B - 0.06900C + 0.02112AB + 0.00750AC - 0.01538BC + 0.00763ABC \quad (7.2)$$

Figure 7.6 provides an analysis of the residuals which display the precision of the model in fitting the PEMWE cell response. In the Normal Probability plot of

Figure 7.6(a) a minimal deviation from the red normalization line is seen, thus, the residuals are said to be normally distributed. The plot of residuals (b) versus Fitted values do show a random pattern of residuals on both sides of zero which suggests that the residuals have constant variance. Additionally, there is not much scattering around zero and no predominance of either the positive or negative residuals. This pattern indicates that the model is adequate as no distinct curve of points is observed. The histogram (c) suggests possible presence of outliers (larger than average response or predictor values), due to the gap between the bars. In the versus Order plots (d) there is no apparent pattern in the data points which implies that the variance is constant. Hence, it can be reasonably concluded that the model adequately describes the data and the ordinary least squares assumptions have been met.

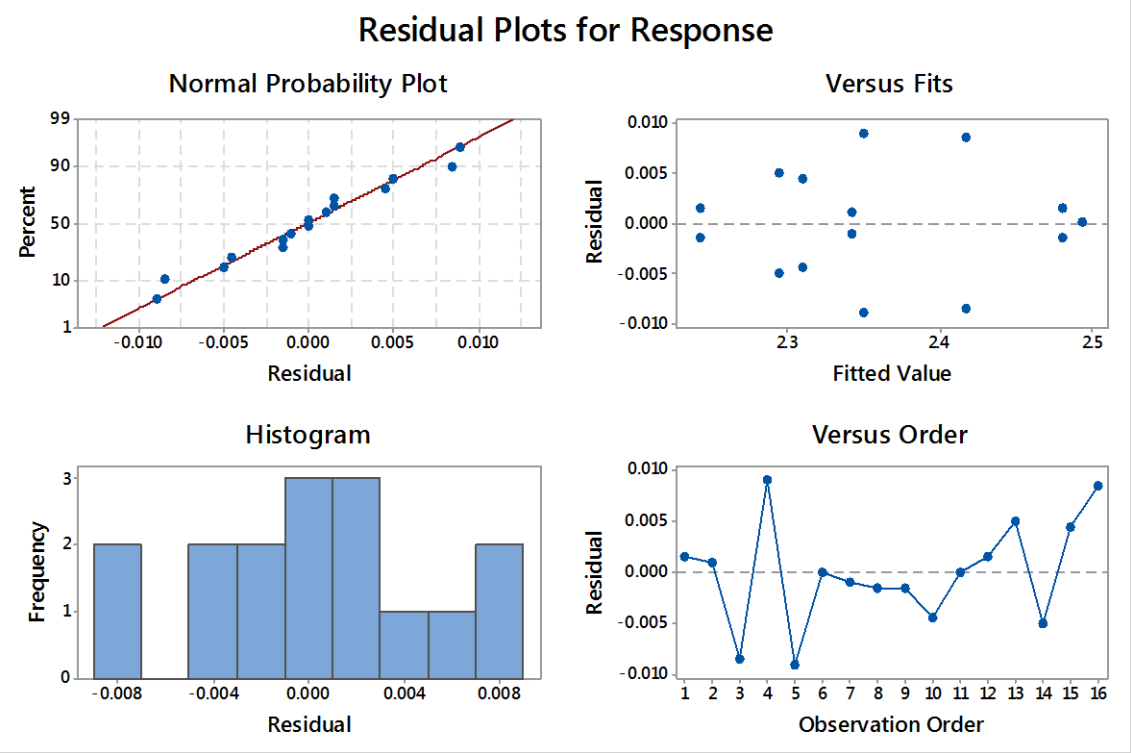

Figure 7.6. Residual plots for cell voltage (a) normal probability distribution, (b) histogram, (c) residuals versus fits and (d) residuals versus order.

7.4 Conclusions

In this chapter, a full-factorial design of experiment (DOE) was applied to PEMWE performance based on mass transport factors. The main effects and interaction of

operationally significant mass transport factors was investigated and a regression model based upon statistically significant factors was developed.

Single cell voltages at current density of 3.0 A cm^{-2} are examined as a response at two levels (high and low) of three factors (controlled variables); anode flow-field design, the anode porous transport layer, and the water feed rate. This yields a two-level, three factor (2^3) full factorial DOE.

The main effects and two factor interactions of each factor are examined to determine their effect on the cell voltage and the underlying physics behind various main effects and interaction influences is analysed. Of the design and parameter considered, the optimum was found to be a combination of high water feed rate of 60 ml min^{-1}, parallel flow-field design and small-pore PTL (16 μm mean pore diameter). It was demonstrated that design of experiments (DoE) can be used successfully as a method for PEMWE characterization with addition benefits and much less experimental effort than the one factor at a time (OFAT) method.

Chapter 8

Summary, Conclusions and Future Work

8.1 Summary and Conclusions

Understanding the multiphase and multicomponent mass transport phenomena in PEMWE is crucial, particularly towards design and performance improvements and large-scale commercialization. By applying various diagnostic techniques, *operando* and *ex-situ*, this research presents physical, electrochemical, qualitative and quantitative investigations on the two-phase flow in the flow channel and PTL of PEMWE cells and the effect of design and geometry and microstructure, in relation to performance.

8.1.1 Effect of Flow-field design by simultaneous high-speed visualization and electrochemical measurement

In the first phase of the research project presented in Chapter 4, the gas-bubble dynamics and two-phase flow behaviour in the anode flow channel of a PEMWE was investigated by simultaneous optical visualization electrochemical performance measurement for two disparate but commonly used flow-field designs, namely, the single serpentine flow-field (SSFF) and parallel flow-field (PFF). The effect of various operating parameters such as water circulation, water flow rate, and temperature on cell performance was also explored. The results show that the PFF design yielded a higher cell performance than the SSFF design at identical operating conditions. It was found that the flow regime of operation depends strongly on the flow path length and the length of gas slugs produced. Longer flow path length in the SSFF resulted in annular flow regime at a high current density

which degraded cell performance. This annular flow regime was absent in the PFF design. The channel-spanning long slugs characteristics of annular flow regime hinders water access to the PTL and electrocatalyst surface and hence the poorer performance in the SSFF. It was found the effect of flow rate on performance depends strongly on operating temperature in both flow patterns. The result indicated that long channel length promotes gas accumulation and channel-blocking which degrades performance in PEMWEs.

8.1.2 Effect of Anode Flow Channel Depth on PEMWE Cell Performance

The next phase of the research project presented in Chapter 5 focused on investigating the influence of anode flow channel geometry (depth) on the performance in a PEMWE; hitherto unexplored due to the difficulty of fabricating flow plates with various depth profiles. A single-straight flow channel was employed for simplification, and the channel depth was varied from 3 to 8 mm and the cell performance was studied at current densities up to 2.0 A cm^{-2} using electrochemical impedance spectroscopy (EIS).

The impedance results revealed that the cell performance was invariant with channel depth at low and medium current densities, which indicate that the activation-controlled nature at low current densities and the ohmic-controlled nature at medium current densities are unchanged by variation in the depth of the flow channel. However, a non-monotonic variation in cell performance was observed at high current densities, which is attributed to the opposing impact of flow velocity and mass transfer characteristics produced with varying channel depth. Therefore, the obtained results have demonstrated for the first time that modifying the anode channel depth might bring into play different factors which combine to determine cell performance.

8.1.3 Effect of Porous Transport Layer Microstructure on PEMWE cell performance

Further, this research work investigated the other key component of mass transport: the porous transport layer (PTL). The PTL has multiple roles of delivering water to

the electro-catalyst, removal of product gas, and acts as a conduit for electronic and thermal transport. They are, thus, a critical component for optimized performance, especially at high current density operation. The relationship between the PTL microstructure and corresponding electrochemical performance of commonly used titanium sinter PTLs was investigated.

Four PTLs, with mean pore diameter (MPD) ranging from 16 µm to 90 µm, were characterized *ex-situ* using scanning electron microscopy and X-ray computed micro-tomography to determine key structural properties. The microstructural properties of the PTLs, such as surface morphology, pore size distribution, porosity, tortuosity, and porosity distribution were investigated ex-situ by scanning electron microscopy (SEM) and X-ray computed micro-tomography. The electrochemical performance of the PTLs was investigated by steady-state polarization and electrochemical impedance spectroscopy at various operating conditions.

Results showed that an increase in mean pore size of the PTLs correlates to an increase in the spread and multimodality of the pore size distribution and a reduction in homogeneity of porosity distribution. Electrochemical measurements reveal a strong correlation of mean pore size of the PTLs with performance. Smaller pore size of PTLs resulted in better electron conductivity but poorer mass transport at high current density. Improved mass transport was enabled by a larger pore size, although a non-monotonic trend suggests an optimal pore size beyond which the advantageous influence of macroporosity for mass transport is diminished. The results indicate that maximizing contact points between the PTL and the catalyst layer is the overriding factor in determining the overall performance. Thus, the effectiveness of the PTL can be significantly improved if the interfacial contact resistance can be minimized. This study therefore suggests that graded pore size PTL would be most beneficial in aggregating the advantage of the reduced interfacial contact resistance at smaller pore and improved mass transport at larger pores.

8.1.4 Full-factorial DoE approach for Mass Transport Analysis

Optimized mass transport is crucial for high current density operations in PEMWEs. This study investigates the effect and interactions of anode mass

transport parameters on performance of a PEMWE using a 2^3 full factorial Design of Experiments (DoE) approach with two replications. The effects of anode flow-field design, anode porous transport layer and water feed rate on the cell performance were studied. At 95% confidence level, the result shows that all three factors and their 2-way interactions significantly affect the cell performance. Among them, the water feed rate shows the most significant contribution to performance, followed by the interaction between the flow field and PTL. A regression model was developed to relate the cell performance and the mass transfer parameters and the fitted model shows a good agreement between predicted and actual cell performance (R^2 = 0.99), demonstrating the validity of the regression analysis in the performance optimization. The best performance was obtained at parameter setting of parallel flow configuration, small average pore size of PTL and high water feed rate. The DoE is proved to be suitable method for investigating interactions and thus optimizing the operating conditions in order to maximize performance.

8.2 Suggestions for Future Work

This section is aimed to present a brief idea of the future work that may be expanded from the work reported here.

8.2.1 Correlation of Mass Transport with Current Density Distribution in the PEMWE

In addition to the difficulty with reactant supply or product removal, one very important side-effect of poor mass transport in the flow channels and PTL of the PEMWE is that the two-phase flow effect can lead to pronounced inhomogeneous current distribution as well as power loss of the PEMWE. An uneven current distribution may cause high local current densities associated with a high local degradation rate. For this reason, uneven current distribution does not only hinder performance, but also the durability of the PEMWE cell. Complementarily to the result presented in Chapter 4, an investigation of the local distribution of current as a function of the bubble dynamics and gas evolution at different operation modes would greatly enhance understanding and lead to improvements of cell operations, components and designs. In addition, by attaining media and current distribution

that is as homogeneous as possible, detrimental operating conditions can be identified and avoided during PEMWE operations.

In order to investigate the effects leading to inhomogeneous current distributions, a measurement technique that allows *in-situ* observation of the current, gas and water distribution simultaneously is required. Efforts are currently being made at the Electrochemical Innovation Lab in UCL to study these local heterogeneities *in situ*, build a correlation with the local mass transport phenomena and investigate effect on performance. The current density distribution is measured using an electronic Printed Circuit Board (PCB) from S++® Simulation Services Company.

8.2.2 Design of Experiment for Mass Transport Analysis

The DoE study presented in Chapter 7 was based on a two-level, three-factor (2^3) full factorial approach. The regression model obtained from a 2^3 DoE is linear due to only two levels of each factor being used. If the middle points indicate that the response showed a nonlinear behaviour, a three-level or higher DoE can be designed for obtaining a higher order regression model for better representation of the actual response. Also, a more comprehensive DoE study that includes factors such as cathode and anode flow-field design, PTL and operational factors such as temperature, pressure and even cell orientation would be beneficial in revealing relative significant of factors and factor interactions for optimization of PEMWE system performance.

8.2.3 Acoustics Techniques for Mass Transport Analysis

In addition to various diagnostic techniques that has been used to probe mass transport and gain insight into overall cell operation PEMWE, acoustic emission technique is a non-destructive, operando diagnostic tool that might prove useful in providing further insight to various processes during PEMWE operation. It is becoming increasingly used for diagnostics in various electrochemical processes such as for detection of corrosion in stainless steel, exfoliation of aluminium alloys, investigation of fractures in battery electrodes and seal cracking in solid oxide fuel cell.

The acoustic emission works by detecting transient elastic sound waves produced by sudden redistribution of stress in materials or processes. The perturbations are then converted into a voltage signal using a piezoelectric sensor. When the signal produced exceeds a certain predefined threshold, the acoustic 'hit' produced is captured in a voltage-time profile. By analysing parameters such as amplitude, frequency and number of hits per time, information about the process under consideration can be gathered.

Thus, acoustic emission technique could act as a valuable PEMWE diagnostic tool that could capture the local flow characteristics, including flow regimes and transitions during operation at various conditions.

8.2.4 *In-situ* and *Operando* Neutron and X-ray Imaging of PEMWE

The potential of X-ray imaging to aid characterization and enhance understanding of mass transport have been demonstrated in this study in Chapter 6, and the results obtained shows that the interaction and influence of various microstructural parameters can be determined to enable improved component design. However, microstructural characterization in this research was conducted on the PTLs *ex-situ,* away from cell operation. It is expected that *in-situ* and *operando* investigation in a bespoke cell would yield further valuable insight into the influence of the various microstructural properties on gas evolution, two-phase flow and overall performance in the PEMWE cell. Such an arrangement would enable real-time coupling of mass transport losses with various gas-bubble evolution and any structural change in components due to cell operation, thereby providing vital operational and degradation information, thus enabling design and performance improvements.

Research Dissemination

Talks and Conference Participations

- **Jude O. Majasan**, Ishanka Dedigama, Dan J.L Brett, Paul R. Shearing, "Gas Evolution and Two-Phase Flow Behaviour in the Anode Flow-field of PEM Water Electrolysers" **H2FC Supergen Research Conference 2017, University of St. Andrews, Scotland.**

- **Jude O. Majasan**, Jason I.S Cho, Maximilian Maier, Ishanka Dedigama, Dan J.L Brett, Paul R. Shearing, "Effect of Anode Flow Channel Depth on the Performance of Polymer Electrolyte Membrane Water Electrolyser" **233rd ECS Meeting 2018,Seattle,Washington, USA.**

- **Jude O. Majasan**, Jason I.S Cho, Maximilian Maier, Ishanka Dedigama, Dan J.L Brett, Paul R. Shearing, "Effect of Anode Flow Channel Depth on the Performance of Polymer Electrolyte Membrane Water Electrolyser" **World Hydrogen Energy Conference 2018, Rio de Janeiro, Brazil.**

- **Jude O. Majasan**, Jason I.S Cho, Maximilian Maier, Ishanka Dedigama, Dan J.L Brett, Paul R. Shearing, "Effect of Microstructure of Porous Transport Layer on Performance in Polymer Electrolyte Membrane Water Electrolyser". **3rd CDT Conference in Energy Storage and Applications, 2018 Univeristy of Sheffield, UK.**

- **Jude O. Majasan,** Jason I.S Cho, Maximilian Maier, Ishanka Dedigama, Dan J.L Brett, Paul R. Shearing, "Optimization of Mass Transport Parameters in Polymer Electrolyte Membrane Electrolysers: A Full Factorial Design of Experiment Approach". **20th International Conference on Hydrogen Energy and Technologies Rome, Italy.**

References

[1] S. Dunn, "Hydrogen futures: Toward a sustainable energy system," *Int. J. Hydrogen Energy*, vol. 27, no. 3, pp. 235–264, 2002.

[2] S. A. Grigoriev, V. I. Porembsky, and V. N. Fateev, "Pure hydrogen production by PEM electrolysis for hydrogen energy," in *International Journal of Hydrogen Energy*, 2006, vol. 31, no. 2, pp. 171–175.

[3] N. Briguglio *et al.*, "Renewable energy for hydrogen production and sustainable urban mobility," in *International Journal of Hydrogen Energy*, 2010, vol. 35, no. 18, pp. 9996–10003.

[4] F. Barbir, "PEM electrolysis for production of hydrogen from renewable energy sources," *Sol. Energy*, vol. 78, no. 5, pp. 661–669, 2005.

[5] E. (International R. E. A.-I. Aberg *et al.*, "Renewables 2018 Global Status Report," 2018.

[6] A. Louw *et al.*, "Global Trends in Renewable Energy Investment 2018," 2018.

[7] Bloomberg NEF, "Corporations Already Purchased Record Clean Energy Volumes in 2018, and It's Not an Anomaly," *Bloomberg NEF*, 2018. .

[8] I. INTERNATIONAL ENERGY AGENCY, "World Energy Outlook 2015," *World Energy Outlook 2015*, 2015.

[9] X. Luo, J. Wang, M. Dooner, and J. Clarke, "Overview of current development in electrical energy storage technologies and the application potential in power system operation," *Appl. Energy*, vol. 137, pp. 511–536, 2015.

[10] M. De Francesco and E. Arato, "Start-up analysis for automotive PEM fuel cell systems," *J. Power Sources*, vol. 108, no. 1–2, pp. 41–52, 2002.

[11] A. Rabbani and M. Rokni, "Start-up Analysis of a PEM Fuel Cell System in Vehicles," *Int. J. Green Energy*, 2013.

[12] G. Mulder, J. Hetland, and G. Lenaers, "Towards a sustainable hydrogen economy: Hydrogen pathways and infrastructure," *Int. J. Hydrogen Energy*, vol. 32, no. 10–11, pp. 1324–1331, 2007.

[13] K. Zeng and D. Zhang, "Recent progress in alkaline water electrolysis for hydrogen production and applications," *Progress in Energy and Combustion Science*, vol. 36, no. 3. pp. 307–326, 2010.

[14] H. E. Hoydonckx, W. M. Van Rhijn, W. Van Rhijn, D. E. De Vos, and P. A. Jacobs, *Ullmann's Encyclopedia of Industrial Chemistry*, vol. d. 2000.

[15] M. I. Gillespie, F. van der Merwe, and R. J. Kriek, "Performance evaluation of a membraneless divergent electrode-flow-through (DEFT) alkaline electrolyser based on optimisation of electrolytic flow and electrode gap," *J. Power Sources*, vol. 293, pp. 228–235, 2015.

[16] S. Trasatti, "Water electrolysis: Who first?," *J. Electroanal. Chem.*, 1999.

[17] W. Kreuter and H. Hofmann, "Electrolysis: the important energy transformer in a world of sustainable energy," *Int. J. Hydrogen Energy*, 1998.

[18] B. Dmitri, H. Wang, L. Hui, and N. Zhao, Eds., *PEM Electrolysis for Hydrogen Production: Principles and Applications*, 1st ed. CRC Press, 2016.

[19] D. Stolten and V. Scherer, *Transition to Renewable Energy Systems*. 2013.

[20] M. Götz *et al.*, "Renewable Power-to-Gas: A technological and economic review," *Renewable Energy*. 2016.

[21] M. A. Laguna-Bercero, "Recent advances in high temperature electrolysis using solid oxide fuel cells: A review," *Journal of Power Sources*. 2012.

[22] A. Brisse, J. Schefold, and M. Zahid, "High temperature water electrolysis in solid oxide cells," *Int. J. Hydrogen Energy*, 2008.

[23] M. A. Laguna-Bercero, S. J. Skinner, and J. A. Kilner, "Performance of solid oxide electrolysis cells based on scandia stabilised zirconia," *J. Power Sources*, 2009.

[24] T. Ishihara and T. Kannou, "Intermediate temperature steam electrolysis using LaGaO3-based electrolyte," in *Solid State Ionics*, 2011.

[25] A. Ursùa, L. M. Gandia, and P. Sanchis, "Hydrogen production from water electrolysis: Current status and future trends," in *Proceedings of the IEEE*, 2012, vol. 100, no. 2, pp. 410–426.

[26] A. Ursúa, L. M. Gandía, and P. Sanchis, "Hydrogen production from water electrolysis: Current status and future trends," in *Proceedings of the IEEE*, 2012.

[27] M. Carmo, D. L. Fritz, J. Mergel, and D. Stolten, "A comprehensive review on PEM water electrolysis," *International Journal of Hydrogen Energy*, vol. 38, no. 12. pp. 4901–4934, 2013.

[28] P. Medina and M. Santarelli, "Analysis of water transport in a high pressure PEM electrolyzer," *Int. J. Hydrogen Energy*, vol. 35, no. 11, pp. 5173–5186, 2010.

[29] K. E. Ayers *et al.*, "Research Advances towards Low Cost, High Efficiency PEM Electrolysis," *ECS Trans.*, 2010.

[30] S. A. Grigor'ev, M. M. Khaliullin, N. V. Kuleshov, and V. N. Fateev, "Electrolysis of water in a system with a solid polymer electrolyte at elevated pressure," *Russ. J. Electrochem.*, 2001.

[31] M. Carmo, D. L. Fritz, J. Mergel, and D. Stolten, "A comprehensive review on PEM water electrolysis," *Int. J. Hydrogen Energy*, vol. 38, no. 12, pp. 4901–4934, Apr. 2013.

[32] U. Babic, M. Suermann, F. N. Büchi, L. Gubler, and T. J. Schmidt, "Critical Review—Identifying Critical Gaps for Polymer Electrolyte Water Electrolysis Development," *J. Electrochem. Soc.*, vol. 164, no. 4, pp. F387–F399, 2017.

[33] C. Rozain and P. Millet, "Electrochemical characterization of Polymer Electrolyte Membrane Water Electrolysis Cells," *Electrochim. Acta*, 2014.

[34] L. Bertuccioli, A. Chan, D. Hart, F. Lehner, B. Madden, and E. Standen, "Study on development of water electrolysis in the EU, Fuel Cells and hydrogen Joint Undertaking," 2014.

[35] E. Brightman, J. Dodwell, N. Van Dijk, and G. Hinds, "In situ characterisation of PEM water electrolysers using a novel reference electrode," *Electrochem. commun.*, 2015.

[36] M. M. Mench, *Fuel Cell Engines*. 2008.

[37] O. F. Selamet, U. Pasaogullari, D. Spernjak, D. S. Hussey, D. L. Jacobson, and M. D. Mat, "Two-phase flow in a proton exchange membrane electrolyzer visualized in situ by simultaneous neutron radiography and optical imaging," *Int. J. Hydrogen Energy*, vol. 38, no. 14, pp. 5823–5835, 2013.

[38] A. Skulimowska *et al.*, "Proton exchange membrane water electrolysis with short-side-chain Aquivion® membrane and IrO2 anode catalyst," *Int. J. Hydrogen Energy*, 2014.

[39] V. Antonucci *et al.*, "High temperature operation of a composite membrane-based solid polymer electrolyte water electrolyser," *Electrochim. Acta*, 2008.

[40] C. LINKOUS, "Development of new proton exchange membrane electrolytes for water electrolysis at higher temperatures," *Int. J. Hydrogen Energy*, 1998.

[41] G. Wei, L. Xu, C. Huang, and Y. Wang, "SPE water electrolysis with SPEEK/PES blend membrane," *Int. J. Hydrogen Energy*, 2010.

[42] E. Antolini, "Carbon supports for low-temperature fuel cell catalysts," *Applied Catalysis B: Environmental*. 2009.

[43] S. A. Grigoriev, M. S. Mamat, K. A. Dzhus, G. S. Walker, and P. Millet, "Platinum and palladium nano-particles supported by graphitic nano-fibers as catalysts for PEM water electrolysis," *Int. J. Hydrogen Energy*, 2011.

[44] S. A. Grigoriev, P. Millet, and V. N. Fateev, "Evaluation of carbon-

supported Pt and Pd nanoparticles for the hydrogen evolution reaction in PEM water electrolysers," *J. Power Sources*, 2008.

[45] E. Rasten, G. Hagen, and R. Tunold, "Electrocatalysis in water electrolysis with solid polymer electrolyte," in *Electrochimica Acta*, 2003.

[46] S. Song, H. Zhang, X. Ma, Z. Shao, R. T. Baker, and B. Yi, "Electrochemical investigation of electrocatalysts for the oxygen evolution reaction in PEM water electrolyzers," *Int. J. Hydrogen Energy*, 2008.

[47] S. Siracusano, V. Baglio, N. Van Dijk, L. Merlo, and A. S. Aricò, "Enhanced performance and durability of low catalyst loading PEM water electrolyser based on a short-side chain perfluorosulfonic ionomer," *Appl. Energy*, vol. 192, pp. 477–489, 2017.

[48] S. Trasatti, "Electrocatalysis in the anodic evolution of oxygen and chlorine," *Electrochim. Acta*, 1984.

[49] R. Kötz and S. Stucki, "Stabilization of RuO2 by IrO2 for anodic oxygen evolution in acid media," *Electrochim. Acta*, 1986.

[50] J. Gatineau, K. Yanagita, and C. Dussarrat, "A new RuO4 solvent solution for pure ruthenium film depositions," *Microelectron. Eng.*, 2006.

[51] S. Siracusano *et al.*, "Optimization of components and assembling in a PEM electrolyzer stack," *Int. J. Hydrogen Energy*, vol. 36, no. 5, pp. 3333–3339, 2011.

[52] V. Baglio *et al.*, "Synthesis, characterization and evaluation of IrO2-RuO 2 electrocatalytic powders for oxygen evolution reaction," in *Journal of New Materials for Electrochemical Systems*, 2008.

[53] A. T. Marshall, S. Sunde, M. Tsypkin, and R. Tunold, "Performance of a PEM water electrolysis cell using Irx Ruy Taz O2 electrocatalysts for the oxygen evolution electrode," *Int. J. Hydrogen Energy*, 2007.

[54] D. Stolten and B. Emonts, *Hydrogen Science and Engineering: Materials, Processes, Systems and Technology*, 1st ed., vol. 1–2. 2016.

[55] J. Nie, Y. Chen, S. Cohen, B. D. Carter, and R. F. Boehm, "Numerical and experimental study of three-dimensional fluid flow in the bipolar plate of a PEM electrolysis cell," *International Journal of Thermal Sciences*, vol. 48, no. 10. pp. 1914–1922, 2009.

[56] H. Ito, T. Maeda, A. Nakano, A. Kato, and T. Yoshida, "Influence of pore structural properties of current collectors on the performance of proton exchange membrane electrolyzer," *Electrochim. Acta*, vol. 100, pp. 242–248, 2013.

[57] S. A. Grigoriev, P. Millet, S. A. Volobuev, and V. N. Fateev, "Optimization of porous current collectors for PEM water electrolysers," *Int. J. Hydrogen Energy*, vol. 34, no. 11, pp. 4968–4973, 2009.

[58] C. M. Hwang *et al.*, "Influence of properties of gas diffusion layers on the performance of polymer electrolyte-based unitized reversible fuel cells," *Int. J. Hydrogen Energy*, vol. 36, no. 2, pp. 1740–1753, 2011.

[59] H. Ito *et al.*, "Experimental study on porous current collectors of PEM electrolyzers," *Int. J. Hydrogen Energy*, vol. 37, no. 9, pp. 7418–7428, May 2012.

[60] F. Arbabi, A. Kalantarian, R. Abouatallah, R. Wang, J. S. Wallace, and A. Bazylak, "Feasibility study of using microfluidic platforms for visualizing bubble flows in electrolyzer gas diffusion layers," *J. Power Sources*, vol. 258, pp. 142–149, 2014.

[61] G. Yang *et al.*, "Additive manufactured bipolar plate for high-efficiency hydrogen production in proton exchange membrane electrolyzer cells," *Int. J. Hydrogen Energy*, vol. 42, no. 21, pp. 14734–14740, 2017.

[62] P. Lettenmeier, R. Wang, R. Abouatallah, F. Burggraf, A. S. Gago, and K. A. Friedrich, "Coated Stainless Steel Bipolar Plates for Proton Exchange Membrane Electrolyzers," *J. Electrochem. Soc.*, 2016.

[63] A. S. Gago, A. S. Ansar, P. Gazdzicki, N. Wagner, J. Arnold, and K. A. Friedrich, "Low Cost Bipolar Plates for Large Scale PEM Electrolyzers,"

ECS Trans., vol. 64, no. 3, pp. 1039–1048, Aug. 2014.

[64] A. S. Gago *et al.*, "Protective coatings on stainless steel bipolar plates for proton exchange membrane (PEM) electrolysers," *J. Power Sources*, 2016.

[65] M. Langemann, D. L. Fritz, M. M??ller, and D. Stolten, "Validation and characterization of suitable materials for bipolar plates in PEM water electrolysis," in *International Journal of Hydrogen Energy*, 2015, vol. 40, no. 35, pp. 11385–11391.

[66] M. Langemann, D. L. Fritz, M. Müller, and D. Stolten, "Validation and characterization of suitable materials for bipolar plates in PEM water electrolysis," in *International Journal of Hydrogen Energy*, 2015.

[67] P. Lettenmeier *et al.*, "Low-cost and durable bipolar plates for proton exchange membrane electrolyzers," *Sci. Rep.*, 2017.

[68] C. Martinson, G. Van Schoor, K. Uren, and D. Bessarabov, "Equivalent electrical circuit modelling of a Proton Exchange Membrane electrolyser based on current interruption," in *Proceedings of the IEEE International Conference on Industrial Technology*, 2013.

[69] A. Awasthi, K. Scott, and S. Basu, "Dynamic modeling and simulation of a proton exchange membrane electrolyzer for hydrogen production," *Int. J. Hydrogen Energy*, vol. 36, no. 22, pp. 14779–14786, 2011.

[70] R. García-Valverde, N. Espinosa, and A. Urbina, "Simple PEM water electrolyser model and experimental validation," in *International Journal of Hydrogen Energy*, 2012.

[71] *Advances in Batteries for Medium and Large-Scale Energy Storage*. 2016.

[72] A. J. Bard, L. R. Faulkner, E. Swain, and C. Robey, *Fundamentals and Applications*. 1996.

[73] P. Choi, D. G. Bessarabov, and R. Datta, "A simple model for solid polymer electrolyte (SPE) water electrolysis," in *Solid State Ionics*, 2004.

[74] I. Dedigama, K. Ayers, P. R. Shearing, and D. J. L. Brett, "An

experimentally validated steady state polymer electrolyte membrane water electrolyser model," *Int. J. Electrochem. Sci.*, 2014.

[75] D. L. Fritz, J. Mergel, and D. Stolten, "PEM Electrolysis Simulation and Validation," *ECS Trans.*, vol. 58, no. 19, pp. 1–9, 2014.

[76] C.-W. Sun and S.-S. Hsiau, "Effect of Electrolyte Concentration Difference on Hydrogen Production during PEM Electrolysis," *J. Electrochem. Sci. Technol.*, 2019.

[77] F. Marangio, M. Santarelli, and M. Calì, "Theoretical model and experimental analysis of a high pressure PEM water electrolyser for hydrogen production," *Int. J. Hydrogen Energy*, vol. 34, no. 3, pp. 1143–1158, 2009.

[78] S. Shiva Kumar and V. Himabindu, "Hydrogen production by PEM water electrolysis – A review," *Mater. Sci. Energy Technol.*, 2019.

[79] L. Ma, S. Sui, and Y. Zhai, "Investigations on high performance proton exchange membrane water electrolyzer," *Int. J. Hydrogen Energy*, 2009.

[80] T. Norman and M. Hamdan, "Unitized Design for Home Refueling Appliance for Hydrogen Generation to 5,000 psi," 2013.

[81] S. A. Grigoriev, V. I. Porembskiy, S. V. Korobtsev, V. N. Fateev, F. Aupr?tre, and P. Millet, "High-pressure PEM water electrolysis and corresponding safety issues," *Int. J. Hydrogen Energy*, vol. 36, no. 3, pp. 2721–2728, Feb. 2011.

[82] S. A. Grigoriev, A. A. Kalinnikov, P. Millet, V. I. Porembsky, and V. N. Fateev, "Mathematical modeling of high-pressure PEM water electrolysis," in *Journal of Applied Electrochemistry*, 2010, vol. 40, no. 5, pp. 921–932.

[83] M. S. Thomassen, "Next Generation PEM Electrolyser for Sustainable Hydrogen Production," 2012.

[84] K. A. Lewinski, D. F. van der Vliet, and S. M. Luopa, "NSTF Advances for PEM Electrolysis – The Effect of Alloying on Activity of NSTF Electrolyzer Catalysts and Performance of NSTF Based PEM Electrolyzers," *ECS Trans.*,

2015.

[85] E. Price, "Durability and Degradation Issues in PEM Electrolysis Cells and its Components," *Johnson Matthey Technol. Rev.*, vol. 61, no. 1, pp. 47–51, Jan. 2017.

[86] B. Verdin, F. Fouda-Onana, S. Germe, G. Serre, P. A. Jacques, and P. Millet, "Operando current mapping on PEM water electrolysis cells. Influence of mechanical stress," *Int. J. Hydrogen Energy*, 2017.

[87] B. Han, S. M. Steen, J. Mo, and F. Y. Zhang, "Electrochemical performance modeling of a proton exchange membrane electrolyzer cell for hydrogen energy," *Int. J. Hydrogen Energy*, 2015.

[88] O. Panchenko *et al.*, "In-situ two-phase flow investigation of different porous transport layer for a polymer electrolyte membrane (PEM) electrolyzer with neutron spectroscopy," *J. Power Sources*, vol. 390, pp. 108–115, 2018.

[89] Y. Li *et al.*, "In-situ investigation of bubble dynamics and two-phase flow in proton exchange membrane electrolyzer cells," *Int. J. Hydrogen Energy*, 2018.

[90] S. Sun *et al.*, "Behaviors of a proton exchange membrane electrolyzer under water starvation," *RSC Adv.*, vol. 5, no. 19, pp. 14506–14513, 2015.

[91] H. Ito *et al.*, "Effect of flow regime of circulating water on a proton exchange membrane electrolyzer," *Int. J. Hydrogen Energy*, vol. 35, no. 18, pp. 9550–9560, 2010.

[92] M. Sakurai, Y. Sone, T. Nishida, H. Matsushima, and Y. Fukunaka, "Fundamental study of water electrolysis for life support system in space," *Electrochim. Acta*, 2013.

[93] S. D. Greenway, E. B. Fox, and A. A. Ekechukwu, "Proton exchange membrane (PEM) electrolyzer operation under anode liquid and cathode vapor feed configurations," *Int. J. Hydrogen Energy*, 2009.

[94] I. Dedigama *et al.*, "In situ diagnostic techniques for characterisation of polymer electrolyte membrane water electrolysers - Flow visualisation and

electrochemical impedance spectroscopy," *Int. J. Hydrogen Energy*, vol. 39, no. 9, pp. 4468–4482, 2014.

[95] I. U. Dedigama, "Diagnostics and Modeling of Polymer Electrolyte Membrane Water Electrolysers."

[96] W. G. C. Ryan O'hayre, Suk-Won Cha, "Fuel Cell Fundamentals, 3. Edition," *Wiley*. 2005.

[97] I. Dedigama *et al.*, "Current density mapping and optical flow visualisation of a polymer electrolyte membrane water electrolyser," *J. Power Sources*, vol. 265, pp. 97–103, 2014.

[98] J. Mo *et al.*, "In situ investigation on ultrafast oxygen evolution reactions of water splitting in proton exchange membrane electrolyzer cells," *J. Mater. Chem. A*, 2017.

[99] H. Matsushima, T. Iida, and Y. Fukunaka, "Gas bubble evolution on transparent electrode during water electrolysis in a magnetic field," *Electrochim. Acta*, 2013.

[100] C. A. C. Sequeira, D. M. F. Santos, B. Šljukić, and L. Amaral, "Physics of Electrolytic Gas Evolution," *Brazilian Journal of Physics*. 2013.

[101] A. Bejan and A. D. Kraus, *Heat Transfer Handbook*, no. 3. 2003.

[102] S. L. Chen, C. T. Lin, C. Pan, C. C. Chieng, and F. G. Tseng, "Growth and detachment of chemical reaction-generated micro-bubbles on micro-textured catalyst," *Microfluid. Nanofluidics*, 2009.

[103] R. Fitzpatrick, "Axisymmetric incompressible inviscid flow," in *Theoretical Fluid Mechanics*, IOP Publishing, 2017, pp. 7–26.

[104] G. Q. Lu and C. Y. Wang, "Electrochemical and flow characterization of a direct methanol fuel cell," *J. Power Sources*, vol. 134, no. 1, pp. 33–40, 2004.

[105] T. E. Springer, "Polymer Electrolyte Fuel Cell Model," *J. Electrochem. Soc.*, 1991.

[106] S. Sadeghi Lafmejani, A. C. Olesen, and S. K. Kaer, "Analysing Gas-Liquid Flow in PEM Electrolyser Micro-Channels," *ECS Trans.*, vol. 75, no. 14, pp. 1121–1127, Sep. 2016.

[107] O. F. Selamet, U. Pasaogullari, D. Spernjak, D. S. Hussey, D. L. Jacobson, and M. D. Mat, "Two-phase flow in a proton exchange membrane electrolyzer visualized in situ by simultaneous neutron radiography and optical imaging," *Int. J. Hydrogen Energy*, vol. 38, no. 14, pp. 5823–5835, 2013.

[108] M. A. Hoeh *et al.*, "In-Operando Neutron Radiography Studies of Polymer Electrolyte Membrane Water Electrolyzers," *ECS Trans.*, vol. 69, no. 17, pp. 1135–1140, 2015.

[109] M. A. Hoeh *et al.*, "In operando synchrotron X-ray radiography studies of polymer electrolyte membrane water electrolyzers," *Electrochem. commun.*, vol. 55, pp. 55–59, 2015.

[110] A. S. Tijani, D. Barr, and A. H. A. Rahim, "Computational Modelling of the Flow Field of An Electrolyzer System using CFD," *Energy Procedia*, vol. 79, pp. 195–203, Nov. 2015.

[111] F. Aubras *et al.*, "Two-dimensional model of low-pressure PEM electrolyser: Two-phase flow regime, electrochemical modelling and experimental validation," *Int. J. Hydrogen Energy*, vol. 42, no. 42, pp. 26203–26216, 2017.

[112] D. D. H. Ruiz, A. P. Sasmito, and T. Shamim, "Numerical Investigation of the High Temperature PEM Electrolyzer: Effect of Flow Channel Configurations," *ECS Trans.* , vol. 58, no. 2, pp. 99–112, 2013.

[113] S. M. Steen, J. Mo, Z. Kang, G. Yang, and F. Y. Zhang, "Investigation of titanium liquid/gas diffusion layers in proton exchange membrane electrolyzer cells," *Int. J. Green Energy*, vol. 14, no. 2, pp. 162–170, 2017.

[114] C. H. Lee, R. Banerjee, F. Arbabi, J. Hinebaugh, and A. Bazylak, "Porous Transport Layer Related Mass Transport Losses in Polymer Electrolyte Membrane Electrolysis: A Review," in *ASME 2016 14th International*

Conference on Nanochannels, Microchannels, and Minichannels, 2016, p. V001T07A003.

[115] S. Park, J. W. Lee, and B. N. Popov, "A review of gas diffusion layer in PEM fuel cells: Materials and designs," *Int. J. Hydrogen Energy*, 2012.

[116] C. Rakousky, U. Reimer, K. Wippermann, M. Carmo, W. Lueke, and D. Stolten, "An analysis of degradation phenomena in polymer electrolyte membrane water electrolysis," *J. Power Sources*, 2016.

[117] P. Millet, F. Andolfatto, and R. Durand, "Design and performance of a solid polymer electrolyte water electrolyzer," *Int. J. Hydrogen Energy*, vol. 21, no. 2, pp. 87–93, 1996.

[118] J. Mo *et al.*, "Investigation of titanium felt transport parameters for energy storage and hydrogen/oxygen production," in *13th International Energy Conversion Engineering Conference*, 2015.

[119] T. Smolinka, "Review Lecture-Session HP.3d PEM Water Electrolysis-Present Status of Research and Development Agenda Background of PEM water electrolysis activities at Fraunhofer ISE," 2010.

[120] Y. Tanaka, K. Kikuchi, Y. Saihara, and Z. Ogumi, "Bubble visualization and electrolyte dependency of dissolving hydrogen in electrolyzed water using Solid-Polymer-Electrolyte," in *Electrochimica Acta*, 2005, vol. 50, no. 25-26 SPEC. ISS., pp. 5229–5236.

[121] P. Lettenmeier *et al.*, "Comprehensive investigation of novel pore-graded gas diffusion layers for high-performance and cost-effective proton exchange membrane electrolyzers," *Energy Environ. Sci.*, 2017.

[122] I. H. Oh, N. Nomura, N. Masahashi, and S. Hanada, "Mechanical properties of porous titanium compacts prepared by powder sintering," *Scr. Mater.*, vol. 49, no. 12, pp. 1197–1202, 2003.

[123] M. Thieme *et al.*, "Titanium Powder Sintering for Preparation of a Porous FGM Destined as a Skeletal Replacement Implant," *Mater. Sci. Forum*, vol. 308–311, no. October 2015, pp. 374–382, 1999.

[124] P. Millet *et al.*, "PEM water electrolyzers: From electrocatalysis to stack development," *Int. J. Hydrogen Energy*, vol. 35, no. 10, pp. 5043–5052, 2010.

[125] B. Han, J. Mo, Z. Kang, and F. Y. Zhang, "Effects of membrane electrode assembly properties on two-phase transport and performance in proton exchange membrane electrolyzer cells," *Electrochim. Acta*, 2016.

[126] L. Zielke, A. Fallisch, N. Paust, R. Zengerle, and S. Thiele, "Tomography based screening of flow field / current collector combinations for PEM water electrolysis," *RSC Adv.*, vol. 4, no. 102, pp. 58888–58894, 2014.

[127] F. Arbabi, H. Montazeri, R. Abouatallah, R. Wang, and A. Bazylak, "Three-Dimensional Computational Fluid Dynamics Modelling of Oxygen Bubble Transport in Polymer Electrolyte Membrane Electrolyzer Porous Transport Layers," *J. Electrochem. Soc.*, vol. 163, no. 11, pp. F3062–F3069, 2016.

[128] J. Wu, X. Z. Yuan, H. Wang, M. Blanco, J. J. Martin, and J. Zhang, "Diagnostic tools in PEM fuel cell research: Part I Electrochemical techniques," *International Journal of Hydrogen Energy*, vol. 33, no. 6. pp. 1735–1746, 2008.

[129] X.-Z. Yuan, C. Song, H. Wang, and J. Zhang, "Electrochemical Impedance Spectroscopy in PEM Fuel Cells," in *Electrochemical Impedance Spectroscopy in PEM Fuel Cells*, 2010, pp. 95–138.

[130] P. Millet, N. Mbemba, S. A. Grigoriev, V. N. Fateev, A. Aukauloo, and C. Etiévant, "Electrochemical performances of PEM water electrolysis cells and perspectives," *Int. J. Hydrogen Energy*, vol. 36, no. 6, pp. 4134–4142, Mar. 2011.

[131] J. Mo *et al.*, "Thin liquid/gas diffusion layers for high-efficiency hydrogen production from water splitting," *Appl. Energy*, vol. 177, pp. 817–822, 2016.

[132] P. Millet, "PEM Water Electrolysis," in *Hydrogen Production*, Weinheim, Germany: Wiley-VCH Verlag GmbH & Co. KGaA, 2015, pp. 63–116.

[133] C. Rozain and P. Millet, "Electrochemical characterization of Polymer Electrolyte Membrane Water Electrolysis Cells," *Electrochim. Acta*, vol. 131,

pp. 160–167, Jun. 2014.

[134] F. Barbir, *PEM Fuel Cells*. 2005.

[135] C. Breitkopf and K. Swider-Lyons, "Electrochemical Science — Historical Review," in *Springer Handbook of Electrochemical Energy*, 2017.

[136] A. Huth, B. Schaar, and T. Oekermann, "A 'proton pump' concept for the investigation of proton transport and anode kinetics in proton exchange membrane fuel cells," *Electrochim. Acta*, 2009.

[137] L. Schoeman, P. Williams, A. du Plessis, and M. Manley, "X-ray micro-computed tomography (μCT) for non-destructive characterisation of food microstructure," *Trends in Food Science and Technology*. 2016.

[138] E. Maire and P. J. Withers, "Quantitative X-ray tomography," *Int. Mater. Rev.*, 2014.

[139] V. Cnudde and M. N. Boone, "High-resolution X-ray computed tomography in geosciences: A review of the current technology and applications," *Earth-Science Reviews*. 2013.

[140] R. Mizutani and Y. Suzuki, "X-ray microtomography in biology," *Micron*. 2012.

[141] X. Lu *et al.*, "Multi-length scale tomography for the determination and optimization of the effective microstructural properties in novel hierarchical solid oxide fuel cell anodes," *J. Power Sources*, 2017.

[142] O. O. Taiwo *et al.*, "Microstructural degradation of silicon electrodes during lithiation observed via operando X-ray tomographic imaging," *J. Power Sources*, 2017.

[143] F. C. De Beer, "Characteristics of the neutron/X-ray tomography system at the SANRAD facility in South Africa," in *Nuclear Instruments and Methods in Physics Research, Section A: Accelerators, Spectrometers, Detectors and Associated Equipment*, 2005.

[144] K. S. Lim and M. Barigou, "X-ray micro-computed tomography of cellular

food products," *Food Res. Int.*, 2004.

[145] O. O. Taiwo, "3D and 4D Characterisation of Lithium Ion Battery Electrode Microstructures using X-ray Tomography," University College London, 2016.

[146] E. N. Landis and D. T. Keane, "X-ray microtomography," *Materials Characterization*, vol. 61, no. 12. pp. 1305–1316, 2010.

[147] B. Münch and L. Holzer, "Contradicting geometrical concepts in pore size analysis attained with electron microscopy and mercury intrusion," *J. Am. Ceram. Soc.*, 2008.

[148] S. J. Cooper, A. Bertei, P. R. Shearing, J. A. Kilner, and N. P. Brandon, "TauFactor: An open-source application for calculating tortuosity factors from tomographic data," *SoftwareX*, vol. 5, pp. 203–210, 2016.

[149] C. W. Wong, T. S. Zhao, Q. Ye, and J. G. Liu, "Experimental investigations of the anode flow field of a micro direct methanol fuel cell," *J. Power Sources*, vol. 155, no. 2, pp. 291–296, 2006.

[150] W. Yuan, A. Wang, Z. Yan, Z. Tan, Y. Tang, and H. Xia, "Visualization of two-phase flow and temperature characteristics of an active liquid-feed direct methanol fuel cell with diverse flow fields," *Appl. Energy*, vol. 179, pp. 85–98, 2016.

[151] H. Vogt, "Bubble coverage of gas-evolving electrodes in a flowing electrolyte," *Electrochim. Acta*, 2000.

[152] P. Boissonneau and P. Byrne, "Experimental investigation of bubble-induced free convection in a small electrochemical cell," *J. Appl. Electrochem.*, 2000.

[153] J. Mo *et al.*, "In situ investigation on ultrafast oxygen evolution reactions of water splitting in proton exchange membrane electrolyzer cells," *J. Mater. Chem. A*, vol. 5, no. 35, pp. 18469–18475, 2017.

[154] D. Zhang and K. Zeng, "Evaluating the behavior of electrolytic gas bubbles and their effect on the cell voltage in alkaline water electrolysis," *Ind. Eng.*

Chem. Res., 2012.

[155] L. Abdelouahed, G. Valentin, S. Poncin, and F. Lapicque, "Current density distribution and gas volume fraction in the gap of lantern blade electrodes," *Chem. Eng. Res. Des.*, 2014.

[156] D. C. Montgomery, "Design and Analysis of Experiments, 5th Edition," *America*. 2012.

[157] J. Antoy, *Design of Experiments for Engineers and Scientists: Second Edition*. 2014.

[158] R. Roy, "Design of Experiments Using the Taguchi Approach.pdf," *Technometrics*. 2001.

[159] C. Puncreobutr, P. D. Lee, R. W. Hamilton, and A. B. Phillion, "Quantitative 3D characterization of solidification structure and defect evolution in Al alloys," *JOM*, 2012.

[160] J. O. Majasan, J. I. S. Cho, I. Dedigama, D. Tsaoulidis, P. Shearing, and D. J. L. Brett, "Two-phase flow behaviour and performance of polymer electrolyte membrane electrolysers: Electrochemical and optical characterisation," *International Journal of Hydrogen Energy*, vol. 43, no. 33, pp. 15659–15672, 2018.

[161] J. Wang, "Theory and practice of flow field designs for fuel cell scaling-up: A critical review," *Appl. Energy*, vol. 157, pp. 640–663, 2015.

[162] T. Oi and Y. Sakaki, "Optimum hydrogen generation capacity and current density of the PEM-type water electrolyzer operated only during the off-peak period of electricity demand," *J. Power Sources*, vol. 129, no. 2, pp. 229–237, 2004.

[163] V. B. Oliveira, C. M. Rangel, and A. M. F. R. Pinto, "Effect of anode and cathode flow field design on the performance of a direct methanol fuel cell," *Chem. Eng. J.*, vol. 157, no. 1, pp. 174–180, 2010.

[164] A. S. Arico, P. Creti, V. Baglio, E. Modica, and V. Antonucci, "Influence of flow field design on the performance of a direct methanol fuel cell," *J. Power*

Sources, vol. 91, no. 2, pp. 202–209, 2000.

[165] D. Butterworth and G. F. Hewitt, *Two-phase flow and heat transfer*. 1977.

[166] Ö. F. Selamet, F. Becerikli, M. D. Mat, and Y. Kaplan, "Development and testing of a highly efficient proton exchange membrane (PEM) electrolyzer stack," *Int. J. Hydrogen Energy*, vol. 36, no. 17, pp. 11480–11487, 2011.

[167] W. Xu, K. Scott, and S. Basu, "Performance of a high temperature polymer electrolyte membrane water electrolyser," *J. Power Sources*, vol. 196, no. 21, pp. 8918–8924, 2011.

[168] J. O. Majasan *et al.*, "Correlative study of microstructure and performance for porous transport layers in polymer electrolyte membrane water electrolysers by X-ray computed tomography and electrochemical characterization," *Int. J. Hydrogen Energy*, vol. 44, no. 36, pp. 19519–19532, Jul. 2019.

[169] M. Suermann, K. Takanohashi, A. Lamibrac, T. J. Schmidt, and F. N. Büchi, "Influence of Operating Conditions and Material Properties on the Mass Transport Losses of Polymer Electrolyte Water Electrolysis," *J. Electrochem. Soc.*, vol. 164, no. 9, 2017.

[170] C. H. Lee *et al.*, "Influence of limiting throat and flow regime on oxygen bubble saturation of polymer electrolyte membrane electrolyzer porous transport layers," *Int. J. Hydrogen Energy*, vol. 42, no. 5, pp. 2724–2735, 2017.

[171] H. Ito *et al.*, "Influence of different gas diffusion layers on the water management of polymer electrolyte unitized reversible fuel cell," in *ECS Transactions*, 2010, vol. 33, no. 1 PART 1.

[172] C. M. Hwang *et al.*, "Effect of titanium powder loading in gas diffusion layer of a polymer electrolyte unitized reversible fuel cell," *J. Power Sources*, vol. 202, pp. 108–113, 2012.

[173] S. Siracusano *et al.*, "Electrochemical characterization of single cell and short stack PEM electrolyzers based on a nanosized IrO2anode electrocatalyst," *Int. J. Hydrogen Energy*, vol. 35, no. 11, pp. 5558–5568, 2010.

[174] E. Nishiyama and T. Murahashi, "Water transport characteristics in the gas diffusion media of proton exchange membrane fuel cell - Role of the microporous layer," *J. Power Sources*, vol. 196, no. 4, pp. 1847–1854, 2011.

[175] T. Kitahara, T. Konomi, and H. Nakajima, "Microporous layer coated gas diffusion layers for enhanced performance of polymer electrolyte fuel cells," *J. Power Sources*, vol. 195, no. 8, pp. 2202–2211, 2010.

[176] B. N. Popov, S. Park, and J. Lee, *Effect of Gas Diffusion Layer Structure on the Performance of Polymer Electrolyte Membrane Fuel Cell*. 2017.

[177] J. Park, H. Oh, Y. Il Lee, K. Min, E. Lee, and J. Y. Jyoung, "Effect of the pore size variation in the substrate of the gas diffusion layer on water management and fuel cell performance," *Appl. Energy*, vol. 171, pp. 200–212, 2016.

[178] P. Lettenmeier, S. Kolb, F. Burggraf, A. S. Gago, and K. A. Friedrich, "Towards developing a backing layer for proton exchange membrane electrolyzers," *J. Power Sources*, vol. 311, pp. 153–158, 2016.

[179] J. Mo, R. R. Dehoff, W. H. Peter, T. J. Toops, J. B. Green, and F.-Y. Zhang, "Additive manufacturing of liquid/gas diffusion layers for low-cost and high-efficiency hydrogen production," *Int. J. Hydrogen Energy*, vol. 41, no. 4, pp. 3128–3135, Jan. 2016.

[180] J. Mo, S. M. Steen III, S. Retterer, D. A. Cullen, A. Terekhov, and F.-Y. Zhang, "Mask-Patterned Wet Etching of Thin Titanium Liquid/Gas Diffusion Layers for a PEMEC," *ECS Trans.*, vol. 66, no. 24, pp. 3–10, 2015.

[181] Z. Kang *et al.*, "Investigation of thin/well-tunable liquid/gas diffusion layers exhibiting superior multifunctional performance in low-temperature electrolytic water splitting," *Energy Environ. Sci.*, vol. 10, no. 1, pp. 166–175, 2017.

[182] L. A. Feldkamp, L. C. Davis, and J. W. Kress, "Practical cone-beam algorithm," *J. Opt. Soc. Am. A*, 1984.

[183] M. Schalenbach, G. Tjarks, M. Carmo, W. Lueke, M. Mueller, and D.

Stolten, "Acidic or Alkaline? Towards a New Perspective on the Efficiency of Water Electrolysis," *J. Electrochem. Soc.*, 2016.

[184] J. Xu, Q. Li, E. Christensen, X. Wang, and N. J. Bjerrum, "Platinum activated IrO2/SnO2 nanocatalysts and their electrode structures for high performance proton exchange membrane water electrolysis," *Int. J. Electrochem. Sci.*, 2013.

[185] N. Epstein, "On tortuosity and the tortuosity factor in flow and diffusion through porous media," *Chem. Eng. Sci.*, 1989.

[186] B. Tjaden, S. J. Cooper, D. J. Brett, D. Kramer, and P. R. Shearing, "On the origin and application of the Bruggeman correlation for analysing transport phenomena in electrochemical systems," *Curr. Opin. Chem. Eng.*, 2016.

[187] K. Elsøe, L. Grahl-Madsen, G. G. Scherer, J. Hjelm, and M. B. Mogensen, "Electrochemical Characterization of a PEMEC Using Impedance Spectroscopy," *J. Electrochem. Soc.*, vol. 164, no. 13, pp. F1419–F1426, 2017.

[188] P. . S. and D. J. . B. J.O Majasan, J.I.S Cho, M. Maier, I. Dedigama, "Effect of Anode Flow Channel Depth on the Performance of Polymer Electrolyte Membrane Water Electrolyser," *ECS Trans.*, vol. 85, no. 13, pp. 1593–1603, 2018.

[189] J. Van Der Merwe, K. Uren, G. Van Schoor, and D. Bessarabov, "Characterisation tools development for PEM electrolysers," in *International Journal of Hydrogen Energy*, 2014, vol. 39, no. 26, pp. 14212–14221.

[190] I. Pivac and F. Barbir, "Inductive phenomena at low frequencies in impedance spectra of proton exchange membrane fuel cells – A review," *J. Power Sources*, vol. 326, pp. 112–119, Sep. 2016.

[191] R. R. Palkar and V. Shilapuram, "Development of a model for the prediction of hydrodynamics of a liquid-solid circulating fluidized beds: A full factorial design approach," *Powder Technol.*, 2015.

[192] S. Kaytakoğlu and L. Akyalçin, "Optimization of parametric performance of a PEMFC," *Int. J. Hydrogen Energy*, 2007.

[193] W. L. Yu, S. J. Wu, and S. W. Shiah, "Parametric analysis of the proton exchange membrane fuel cell performance using design of experiments," *Int. J. Hydrogen Energy*, 2008.

[194] P. Karthikeyan, M. Muthukumar, S. V. Shanmugam, P. P. Kumar, S. Murali, and A. P. S. Kumar, "Optimization of operating and design parameters on proton exchange membrane fuel cell by using Taguchi method," in *Procedia Engineering*, 2013.

[195] V. Lakshminarayanan and P. Karthikeyan, "Optimization of flow channel design and operating parameters on proton exchange membrane fuel cell using MATLAB," *Period. Polytech. Chem. Eng.*, 2016.

[196] A. Pessot *et al.*, "Contribution to the modelling of a low temperature PEM fuel cell in aeronautical conditions by design of experiments," *Math. Comput. Simul.*, 2019.

[197] Y. Rahim, H. Janßen, and W. Lehnert, "Characterizing membrane electrode assemblies for high temperature polymer electrolyte membrane fuel cells using design of experiments," *Int. J. Hydrogen Energy*, 2017.

[198] R. C. Dante *et al.*, "Fractional factorial design of experiments for PEM fuel cell performances improvement," *Int. J. Hydrogen Energy*, 2003.

[199] S. Flick, M. Schwager, E. McCarthy, and W. Mérida, "Designed experiments to characterize PEMFC material properties and performance," *Appl. Energy*, 2014.

[200] E. E. Kahveci and I. Taymaz, "Experimental investigation on water and heat management in a PEM fuel cell using response surface methodology," *Int. J. Hydrogen Energy*, 2014.

[201] F. Barari, R. Morgan, and P. Barnard, "A design of experiments (DOE) approach to optimise temperature measurement accuracy in Solid Oxide Fuel Cell (SOFC)," in *Journal of Physics: Conference Series*, 2014.

[202] B. Wahdame, D. Candusso, X. François, F. Harel, J. M. Kauffmann, and G. Coquery, "Design of experiment techniques for fuel cell characterisation and

development," *Int. J. Hydrogen Energy*, 2009.

[203] A. Schulze Lohoff, N. Kimiaie, and L. Blum, "The application of design of experiments and response surface methodology to the characterization of a direct methanol fuel cell stack," *Int. J. Hydrogen Energy*, 2016.

[204] S. Toghyani, S. Fakhradini, E. Afshari, E. Baniasadi, M. Y. Abdollahzadeh Jamalabadi, and M. Safdari Shadloo, "Optimization of operating parameters of a polymer exchange membrane electrolyzer," *Int. J. Hydrogen Energy*, 2019.

[205] S. Toghyani, E. Afshari, E. Baniasadi, and S. A. Atyabi, "Thermal and electrochemical analysis of different flow field patterns in a PEM electrolyzer," *Electrochim. Acta*, vol. 267, pp. 234–245, Mar. 2018.

[206] L. Oliveira, J. C. Santos, T. H. Panzera, R. T. S. Freire, L. M. G. Vieira, and F. Scarpa, "Evaluation of hybrid-short-coir-fibre-reinforced composites via full factorial design," *Compos. Struct.*, 2018.

[207] C. F. J. Wu and M. Hamada, *Experiments: Planning, analysis, and parameter design optimization*. 2000.